

**UNIVERSITÉ DU QUÉBEC**

**À CHICOUTIMI**

**MÉMOIRE PRÉSENTÉ À L'UNIVERSITÉ DU  
QUÉBEC À CHICOUTIMI COMME EXIGENCE  
PARTIELLE DE LA MAÎTRISE EN INGÉNIEURIE**

**Par**

**Mahmood Mousavi**

**Experimental and Theoretical Verification of Two Icing Codes**

**Vérification Expérimentale et Théorique de Deux Codes de Givrage**

**May 2003**



### Mise en garde/Advice

Afin de rendre accessible au plus grand nombre le résultat des travaux de recherche menés par ses étudiants gradués et dans l'esprit des règles qui régissent le dépôt et la diffusion des mémoires et thèses produits dans cette Institution, **l'Université du Québec à Chicoutimi (UQAC)** est fière de rendre accessible une version complète et gratuite de cette œuvre.

Motivated by a desire to make the results of its graduate students' research accessible to all, and in accordance with the rules governing the acceptance and diffusion of dissertations and theses in this Institution, the **Université du Québec à Chicoutimi (UQAC)** is proud to make a complete version of this work available at no cost to the reader.

L'auteur conserve néanmoins la propriété du droit d'auteur qui protège ce mémoire ou cette thèse. Ni le mémoire ou la thèse ni des extraits substantiels de ceux-ci ne peuvent être imprimés ou autrement reproduits sans son autorisation.

The author retains ownership of the copyright of this dissertation or thesis. Neither the dissertation or thesis, nor substantial extracts from it, may be printed or otherwise reproduced without the author's permission.

Le travail de recherche qui est présenté ici fait partie d'un programme de recherche basé sur le givrage des conducteurs aérien. Les investigations ont été effectuées dans le tunnel réfrigéré de la CIGELE. La première étape de ce travail a consisté en l'étude théorique de différents types de modèles de givrage existants. Parmi les modèles analytiques et numériques variés, deux modèles numériques généraux plus appropriés, pour l'accumulation de verglas sur les objets cylindriques, sont choisis et décrits en détails. La deuxième étape a consisté en la préparation de la série d'expériences de givrage. Lors de cette étape, la configuration de la teneur en eau liquide (LWC) et la taille médiane de gouttelette (MDS) pour des conditions spécifiques thermodynamique et aérodynamique ont été déterminées. Dans la troisième étape, les tests de givrage ont été effectués. Elles ont été effectués sur quatre cylindres d'aluminium de différents diamètres. Les expériences de givrage ont été effectuées dans les mêmes conditions thermodynamiques et aérodynamiques pour les LWC et MDS. À la quatrième étape, en utilisant des programmes écrits en Fortran, les deux modèles numériques ont été étudiés. Les résultats prédisent une accumulation de masse de verglas pour les mêmes LWC, MDS et diamètre de cylindre qui ont été déjà utilisés dans des expériences d'accrétion de verglas. Dans la cinquième étape, les résultats expérimentaux et théoriques sont comparés et validés. Les comparaisons permettent de révéler l'avantage des modèles choisis et leur précision de prévision de la masse de verglas accumulées sur les câbles aériens de transport d'énergie électrique. En conclusion, des recommandations nécessaires sont présentées aussi bien sur l'utilisation de ces modèles que sur les investigations futures dans ce domaine.

## **ABSTRACT**

The research paper submitted here is part of a larger over-all investigation into the problem of icing on electrical power cables, and which is being carried out at the CIGELE Icing Research Wind Tunnel based on the following steps. The first step involves the theoretical study of the range of existing types of icing models. From among the analytical and numerical models available, two numerical models were chosen and described in detail as being distinctly appropriate for explaining glaze-ice accumulation on cylindrical objects. The second step consists of setting up a series of icing experiments so as to initiate the research proper. At this stage, the distributions of liquid water content (LWC) and median droplet volume (MVD) for specific thermodynamical and aerodynamical conditions were figured out. Throughout the third step, the icing experiments were carried out using four aluminum cylinders of different diameters under the influence of the above-mentioned LWC and MVD distributions. During the fourth step, two FORTRAN programs were written and used to investigate the selected numerical models. The results provide the mass accumulation of glaze ice for the same LWC, MVD, and cylinder diameters as had already been used in the preceding icing experiments. The fifth step compares and analyzes the data collected from ice mass accumulation both experimentally and theoretically. The comparison serves to reveal the advantages and drawbacks of the selected models together with their prediction accuracy as regards the glaze-ice mass accreted on the electrical power cables. Lastly, certain necessary recommendations are put forward for the most productive manner of using these models, and for further functional investigation in this field.

## Acknowledgments

This work has been carried out within the framework of NSERC/Hydro-Quebec/UQAC industrial chair on Atmospheric Icing of Power Network Equipment (CIGELE).

I would like to express my gratitude to my director, **Prof. Massoud Farzaneh** for his instructions and support. I am very grateful to my co-director, **Dr. Anatolij Karev** for his gentle supervision and encouragement in the project.

I express my deep appreciation to all my professors in UQAC, and my special thanks to **Mr. Pierre Camarad**, **Mr. Sylvain Desgagné**, **Mr. Dominique Toulouse** for their help in performing the experiments, and **Madam Marijon Lesly Sinclair** for her valuable work in grammatical correction of the text of my master thesis.

Finally, I would like to thank all **members of CIGELE** for their support and help during different stages of project.

Mahmood Mousavi

## TABLE OF CONTENTS

<u>CHAPTER</u>	<u>PAGE</u>
<b>CHAPTER 1 INTRODUCTION</b>	
1.1 Background.....	1
1.2 Various approaches in investigating icing of power transmission lines.....	1
1.2.1 Continuous field measurement.....	2
1.2.2 Simulation in an icing tunnel.....	3
1.2.3 Construction of mathematical /computational icing model.....	4
1.3 Objective of this research work.....	5
1.4 Methodology.....	5
1.5 Structure of the thesis.....	6
 <b>CHAPTER 2. REVIEW OF LITERATURE</b>	
2.1 Introduction.....	8
2.2 Analytical and empirical models .....	8
2.1.1 The Imai Model.....	8
2.2.2 The Lenhard Model.....	9
2.2.3 The Goodwin Model.....	10
2.2.4 The Chaîné and Castonguay Model.....	12

2.2.5 The Jones simple Model .....	13
2.2.6 The icing clock model.....	15
2.3 Numerical Models .....	17
2.3.1 Porcu and Prodi 2-D stochastic18 Model.....	17
2.3.2 The Szilder and Lozowski, 3-D random walk model.....	19
2.3.3 The Lozowski, Stallabrass & Hearty model.....	23
2.3.4 The Makkonen model.....	23
2.4 Conclusion.....	24

### **CHAPTER 3. THE CIGELE ATMOSPHERIC ICING RESEARCH WIND TUNNEL AND RELATED EQUIPMENT**

3.1 Introduction .....	27
3.2 Construction of the Wind Tunnel and its Component and Systems.....	28
3.2.1 General Description of Air Circuit.....	28
3.2.2 Test Section.....	31
3.2.3 Functioning and Regulating of the CAIRWT Systems Maintaining Ambient Condition.....	33
3.3 Instrumentation.....	37
3.3.1 Air Speed.....	37
3.3.2 Air Temperature.....	39
3.3.3 Absolute and Relative air Humidity.....	40
3.3.4 LWC and DSD of the Aerosol Cloud.....	40
3.3.5 Data Acquisition System.....	42

## **CHAPTER 4. DESCRIPTION OF THE LOZOWSKI ET AL MODEL (1974) AND MAKKONEN (1984) MODEL**

4.1 Introduction.....	43
4.2 Lozowski et al (1979) Icing Code.....	43
4.2.1 General Structure.....	43
4.2.2. Input and Output Parameters of the Model.....	44
4.3 Collection Efficiency.....	46
4.3.1 General concept and theory of collection efficiency.....	46
4.3.2 Taylor (1940) on collection efficiency.....	47
4.3.3 Langmuir and Blodgett (1949) on collection efficiency.....	48
4.3.4 Lozowski et al. (1979) on collection efficiency.....	49
4.4 Steady State Heat Balance Equation.....	52
4.5 Application of the Model to Different Conditions.....	56
4.6 General structure the Makkonen (1984) model.....	58
4.6.1 Model Input and Output.....	58
4.6.2 Collection Efficiency of the Makkonen Model.....	59
4.6.3 Freezing Fraction .....	62
4.6.4 Heat Balance Equation.....	63
4.6.5 Time Dependence in the Makkonen Model .....	63
4.6.6 Ice Density.....	65

**CHAPTER 5 COMPARISON OF EXPERIMENTAL RESULTS WITH MODEL PREDICTIONS: VERIFICATION OF WATER RUN-BACK ICING MODEL**

5.1 Selecting a Basis for Comparison.....67

    5.1.1 Icing Intensity and Ice Load.....67

    5.1.2 Spatial Integration Procedure.....69

    5.1.3 Time Integration Procedure.....71

    5.1.4 Influence of Ice Sample Density and Sponginess.....72

5.2 Selecting Experimental Conditions.....76

    5.2.1 Air Speed.....76

    5.2.2 Air Temperature.....76

    5.2.3 Air Pressure and Air Humidity.....77

5.3 Liquid water content and droplet size distribution .....78

    5.3.1. Water Supply Rate: Liquid Water Content (LWC) or precipitation rate.....78

    5.3.2. Relationship between LWC and Air Velocity.....79

    5.3.3. Non-Uniformity of LWC and DSD in the Test Section and Lengthwise on the Experimental Cylinders.....83

5.4. Geometrical Parameters.....86

    5.4.1 Cylinder Diameter.....86

    5.4.2. Shape of Ice Accretion: Icicle Formation.....86

5.5. Final adjustment of the model.....87

5.6. Result and Discussions.....87

    5.6.1. Conditions of High and Ultra-High LWC.....88

    5.6.2. Effect of Excessive LWC.....89

5.5.3. Effect of Cylinder Diameter.....	90
5.6. Concluding Remark.....	95

**CHAPTER 6 COMPARISON OF THE EXPERIMENTAL RESULTS WITH  
MODEL PREDICTIONS: VERIFICATION OF THE MAKKONEN  
MODEL (1984)**

6.1 Selecting a Basis for Comparison .....	96
6.1.1 Specifics of Ice Load Calculations.....	96
6.1.2 Spatial Integration Procedure.....	98
6.1.3. Ice Sample Density, Ice Sponginess and Rotation of Experimental Cylinder.....	99
6.2. Experimental Conditions.....	100
6.2.1 Air Temperature and Air Speed.....	101
6.2.2. LWC and DSD.....	101
6.3. Geometrical Factors.....	101
6.4 Two modes of heat transfer.....	101
6.5. Results and Discussions.....	104
6.5.1. Effect of Excessive LWC.....	104
6.5.3. Effect of Cylinder Diameter.....	105
6.6. Conclusions.....	110

**CHAPTER 7 SUMMARY AND RECOMMENDATIONS**

7.1. Mutual Comparison of Rotating and Non-Rotating Icing Cylinders Series: Experimental and Theoretical Results.....	112
7.2. Process to be Developed and Incorporated in Appropriate Icing Code.....	115

7.3. Recommendations.....117

References.....123

APPENDICES: .....128

Appendix A: Relationship between various types of water supply.....129

Appendix B: Computer Program for Makkonen Model (1984).....133

Appendix C: Computer Program for Lozowski et al (1974) Model.....143

Appendix D:.....158

# LIST OF FIGURES

	<u>Pages</u>
<b>Fig.1.1</b> Empirical histogram for total ice accumulation on 315-KV line conductors(Savadjiev and Farzaneh, 2001).....	2
<b>Fig1.2.</b> Time histories of icing loads for a 10-millimeter cable at -5°C. (Chen and Ettema, 1993).....	3
<b>Fig. 2.1.</b> Comparison of the Jones Simple Model (1996) with the Chaîné and Castonguay Model (1974).....	15
<b>Fig. 2.2.</b> The icing clock model (Skelton and Poots,1988).....	16
<b>Fig. 2.3.</b> The domain of integration of icing nodes $\theta \in [0,2\pi)$ during one revolution.....	17
<b>Fig. 2.4.</b> Examples of different orientations and angular positions of a chain of impinging freezing by Porcu and Prodi, (1993).....	19
<b>Fig. 2.5.</b> Example of numerical experiment with a specific value of the median volume droplet diameter (MVD) in the DSD, Porcu and Prodi, (1993).....	19
<b>Fig. 2.6.</b> Influence of convective heat flux on the accretion process.....	22
<b>Fig. 2.7.</b> Influence of rainfall rate on the accretion process.....	22
<b>Fig.3.1.</b> Upper View of CIGELE Wind Tunnel.....	28
<b>Fig. 3.2.</b> Schematic diagram of CIGELE Atmospheric Icing Research Wind Tunnel.....	29
<b>Fig.3.2.</b> Test Section of CIGELE Atmospheric Icing Research Wind Tunnel.....	32
<b>Fig.3.4.</b> Spray-bar with the nozzles.....	35
<b>Fig.3.5.</b> Control panel for spray-bar.....	37
<b>Fig. 3.6</b> Boundary layer profiles in test section for two cases: <b>1.</b> without cylinder inside tunnel, <b>2.</b> with cylinder inside tunnel.....	39
<b>Fig. 3.5.</b> Data Acquisition System.....	41

<b>Fig.5.1.</b> Ice density as obtained in the experiments.....	74
<b>Fig. 5.2.</b> Experimental relationship between LWC , and air speed, $V_a$ .....	80
<b>Fig.5.3.</b> Two cumulative mass-based droplet size distributions (MSD) used for investigation of LWC/DSD uniformity.....	82
<b>Fig.5.4.</b> Comparison of experimentally recorded droplet size distribution.....	83
<b>Fig.5.5.</b> Experimentally obtained profiles of dimensionless relative LWC.....	84
<b>Fig. 5.6</b> Distribution of the LWC along the cylinder for the following ambient condition.....	85
<b>Fig. 5.7.</b> Comparison of the results of experimental and theoretical modelling A-type with air temperature $T_a = -5$ °C, and air speed $V_a = 5$ m s <sup>-1</sup> (Model of Lozowski).....	91
<b>Fig. 5.8.</b> Comparison of the results of experimental and theoretical modelling A-type with air temperature $T_a = -5$ °C, and air speed $V_a = 10$ m s <sup>-1</sup> (Model of Lozowski).....	91
<b>Fig. 5.9.</b> Comparison of the results of experimental and theoretical modelling A-type, with air temperature $T_a = -10$ °C, and air speed $V_a = 5$ m s <sup>-1</sup> (Model of Lozowski).....	92
<b>Fig. 5.10.</b> Comparison of the results of experimental and theoretical modelling A-type, with air temperature $T_a = -10$ °C, and air speed $V_a = 10$ m s <sup>-1</sup> (Model of Lozowski).....	92
<b>Fig. 5.11.</b> Comparison of the results of experimental and theoretical modelling, B-type, with air temperature $T_a = -5$ °C, and air speed $V_a = -5$ m s <sup>-1</sup> .....(Model of Lozowski).....	93
<b>Fig. 5.12.</b> Comparison of the results of experimental and theoretical modelling, B-type with air temperature $T_a = -5$ °C, and air speed $V_a = 10$ m s <sup>-1</sup> .....(Model of Lozowski).....	93
<b>Fig. 5.13.</b> Comparison of the results of experimental and theoretical modelling, B-type with air temperature $T_a = -10$ °C, and air speed $V_a = 5$ m s <sup>-1</sup> .....(Model of Lozowski).....	94
<b>Fig. 5.14.</b> Comparison of the results of experimental and theoretical modelling, B-type with air temperature $T_a = -10$ °C, and air speed $V_a = 10$ m s <sup>-1</sup> (Model of Lozowski).....	94

**Fig. 6.1.** Comparison of the experimentally obtained ice mass with the one theoretically predicted by using the Makkonen model (1984); Ambient conditions: A-type, with air temperature  $T_a = -5\text{ }^\circ\text{C}$ , and air speed  $V_a = 5\text{ m}\cdot\text{s}^{-1}$ .....106

**Fig. 6.2.** Comparison of the experimentally obtained ice mass with the one theoretically predicted by using the Makkonen model (1984); Ambient conditions: A-type, with air temperature  $T_a = -5\text{ }^\circ\text{C}$ , and air speed  $V_a = 10\text{ m}\cdot\text{s}^{-1}$ .....107

**Fig. 6.3.** Comparison of the experimentally obtained ice mass with the one theoretically predicted by using the Makkonen model (1984); Ambient conditions: A-type, with air temperature  $T_a = -5\text{ }^\circ\text{C}$ , and air speed  $V_a = 10\text{ m}\cdot\text{s}^{-1}$ .....108

**Fig. 6.4.** Comparison of the experimentally obtained ice mass with the one theoretically predicted by using the Makkonen model (1984); Ambient conditions: A-type, with air temperature  $T_a = -10\text{ }^\circ\text{C}$ , and air speed  $V_a = 5\text{ m}\cdot\text{s}^{-1}$ .....108

**Fig. 6.5.** Comparison of the experimentally obtained ice mass with the one theoretically predicted by using the Makkonen model (1984); Ambient conditions: B-type, with air temperature  $T_a = -5\text{ }^\circ\text{C}$ , and air speed  $V_a = 5\text{ m}\cdot\text{s}^{-1}$ .....108

**Fig. 6.6.** Comparison of the experimentally obtained ice mass with the one theoretically predicted by using the Makkonen model (1984); Ambient conditions: B-type, with air temperature  $T_a = -5\text{ }^\circ\text{C}$ , and air speed  $V_a = 10\text{ m}\cdot\text{s}^{-1}$ .....109

**Fig. 6.7.** Comparison of the experimentally obtained ice mass with the one theoretically predicted by using the Makkonen model (1984); Ambient conditions: B-type, with air temperature  $T_a = -10\text{ }^\circ\text{C}$ , and air speed  $V_a = 5\text{ m}\cdot\text{s}^{-1}$ .....109

**Fig. 6.8.** Comparison of the experimentally obtained ice mass with the one theoretically predicted by using the Makkonen model (1984); Ambient conditions: B-type, with air temperature  $T_a = -10\text{ }^\circ\text{C}$ , and air speed  $V_a = 10\text{ m}\cdot\text{s}^{-1}$ .....110

**Fig.7.1.** Comparison of rotating and non-rotating cylinder experiments in addition to the results the Makkonen model and the Lozowski at al. model (1979); ambient conditions: A-type, air temperature is  $T_a = -5^\circ\text{C}$  and air speed  $V_a = 5\text{ ms}^{-1}$ .....119

**Fig.7.2.** Comparison of rotating and non-rotating cylinder experiments in addition to the results the Makkonen model and the Lozowski at al. model (1979); ambient conditions: A-type, air temperature is  $T_a = -5^\circ\text{C}$  and air speed  $V_a = 10\text{ ms}^{-1}$ .....119

- Fig.7.3.** Comparison of rotating and non-rotating cylinder experiments in addition to the results the Makkonen model and the Lozowski at al. model (1979); ambient conditions: A-type, air temperature is  $T_a = -10^\circ\text{C}$  and air speed  $V_a = 5 \text{ ms}^{-1}$  ....120
- Fig.7.4.** Comparison of rotating and non-rotating cylinder experiments in addition to the results the Makkonen model and the Lozowski at al. model (1979); ambient conditions: A-type, air temperature is  $T_a = -10^\circ\text{C}$  and air speed  $V_a = 10 \text{ ms}^{-1}$  ....120
- Fig.7.5.** Comparison of rotating and non-rotating cylinder experiments in addition to the results the Makkonen model and the Lozowski at al. model (1979); ambient conditions: B-type, air temperature is  $T_a = -5^\circ\text{C}$  and air speed  $V_a = 5 \text{ ms}^{-1}$  .....121
- Fig.7.6.** Comparison of rotating and non-rotating cylinder experiments in addition to the results the Makkonen model and the Lozowski at al. model (1979); ambient conditions: B-type, air temperature is  $T_a = -5^\circ\text{C}$  and air speed  $V_a = 10 \text{ ms}^{-1}$  .....121
- Fig.7.7.** Comparison of rotating and non-rotating cylinder experiments in addition to the results the Makkonen model and the Lozowski at al. model (1979); ambient conditions: B-type, air temperature is  $T_a = -10^\circ\text{C}$  and air speed  $V_a = 5 \text{ ms}^{-1}$  .....122
- Fig.7.8.** Comparison of rotating and non-rotating cylinder experiments in addition to the results the Makkonen model and the Lozowski at al. model (1979); ambient conditions: A-type, air temperature is  $T_a = -10^\circ\text{C}$  and air speed  $V_a = 10 \text{ ms}^{-1}$  ....122

## **CHAPTER 1**

### **INTRODUCTION**

#### **1.1 Background: Icing of overhead transmission lines**

Atmospheric icing is a major concern of design engineers in northern countries such as Canada. Ice accretion due to freezing rain, drizzle, icing fog, and wet snow may cause costly damage to structures such as telecommunications towers, wind turbines or transmission lines, and significantly reduce their reliability. The ice weight coupled with wind loading effects, such as galloping, may result in the breakage of power lines, ground wires and insulators, and also collapse their supporting structures including towers and poles. Such serious storms are almost yearly events in Canada.

In the great ice storm of January 1998 in eastern Canada and the north-eastern United States, prolonged freezing rain brought down 120,000 km of power lines and telephone cables, 1,300 major transmission towers each worth about \$100,000, and about 27,000 wooden utility poles costing about \$3,000 each. Over 1,500,000 households in Canada were left without power for periods ranging from a few hours to several days or weeks. The damage in eastern Ontario and southern Quebec was so severe that major rebuilding of the electrical grid, and not merely repairing, had to be undertaken.

#### **1.2. Various Approaches in Investigating of Icing of power Transmission Lines**

In order to overcome the problems arising from excessive ice accretion, three main methods) of investigation have been employed in this field over the last several decades, and they will be briefly outlined below (Ref: 29).

### 1.2.1. Continuous Field Measurements

Gathering of natural ice and wind load data, together with the simultaneous measuring of meteorological elements in order to find the statistical relationships between them, is one of the ways of investigating the meteorological phenomenon called atmospheric icing. The existence of a rime/wet-snow load database with a corresponding historical weather database for each geographical region is of major importance for designers of structures. Also, such a database is essential for the validation of experimental and theoretical simulations of the icing process. The disadvantages of this approach involve: i) high costs for the installation of measurement sites for a geographical location; and ii) management requirements: an example of this approach may be found in a study carried out by Savadjiev and Farzaneh (2001). They analyzed 54 icing events that occurred on a 315-Kv line conductor at Mt. Belair, Quebec, Canada, between February 1998 and April 2000.

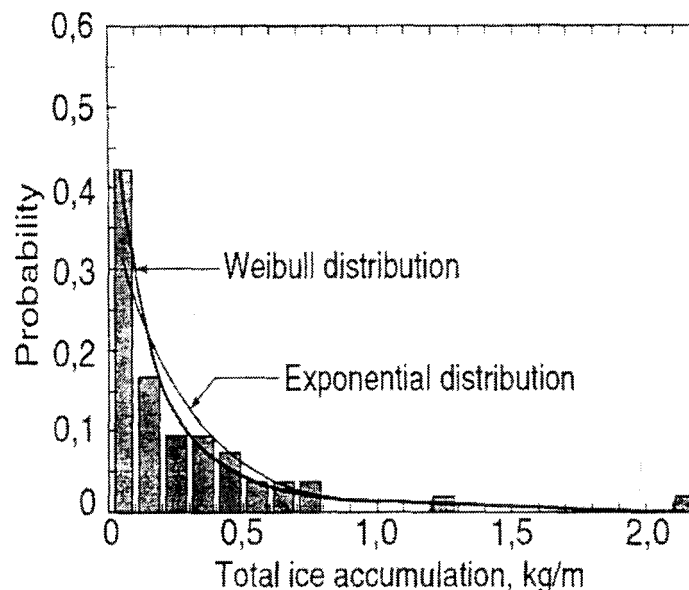


**Fig.1.1** Empirical histogram for total ice accumulation on 315-KV line conductors and best fitting curves: Weibull and exponential distributions(Savadjiev and Farzaneh, 2001).

Figure 1.1, taken from their study, shows the calculated probabilities of ice accumulation based on the Weibull and exponential distributions.

### 1.2.2 Simulation in an Icing Wind Tunnel

The advantage of this approach is that the effects of changes in flow and in thermal conditions on the accretion process can be readily assessed and analyzed. One disadvantage of the method, however, is that, due to the many physical and meteorological elements which must be taken into account, it is difficult to achieve an exact correspondence between the icing wind tunnel and field conditions. A good example of this approach is the study carried out by Chen and Ettema (1993) at the Iowa Institute of Hydraulic Research. Their laboratory experiments investigated the atmospheric-ice loading of power transmission cables. They conducted these

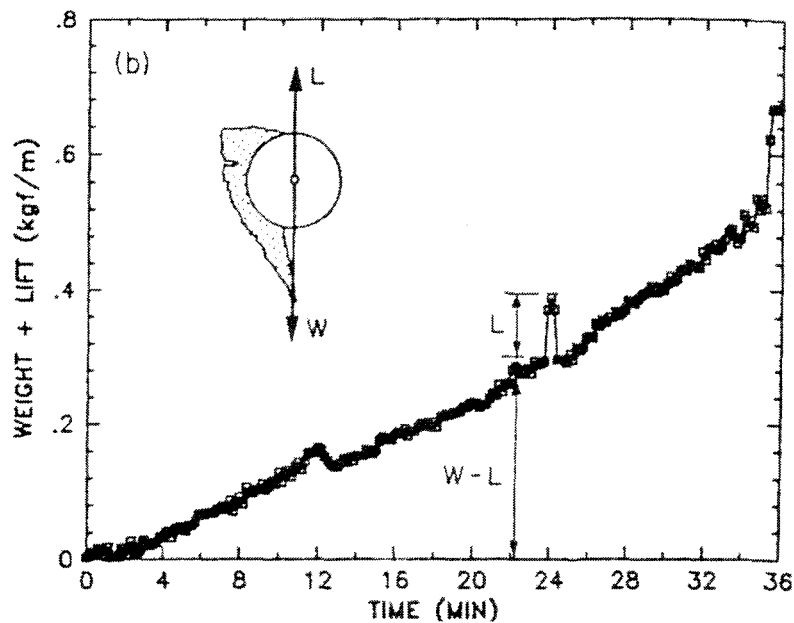


**Fig1.2.** Time histories of icing loads for a 10-millimeter cable at  $-5^{\circ}\text{C}$ .

experiments in an icing wind tunnel that was located alternately outdoors during frigid weather, and in a large refrigerated laboratory. Figure 1.2 shows part of their results

regarding the time dependence feature of ice accretion on electrical power transmission line cables.

### **1.2.3 Construction of Mathematical /Computational Icing Models**

This method involves using theoretical models, which are based on the known physics of the accretion process, and it has obvious advantages especially when implemented in the form of a computational code. The method possesses few disadvantages as opposed to its many advantages, yet one of the major disadvantages is that it requires the input of meteorological elements associated with a particular icing event, which, as mentioned earlier, can be laborious and costly to monitor *in situ*. Moreover, since the aggregate of meteorological elements always produces unique meteorological conditions, it is sometimes not clear which of these elements plays a crucial role during specific atmospheric icing processes. Even such a disadvantage, however, cannot detract from the growing usefulness of the method as it continues to increase in parallel with the development of computer potential and advances in computational accuracy. The first icing model involving mathematical calculation was produced in the 1950's. A number of atmospheric icing models have been developed since then, and may be distinguished from one another by such characteristics as the varying assessment of the role of certain factors involved in the process; the type of atmospheric icing phenomena modeled; methods for the solution of a physical problem; and, the extent to which the mathematical machine is applied. Two main types of investigative procedure may be distinguished in the rapidly developing domain of computational fluid dynamics using updated techniques for modelling the icing process.

The first is to model the icing process by consistently improving computational techniques without changing the main concept from the point of view of overall understanding. The second is to verify experimentally certain already developed icing models for their ability to predict atmospheric icing formation, particularly for some specific type of ice accretion. This second method has been selected for use in this investigation.

### **1.3. Objectives of This Research Project**

The principal objective of this project is i) to verify two well-known mathematical models for icing on horizontal rotating and non-rotating cylinders, and ii) to quantify, accurately and systematically, the range and conditions of their application for predicting the atmospheric icing phenomenon called glaze ice on overhead transmission lines (OHTL). This study forms the experimental part of the research project that is aimed at establishing a universal atmospheric icing model at CIGELE for the prediction of icing of bodies of different shapes. A further objective of this project is to develop an atmospheric icing model with an explicit presentation of a thin water film flowing on an icing surface, and a close-to-natural presentation of microphysical phenomena on an icing surface. The secondary objective of this study is to verify the existence of an eventual dependence of ice accretion load on the diameter of the cable used for OHTL's.

### **1.4. Methodology**

After an extensive review of the literature carried out in the preparation phase of the project and related to atmospheric icing models including a study of a variety of analytical and numerical approaches used in them, two classical models were selected incorporating runback water flow and freezing fraction calculation. The icing models

selected are the Makkonen model (1984) for icing of wire including its rotation, and the Lozowski et al. (1979) model for icing of a non-rotating horizontal cylinder. In order to perform the theoretical and experimental comparison of the atmospheric icing models selected initial adjustments of the Fortran codes of the models were made at the second stage of this study. The mutual comparison of the improved icing codes for three groups of distinctive ambient conditions favorable to glaze ice formation was carried out at this stage. These conditions are classified as follows: i) high liquid water content (LWC); ii) low supercooled air flow; and, iii) rapid air speed. At this stage of the investigation, an experimental verification of the chosen mathematical models was made in the wind tunnel for the same three sets of conditions. The third stage of the study consists of comparing the theoretical and experimental results; revealing the differences between them; establishing one of the adjusted models for calculation of icing of OHTL; and, submitting proposals for trends in further improvement of the established model in order to obtain the best fit between results of theoretical and laboratory modelling.

#### **4. Structure of the Thesis**

The second chapter presents several classic atmospheric icing models, both analytical and numerical, which investigate ice accretions on rotating and non-rotating horizontal cylinders, and provides basis for the selection of the models for verification under laboratory conditions. The third chapter provides details of the experimental facility at which two selected models were verified and its equipment. The physics of the process of icing and the mathematics of its presentation in the two selected atmospheric icing models are discussed in full detail from the point of view of thermodynamics and

aerodynamics in the fourth chapter. In chapter five, a comparison is made of the results obtained from the icing tests for non-rotating horizontal cylinders and the results obtained by application of the Lozowski et al. (1979) model to the same atmospheric icing conditions. A similar type of comparison is made in chapter six between the results from icing tests obtained for rotating horizontal cylinders and the results obtained from application of the Makkonen (1984) atmospheric icing model. The results obtained in the rotating and non-rotating series, both theoretical and experimental, are compared in chapter seven, in which some eventual improvements are proposed for the models presented in order to make it possible for them to be used as diagnostic and prognostic tools.

## Chapter 2

### REVIEW OF THE LITERATURE

#### 2.1 Introduction

Among the different approaches to the categorization of atmospheric icing models, the most common types are the ones that reflect the level of mathematical complexity required. In this chapter, several selected models (*i.e.* empirical, analytical and numerical), classified according to degree of complexity, are introduced first. Then, in the concluding section, the advantages or limitations of each model are discussed.

#### 2.2 Analytical and Empirical Models

##### 2.2.1 The Imai Model – based of the work of Makkonen (Ref: 22)

Imai's model (1953) is the earliest study on the atmospheric icing of structures, which incorporates mathematical calculation. Imai proposed that the growth rate of glaze ice on a cylindrical structure, modelling electrical cable per unit of its length,  $dM/dt$ , is proportional to the square root of air speed,  $V$ , and the radius of cylinder,  $R$ , and also proportional to the air temperature,  $T(^{\circ}C)$ :

$$\frac{dM}{dt} = C_1 \cdot \sqrt{V \cdot R} \cdot (-T) \quad (2.1)$$

where  $C_1$  is a constant. By integrating equation (2.1) one obtains

$$R^{3/2} = C_2 \cdot \sqrt{V} \cdot (-T) \cdot t \quad (2.2)$$

where the ice density is assumed to be constant and equal to  $0.9 \text{ g cm}^{-3}$ , and  $t$  is the time.

“The Imai model is based on the idea that icing intensity is controlled only by the heat transfer from the cylinder, *i.e.* the icing mode is assumed to be wet growth”[Ref: 22].

Thus,  $dM/dt$  during occurrence of icing phenomena is proportional to the value of air temperature taken with a negative sign. As a consequence, the precipitation intensity,  $I$ , has no effect on the final ice load. Although this idea is conceptually correct, more recent studies (Lozowski et al., 1979; Makkonen, 1984) have shown that  $C_2$  (the constant defining features of heat transfer) is also affected by surface roughness and evaporative cooling, and that the wet growth conditions do not always prevail down to  $-5^\circ\text{C}$ , as assumed by Imai. Because of these observations, “the model overestimates ice loads under typical icing conditions, and underestimates ice loads under extreme icing conditions because the value of  $C_2$  is too small, and the formation of icicles is not taken into consideration. The underestimation is particularly severe if the air temperature of the glaze event is close to  $0^\circ\text{C}$ ”[Ref: 22].

### 2.2.2 The Lenhard Model- based of the work of Makkonen (Ref: 22)

Based on empirical data, Lenhard (1955) proposed that the ice weight per meter,  $M$ , is

$$M = C_3 + C_4 \cdot H_g \quad (2.3)$$

“where  $H_g$  is the total amount of precipitation during the icing event, while  $C_3$  and  $C_4$  are constants. It follows from the above equation that” [Ref: 22]

$$\frac{dM}{dt} = C_4 \cdot I \quad (2.4)$$

This model may be counted as an alternative to the above-named Imai model due to the influence of the precipitation intensity,  $I$ , on the ice load only. The model, however, is fairly simplistic, due to the fact that it disregards effects of wind and air temperature.

### 2.2.3 The Goodwin Model - based on the work of Makkonen( Ref:22)

“The Goodwin et al. model (1983) assumes that all the drops collected freeze on the cable. In other words, the growth mode is dry. Then, the accretion rate per unit length of the cable modelled by a horizontal cylindrical icing structure is:

$$\frac{dM}{dt} = 2 \cdot R \cdot w \cdot V_i \quad (2.5)$$

Here,  $R$  is the radius of the ice-covered cylinder,  $w$  is the liquid water content (LWC) in air and  $V_i$  is the droplet impact speed. The mass per unit length,  $M$ , at time  $t$  equals  $\pi \cdot \rho \cdot (R^2 - R_0^2)$ , where  $R$  is the radius of the ice-covered cylinder at the end of time interval  $t$  and  $R_0$  is the radius of the bare cylinder. Substituting for  $M$  in the above equation gives”[Ref: 22]

$$\frac{dR}{dt} = \frac{w \cdot V_i}{\rho_i \cdot \pi} \quad (2.6)$$

The droplet impact speed is :

$$V_i = \sqrt{V_d^2 + V^2} \quad (2.7)$$

where  $V_d$  is the terminal falling velocity of the droplets and  $V$  is wind speed. Here, it is assumed that the wind is perpendicular to the cable orientation. The LWC,  $w$ , can be related to the depth of liquid precipitation,  $H_g$  measured during the accretion time  $t$  by:

$$\rho_w \cdot H_g = w \cdot V_d \cdot t \quad (2.8)$$

where  $\rho_w$  is the water density.

“By integrating equation (2.6) and inserting equation (2.7) into it gives:

$$\Delta R = \frac{w \cdot V_i \cdot t}{\rho_i \cdot \pi} \sqrt{1 + \left(\frac{V}{V_d}\right)^2} \quad (2.9)$$

which, by using equation (2.8), equals:

$$\Delta R = \frac{\rho_w \cdot H_g}{\rho_i \cdot \pi} \sqrt{1 + \left(\frac{V}{V_d}\right)^2} \quad (2.10)$$

Equation (2.10) is the correct analytical solution for radial ice thickness”[Ref: 22].

#### **2.2.4 The Chaîné and Castonguay Model - based of the work of Makkonen( Ref:25)**

Like the Goodwin et al. model (1983), this model assumes that all impinging droplets freeze on the cable. The main difference between the Chaîné and Castonguay model (1974) and the Goodwin et al. model (1983) involves the shape of the ice. Instead of a circular shape in cross-section, the Chaîné and Castonguay model (1974) assumes an elliptical ice shape. In such a case, the cross-sectional area of the ice, according to (2.3) in the Lenhard model (1955), becomes:

$$S_i = \frac{\pi \cdot R_0}{2} \sqrt{H_g^2 + H_v^2} \quad (2.11)$$

where  $H_v$  is the thickness of the water layer which is deposited on the vertical surface, as follows:

$$H_v = \frac{w \cdot V \cdot t}{\rho_w} \quad (2.12)$$

In the first step, Chaîné and Castonguay (1974) defined a correctional area, and calculations were based on equation (2.11). Then,  $S_i$  was compared with the radial ice section showing that the equivalent radial ice thickness was:

$$\Delta R = \left( \frac{R_0 \bullet K}{2} \sqrt{H_g^2 + H_v^2} + R_0^2 \right)^{1/2} - R_0 \quad (2.13)$$

where

$$K = 1.4 + 0.25 \frac{H}{R_0} \quad , \text{ and} \quad H = (H_g^2 + H_v^2)^{1/2} \quad (2.14)$$

The shape correction factor, K, is determined empirically from the work of Stallabrass and Hearty (1967), as a function of  $R_0$  and air temperature  $t_a$ . Makkonen (1996) has already shown that K is more complex than previously believed, and that it depends on all relevant parameters which affect the icing process as well as the ice density.

### 2.2.5 Jones' Simple Model

Jones (1996) describes her model as a simple model, which can be used in any back-of-an-envelope calculations of ice loads, based on the precipitation rate and wind speed. Assuming a circular shape for ice accreted on a horizontal cylinder, she made use of an empirical relationship (Best 1949) between LWC ( $w$ ) and the precipitation rate ( $P$ ), in which:

$$w = 0.067 \bullet P^{0.846} \quad (2.15)$$

where the LWC is expressed in  $\text{g m}^{-3}$  and the precipitation rate in  $\text{mm hour}^{-1}$ . The total water flux  $w_z$  may then be found by adding the horizontal flux of water  $w \bullet V$  ( $\text{g m}^{-2} \cdot \text{s}^{-1}$ ) during freezing rain storms to the vertical flux of rain  $P \cdot \rho_w / 10$  expressed in  $\text{g cm}^{-2} \cdot \text{hour}^{-1}$ :

$$w_{\Sigma} = \left[ (0.1 \cdot P \cdot \rho_w)^2 + (0.36 \cdot w \cdot V)^2 \right]^{1/2} \quad (2.16)$$

Thus, the uniform radial ice thickness on a circular cylinder is:

$$R_{eq} = \frac{N}{\rho_i \cdot \pi} \left[ (0.1 \cdot P \cdot \rho_w)^2 + (0.36 \cdot w \cdot V)^2 \right]^{1/2} \quad (2.17)$$

where  $N$  is the number of hours of freezing rain with a precipitation rate  $P$  ( $\text{mm} \cdot \text{hour}^{-1}$ ) and wind speed  $V$  ( $\text{m} \cdot \text{s}^{-1}$ ) during a storm. The precipitation rate and wind speed may vary over time, therefore, based on empirical observation, equation (2.17) may be written in a more general fashion as:

$$R_{eq} = \frac{1}{\rho_i \cdot \pi} \sum_{j=1}^N \left[ (0.1 \cdot P_j \cdot \rho_w)^2 + (0.36 \cdot w_j \cdot V_j)^2 \right]^{1/2} \quad (2.18)$$

where  $P_j$ ,  $W_j$  and  $V_j$  are the precipitation rate, LWC and wind speed in the  $j^{\text{th}}$  hour of a storm lasting  $N$  hours.

Equation (2.18) shows that the uniform radial ice thickness in the simple model is independent of cylinder diameter. Jones' simple model for a horizontal circular cylinder is based on three assumptions. First, the collection efficiency of the rain droplets reaching the cylinder is 1; this indicates that all the water remains on the cylinder, and that there is no shedding of the water from the upper and lower halves of the cylinder. Secondly, all the rainwater impinging on the cylinder freezes, in other words, the freezing factor is equal to 1, and ice growth is dry rime. Thirdly, the model assumes that ice growth is

circular and uniform, which means that the model disregards the icicles and asymmetric ice growth.

Figure 2.1 shows a comparison of the results obtained using Jones' model (1996) and Chaîné and Castonguay's model (1974). This comparison reveals that predictions of ice

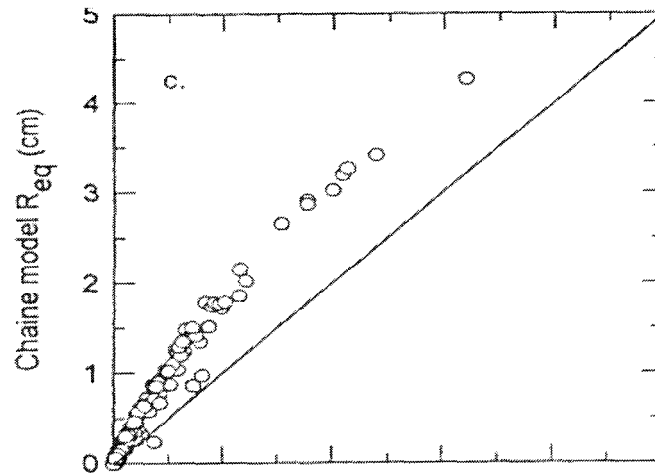


**Fig.2.1** shows a comparison of the results obtained using Jones' model (1996) and Chaîné and Castonguay's model (1974),Ref:6.

thickness made by Chaîné and Castonguay's model are twice those of the Jones simple model for  $R_{eq}$  of less than 1cm, and the accreted radial ice layer calculated by the former model is approximately 1 cm thicker than that calculated by the latter model when the  $R_{eq}$  is greater than 1cm.

### 2.2.6 The Icing Clock Model - based of the work of Poots( Ref:29)

"The Skelton and Poots (1988) icing clock model was developed to study the accretion of a beam of icing particles on a circular cylinder, which rotates at a constant angular velocity. The model is directly applicable to wet snow accretion"[Ref 25]. In Figure 2.2, a schematic representation of 12 icing nodes that form the icing clock is

shown. Fixed Cartesian coordinates  $(x, y)$  are chosen with the origin at the centre of the cylinder.

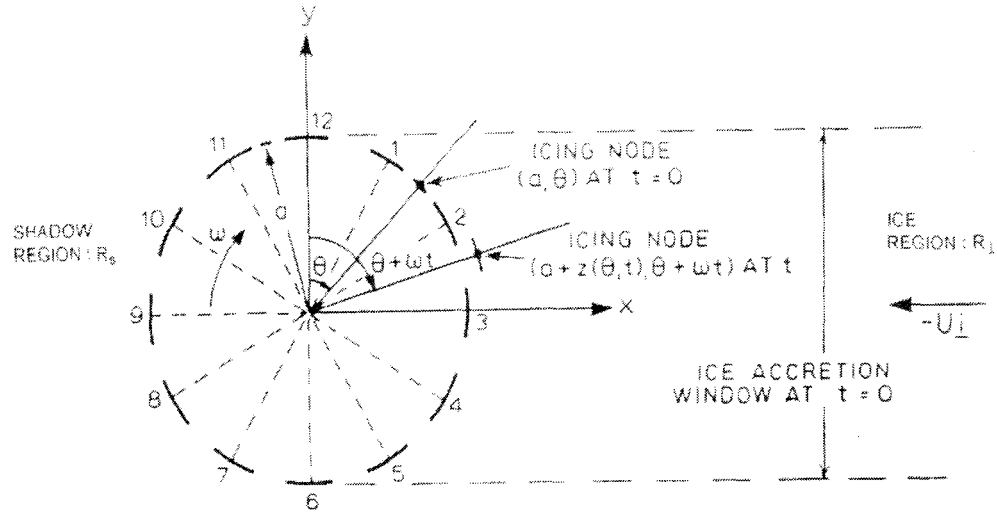


**Fig. 2.2.** *The icing clock model (Skelton and Poots, 1988).*

“For  $t \geq 0$  the cylinder rotates clockwise at an angular velocity  $\omega$ . An icing node will be located at  $(a + z(\theta, t), \theta + \omega t)$ , having polar coordinates  $(a, \theta)$  at time  $t=0$ , where  $\theta$  is an angle measured clockwise from the  $y$ -axis. Here,  $a$  is the radius of the bare cylinder and  $z(\theta, t)$  is the thickness of the snow measured radially outwards. The evolution of the ice accretion surface can be determined by considering an icing node as it rotates through regions of icing and shadow in turn. The ice region is a channel in the flow domain bounded upstream by the ice accretion window. An icing node, initially at  $\theta \in \pi$ , will be in the shadow region,  $R_s$ , for a duration of time  $t \in [0, (R-\theta)/\omega]$  and for  $t \in [(2\pi-\theta)/\omega, 2\pi/\omega]$ , when ice is deposited. For the period  $t \in [(\pi-\theta)/\omega, (2\pi-\theta)/\omega]$ , no snow is deposited on the node, and it is said that the node is in the shadow region  $R_s$ . For  $t \in [(2\pi-\theta)/\omega, 2\pi/\omega]$ , the snow node again is in the icing region  $R_i$  and snow is accreted during this period.

Throughout one whole revolution, each icing node  $\theta \in [0, 2\pi/\omega]$  will be in  $R_I$  and  $R_S$  for the same amount of time,  $\pi/\omega$  [Ref: 25].

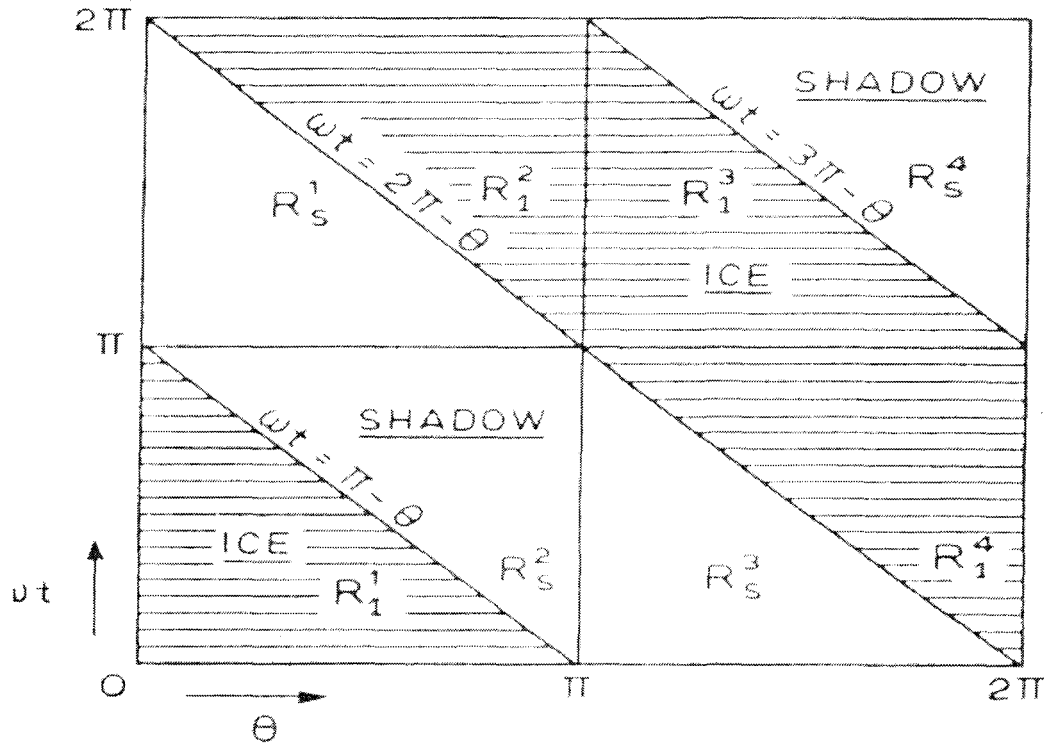


**Fig. 2.3.** The domain of integration of icing nodes  $\theta \in [0, 2\pi)$  during one revolution (Ref: 35)

## 2.3 Numerical Models

### 2.3.1 Porcu and Prodi 2-D Stochastic Model

2-D modelling of ice accretion on wires, as presented by Porcu and Prodi (1993), is a stochastic model in order to simulate atmospheric ice accretion at low values of impingement parameters. In the 2-D model of ice accretion on cylindrical objects, some aspects of fluid dynamics are introduced analytically, and a polydisperse spectrum of particles is used. The numerical experiments were carried out with different values of aerodynamic parameters, for a range of the Stokes number,  $K$ , from 1 to 7.8 and with two

different polydisperse droplet size distributions (DSD's). In this model, the actual curvilinear trajectory is not computed, but the angular position of the impinging droplet on the cylinder is stochastically determined on the basis of the local collection coefficients,  $\phi(\theta)$ , which is parameterized by means of the aerodynamic parameters, and based on the work of Lozowski et al. (1979). Because the motion of a droplet is partially determined by its radius-dependent inertia parameter, Porcu and Prodi (1993) computed a set of local collection coefficient,  $\phi_i(\theta)_x$  for each average angular position on the cylindrical object,  $\theta$ , while  $i$  represents the  $i^{\text{th}}$  value of the droplet radius in the discrete distribution.

Figure 2.4 shows the angular position of the icing surface. The probability,  $P$ , of a droplet of radius  $r_i$ , impinging on the surface of the cylinder at an angular coordinate  $\theta$ , is assumed to be  $P_i(x) \propto \phi_i(\theta)$ . As Figure 2.4 shows, from  $\theta$  it is possible to calculate the incidence angle  $\gamma$  at the point of impact, by using the relationship based on Langmuir and Blodgett (1949). Porcu and Prodi carried out the simulation of the 2-D model using 2 sets of parameters, as follows:

1.  $T=-20^{\circ}\text{C}$ ,  $P=785. \text{ mb}$ ,  $r_m = 9.0 \mu\text{m}$ ,  $R = 0.5 \text{ cm}$ ,  $2.5 < V < 20 \text{ m sec}^{-1}$ ;
2.  $T=-20^{\circ}\text{C}$ ,  $P=785. \text{ mb}$ ,  $r_m = 16.0 \mu\text{m}$ ,  $R = 0.9 \text{ cm}$ ,  $2.5 < V < 20 \text{ m sec}^{-1}$ ;

where  $r_m$  is the median volume radius of the size distribution, and  $R$  is the radius of the cylindrical collector. In this model, the trajectory of droplets is linearly approximated by the incidence angle  $\gamma$  near the surface in order to avoid the calculation of the whole particle path. Figure 2.5 shows numerical experiments with different values of the median radius of the particle distribution and different values of the Stokes number,  $K$ .

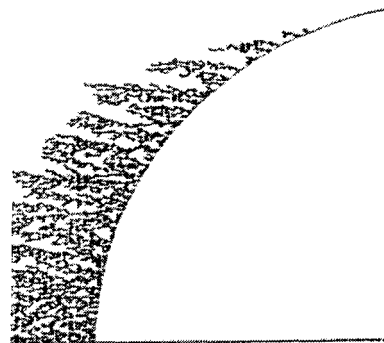
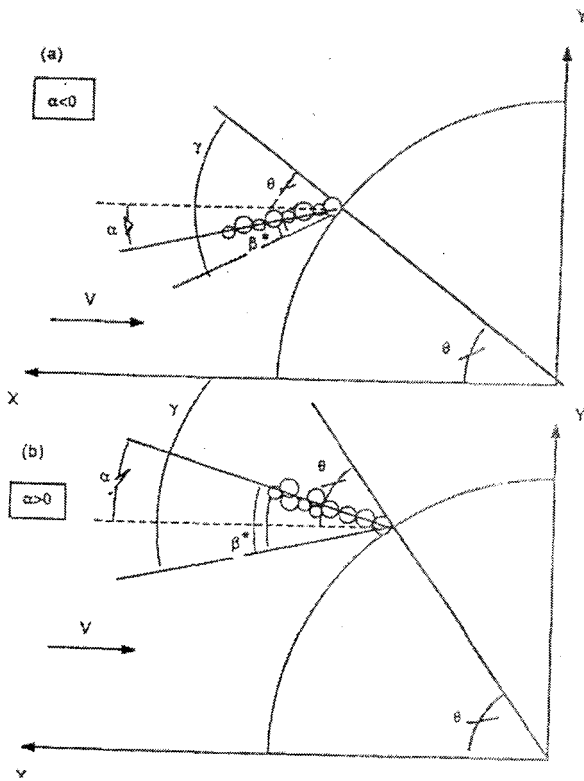


**Fig.2.5.** Example of numerical experiment with a specific value of the median volume droplet diameter (MVD) in the DSD

**Fig. 2.4.** Examples of different orientations and angular positions of a chain of impinging freezing droplets with reference to the icing surface

### 2.3.2 The Szilder and Lozowski, 3-D Random Walk Model

This model (Szilder and Lozowski, 1999) is a combination of ballistic trajectory and random walk models. The ballistic model determines the location of impact of the fluid elements, and the random walk model predicts their motion along the surface of the ice already formed on the object. A 3-D rectangular lattice is considered here for the accretion domain. Fluid elements are fired along straight vertical trajectories from a

random position above the cylinder. The random walk of a fluid element, which can be imagined either as many small drops or as a part of a single large drop, consists of a series of moves through the three-dimensional lattice. At each step, the fluid element may move one cell in any of six perpendicular directions, or it may freeze in place. The probability of motion in any direction is assumed equal. The model defines the motion parameter as the ratio of the probability of moving downward to the probability of motion in any other direction. Based on the previous numerical experiments carried out by Szilder and Lozowski (1995), the value of the motion parameter was chosen as 3.

The random walk of the fluid element may end in one of two ways: the first is freezing, process, which has its own specific probability; and the second is the occurrence of shedding.

### A. The Freezing Probability

Szilder and Lozowski (1999) defined the freezing probability as follows:

$$P_f = \frac{\pi}{2} \cdot \frac{q}{w \cdot \rho_w \cdot L_f} \cdot \frac{\Delta x}{R} \cdot P_c \quad (2.19)$$

where  $L_f$  is the latent heat of fusion ( $\text{J}\cdot\text{kg}^{-1}$ );  $q$  is the mean convective heat flux ( $\text{W}\cdot\text{m}^{-2}$ );  $w$  is rainfall rate ( $\text{m}\cdot\text{s}^{-1}$ );  $\rho_w$  is water density ( $\text{kg}\cdot\text{m}^{-3}$ );  $P_c$  is the probability of motion along the accretion surface;  $R$  is the cylinder radius (m); and  $\Delta x$  is the grid spacing (m).

The above relation (2.19) shows that the probability of freezing is a function of atmospheric conditions. Szilder derived this expression for a bare cylinder, but it may also be used during growth of the ice accretion.

## B. The Shedding Parameter

As in the freezing probability, Szilder and Lozowski (1999) expressed the shedding parameter,  $Sh$ , as a function of atmospheric conditions as follows:

$$Sh = \frac{M_c}{4 \cdot S \cdot \rho_w \cdot R \cdot \Delta t \cdot \left(1 - \frac{l}{L}\right)} \quad (2.20)$$

where  $\Delta t$  is the time step (s);  $M_c$  is the critical mass of a pendant drop estimated from the experimental data (kg);  $S$  is the icicle spacing (m);  $l$  is the distance from the upper stagnation line (m);  $L$  is the maximum distance from the stagnation line  $l \rightarrow L$ ; and  $Sh$  is the shedding parameter.

This expression (2.20) shows that the shedding parameter increases with the increasing length of the accretion. Such a result may be explained by the fact that, as the accretion grows, the amount of water which freezes on the side of the accretion increases; thus, there is a decrease in the number of fluid elements which reach the tip of the accretion. As the accretion length approaches the maximum length,  $l = L$ , the shedding parameter tends towards infinity, the critical mass of the pendant drop may be estimated from experimental data (see. Maeno and Takahashi, 1984; Chung and Lozowski, 1990). *Figures 2.6 and 2.7* show the same results as are predicted by the Szilder and Lozowski

model, (1999). *Figure 2.6* shows the influence of the convective heat flux on the accretion process; while *Figure 2.7* shows the influence of the rainfall rate on the accretion process.

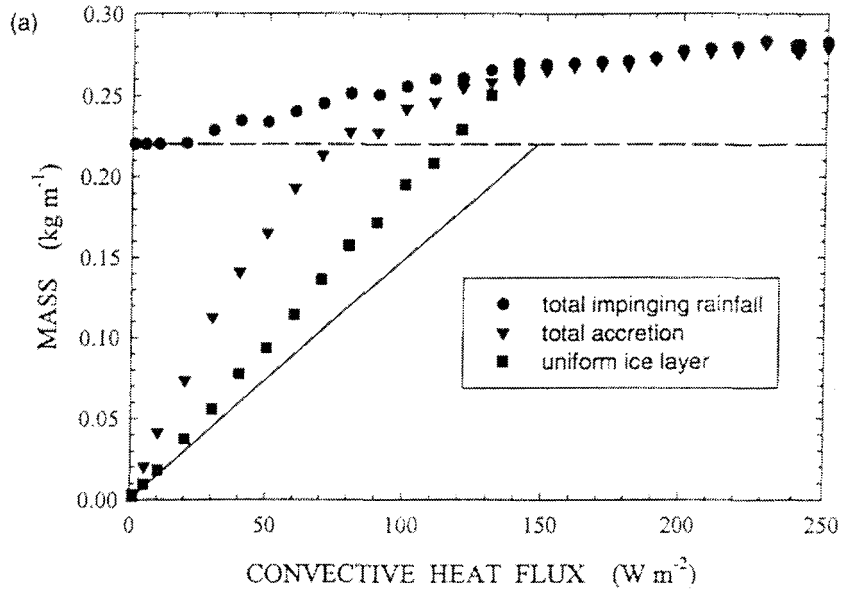


**Fig. 2.6.** Influence of convective heat flux on the accretion process

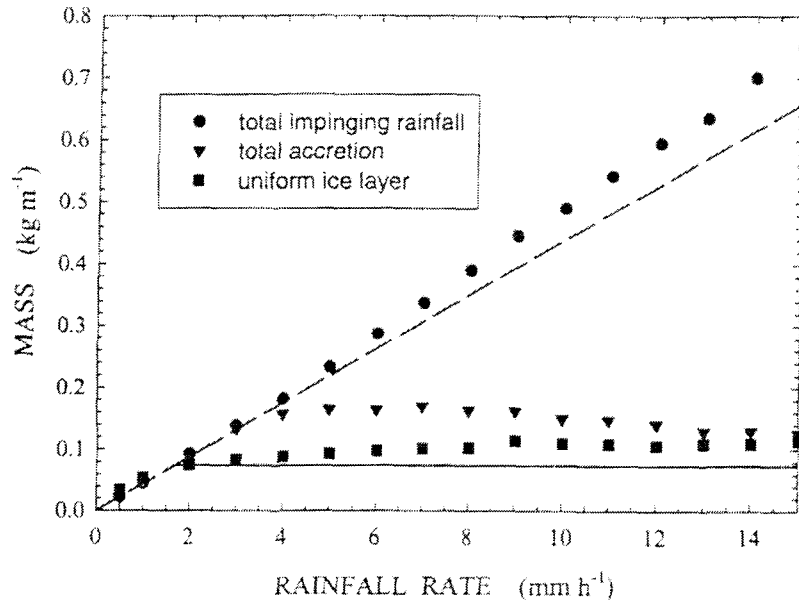


**Fig. 2.7.** Influence of rainfall rate on the accretion process.

### 2.3.3 The Lozowski, Stallabrass & Hearty Model

The numerical icing model created by Lozowski et al. (1979) was basically designed to study the atmospheric icing of fixed horizontal cylindrical objects under aircraft conditions, including high airspeeds and relatively low liquid water contents. This model was developed for conditions of mixed aerosol cloud containing supercooled water droplets and ice particles. For the first time, the effects of the non-freezing part of water or *runback water* on an icing surface flowing from an upstream control volume into a downstream and the effect of runback in heat and mass balance water were introduced and discussed in this model. Verification of the model in the icing wind tunnel (Lozowski et al., 1983) showed its very high level of predictability for moderate and high air speeds. This model occupies a classical position among icing models, and will be described in further detail in *Chapter 4*.

#### **2.3.4 The Makkonen Model**

Like Lozowski's model, the Makkonen model (1984) was also designed specifically for studying ice accretion on cylindrical objects. The aerodynamic parameters (LWC and air velocity) in the heat balance equation for the icing surface in this model is nearly the same as in Lozowski's model, although it also takes into account the time parameter in ice growth on cylindrical objects. In this model, a slow rotation (1 rpm) was given to a cylindrical icing object, in order to take into account the rotation of ice-covered cables and wires due to the combined effects of a wind and ice load. Unlike the Lozowski et al. model (1979), this one is not designed for mixed conditions, where small ice particles are considered in an air flow together with supercooled water droplets, and can be applied only to icing conditions under which only supercooled water droplets exist in a flowing air/aerosol stream. Further on, this model is described in greater detail in *Chapter 4*.

#### **2.4 Conclusion**

Among the variety of models studied in the first stage of this study, the models selected and presented in this section show an improved prediction capacity for ice accretion on cylindrical objects. Although the Imai model (1955) and the Goodwin et al. (1983) model were designed for ice accretion on operational power lines, a detailed theoretical verification of the models mentioned (Makkonen, 1996) reveals that their accuracy of prediction under conditions of moderate and extreme icing remains sub-optimal.

Lenhard's model (1955) tends to produce numerous errors in ice accretion prediction, while Chaîné and Castonguay's model (1974) provides only fair prediction performance under moderate icing conditions and poor prediction capacity under extreme icing conditions. This may be ascribed to the fact that the former model makes use of empirical equations that disregard the effects of ambient temperature on ice accretion, while the latter model does not make adequate calculation for the correction shape factor (k).

Makkonen's model (1984) was designed exclusively for cables and wires, and it shows good prediction capacity in moderate conditions and fair prediction capacity in extreme conditions. The Lozowski et al. model (1979) was not designed primarily for the prediction of ice accretion on operational power lines, but its generality makes it possible for researchers to examine the model under conditions of ice accretion on operational power lines.

The Szilder and Lozowski random walk model (1999) was designed originally for studying icicles. It is a hybrid analytical and random walk model, which includes empirically based freezing probability and shedding parameters. This model disregards the effects of wind on the accretion of ice on cylindrical objects.

From among the variety of models listed here, the Makkonen model (1984) and the Lozowski et al. model (1979) were selected for theoretical and experimental verification in this study of glaze ice formation, because both these models have a closer relation to the topic under study than the ones mentioned earlier. The second reason for such a selection is the fact that both models make use of common aerodynamic and thermodynamic relations. Thus, both models may be counted to the group of classical

atmospheric icing models. The most evident diversity in these models is their relation to the time factor: In the former model (Makkonen, 1984), the output of which is the amount of ice mass accreted over a specific time interval, the time dependence is incorporated indirectly, while the latter model (Lozowski et al., 1979) is a typically time-independent model. Further related studies (Szilder, Lozowski and Gates, 1987) tried to incorporate time dependence by recalculating the effect of succeeding accretion sizes and shapes on the heat transfer and collection efficiency on the output of the model after each time step. The model, when modified for application to anti-icing, marine icing and helicopter rotor-blade icing processes (Szilder, Lozowski and Gates, 1988), displays several improvements over the original. The over-simplification of the heat transfer process, which is completely unsteady by nature, however, does not allow for the ultimate application of the modified model as a quantitative forecasting tool. The second element of diversity in the selected models differs from the first in that its relation to the rotation of a horizontal cylinder is not the same. Taking into account the cylinder rotation in Makkonen's model and the incorporation of time dependence into it are two mutually related features of the process considered. The similarity and diversity of these models make a suitable base for comparing them under different icing conditions. The next chapter briefly presents the icing wind tunnel facility at the CIGELE, where both models were verified experimentally.

**CHAPTER 3**  
**THE CIGELE ATMOSPHERIC ICING RESEARCH WIND TUNNEL AND**  
**RELATED EQUIPMENT**

**3.1 INTRODUCTION**

The complexities inherent in the study of atmospheric icing phenomena occurring in the atmospheric boundary layer and involving ice accretion on structures make it a difficult task to solve. The absence of a final unified theory for understanding the mechanisms that trigger and halt the various types of ice accretion, as well as the impossibility of following its complete development in nature, make laboratory investigations of this phenomenon more productive than field observations. Such experimental modelling of atmospheric icing in a wind tunnel, or in a climatic room, is an integral part of examining the phenomenon that includes field measurements, theoretical and experimental modelling. In order to compare experimental, theoretical and natural data on atmospheric icing and to obtain a high degree of coincidence between them, the experimental modelling should simulate, as closely as possible, the weather conditions typically encountered during natural icing processes. Experimental modelling of these hazardous weather conditions involves maintaining the aggregate of meteorological elements forming these conditions within as wide a range as possible so as to be representative of all the types of atmospheric icing where possible. The aggregate under consideration is comprised of air speed; air temperature; air humidity; air pressure; liquid water content; and, droplet size distribution of the aerosol cloud. The wider the range of each meteorological element maintained in the tunnel, the wider the range of hazardous

weather conditions investigated, and, consequently, the greater the number of types of atmospheric icing which may be experimentally modeled in tunnel or climatic room facilities. This chapter provides an overview of a tunnel facility that is capable of covering a wide spectrum of atmospheric icing conditions.

### 3.2. Construction of Wind Tunnel and its Components and Systems

#### 3.2.1 General Description of Air Circuit

The CIGELE Atmospheric Icing Research Wind Tunnel (CAIRWT) is designed and built to model atmospheric icing experimentally as it occurs within a moving supercooled aerosol cloud with a velocity typical of air flow within the atmospheric boundary layer. The CAIRWT is a closed-loop (air-recirculated) low-speed icing wind tunnel with a total length of about 100 ft. (Figure 3.1). Icing conditions of different

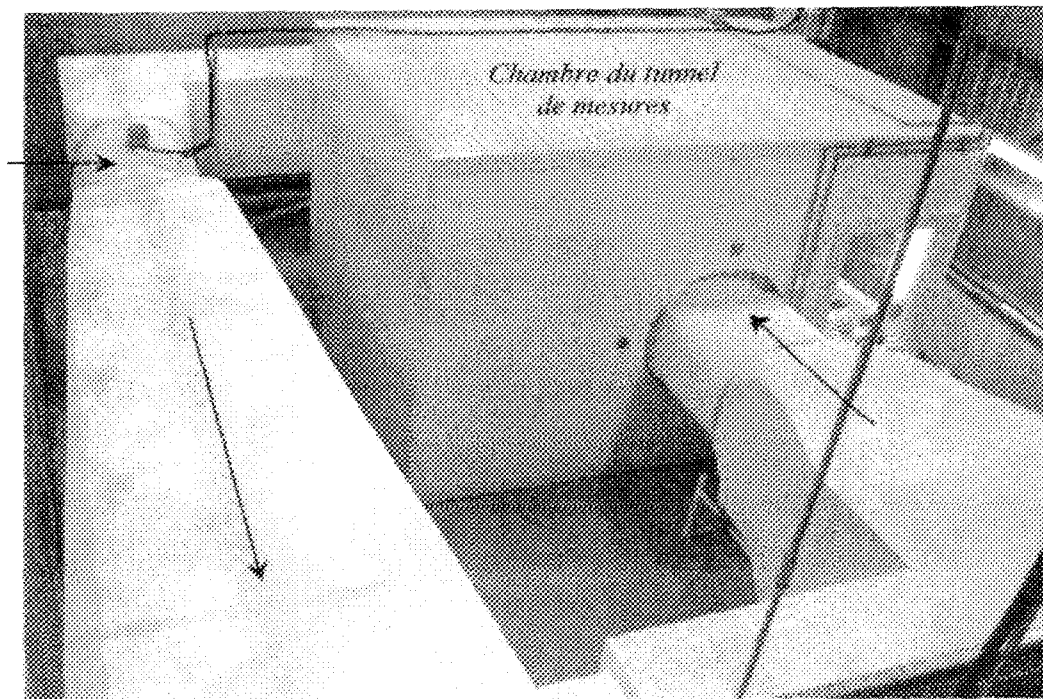


**Fig.3.1.** Upper View of CIGELE Wind Tunnel (longitudinal arrows show the air direction and horizontal arrow shows the RTD Position).



degrees of danger, as encountered during various icing processes in nature, are here simulated by controlling the above-listed meteorological elements inside the tunnel. A schematic diagram of the tunnel is presented in *Figure 3.2*. The construction consists of a number of consecutively connected segments of different shapes and cross-sections, forming a closed circuit for the recirculation of air inside it. The main segments (or sections) of the CAIRWT are: test section; diffusers; fan section; return passage section; cooling section; converging (or contraction) section; preparatory section and four corner sections (turning vane sections). Most of the segments are made of aluminium and covered on the outside by insulating material. The cross-section of each segment of the tunnel gradually narrows, widens or remains constant according to the functions performed by this segment in a circular air flow. The segments with downstream narrowing cross-sections are intended to cause an acceleration and contraction of the air flow producing its re-laminarization and decreasing the level of its free stream turbulence. To this group of segments belong the converging and preparatory sections, as well as the short fitting section ahead of the fan location. Four corner sections are designed to reduce loss of the velocity head by using turning vanes shaped like cambered airfoils. The sections with a downstream widening cross-section, or diffusers, are destined to recover the static pressure and to reduce the air speed before passing the segments containing the three main systems for maintaining the icing conditions inside the tunnel. The diffusers are usually located downstream of the test and fan sections. The first diffuser extending from the downstream end of the test section to the first corner beyond the test section is intended to receive the 'highly waked' air flow after it passes the icing object, and also to reduce flow velocity by expanding. The second diffuser,

called a return passage, is located between the fan section and the third corner, and is designed to continue expansion of the flow to a maximum in the total cross-sectional area. Increasing the area of contact between the air and the air exchanger makes it possible to obtain as effective an air cooling process as possible in the cooling section immediately beyond the third corner.

### **3.2.2. Test Section**

The most important segment of any icing wind tunnel is the part called the test section where the icing structure being analyzed is placed. The test section of the CAIRWT is 10 feet long with a constant rectangular cross-section 1.5 ft high and 3 ft wide (*Figure 3.3*). The width to height ratio (about 2) of the test section of the tunnel does not provide for minimum wall corrections; this is the result of a compromise made between the conditions with minimum wall corrections, imposing a ratio of 1.5 (Rae and Pope, 1984), and considerations of the cylindrical shape of the utility to be analyzed. The great length of the test section, as well as its relatively unchanging cross-sectional area, should serve to maintain constant most of the meteorological elements in this part of the tunnel. Small divergences in the wall of a closed jet (about  $\frac{1}{2}^\circ$ ) ensuring that constant static pressure is maintained (Rae and Pope, 1984, p.41) are not, however, preserved in this tunnel. This is due to the fact that, for this subsonic unpressurized wind tunnel, the non-maintenance of this condition may produce changes in the dynamic characteristics within the range of accuracy of their measurement only. A far more significant point influencing local velocity inside the test section is, in our opinion, the problem of blockage of flow by an icing body, an aspect which will be discussed in further detail in

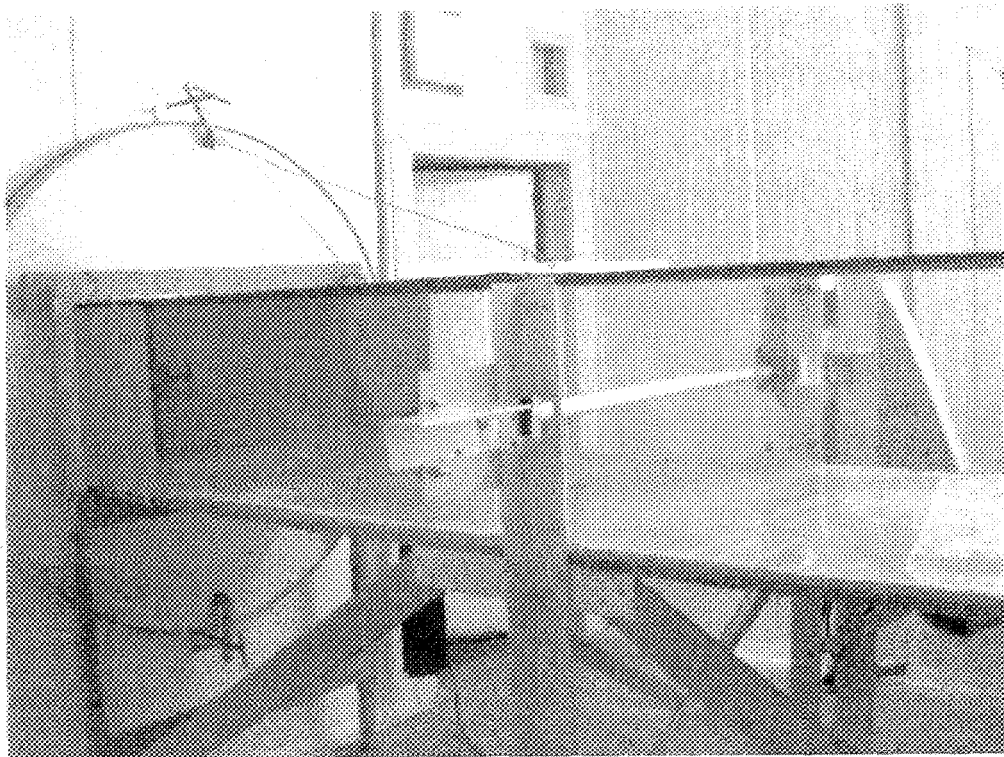


**Fig.3.2.** *Test Section of the CAIRWT*

Chapter 5. The walls, roof and floor of the test section are made of Plexiglas, used here in order to avoid the potential for creating additional turbulence due to rough surfaces. The smooth surface of the Plexiglas, therefore, makes it possible to obtain high quality air flow with a decreased level of turbulence. The transparency of Plexiglas also bypasses the need for installing observation windows to be used for flow visualization or taking photographs. The floor of the test section is fixed with silicone to a wooden base, which is used as a substrate in order to reinforce the entire construction. The Plexiglas plates are strengthened with aluminum rakes, and the joints between the plates are made of silicone to ensure that the section is tightly sealed. The body under observation can be placed inside the test section by opening its roof, which is composed of a two-part cover opening

out from the middle of the section to each of its sides. The edges of the covers and the tops of the walls are encased in  $\pi$ -shaped rubber stripping, which is used to provide a high level of adjacency between both covers and the tops of the walls. The entire test section is located inside a room 3.5-m long, 4.5-m wide and 3-m high, called the control room. This room may be used for: observation of the ice accretion process occurring inside the tunnel; preparation of the equipment to be used there for exposure to a supercooled aerosol cloud; various manipulations with the ice patterns already obtained; and to ensure optimum insulation of the test section from the outside. To ensure minimum heat exchange between the test section and control room, the latter is usually pre-cooled together with the tunnel before the experiment starts by opening one or both of the covers during tunnel pre-cooling procedures. After the covers of the test section are closed and before the beginning of the experiment, the temperature of the control room raises, from some minimal value close to the ambient temperature inside the tunnel, to some value, which is intermediate between the temperature inside the tunnel and outside the control room. The experiment may start once the temperature in the control room is stabilized relatively speaking.

### **3.2.3. Functioning and Regulation of the CAIRWT Systems Maintaining Ambient Conditions**

Experimental modelling of the meteorological elements creating icing conditions, called from now on dynamic and thermodynamic parameters for the purposes of laboratory investigation, is carried out by means of three main systems inside the wind tunnel: the fan system; the refrigeration system; and, the nozzle spray-bar system.

The air inside the tunnel is driven by a fan connected to a three-phase 45-kW motor by a frequency variation mechanism. Using a software programme, the frequency of the motor may be automatically set from 0 to 60 Hz, making it possible to change air speeds within the range from 0 to  $29 \text{ m s}^{-1}$ . With the activation of the fan by the computer, the cooling system may be started simultaneously, if the switch for this system on the control panel is set at 'on'. The air speed may also be adjusted manually.

The desired ambient temperature in the icing wind tunnel may be set by a remote temperature control system (Honeywell T 775A) with about  $\pm 1 \text{ }^\circ\text{F}$  accuracy. The nominal lower limit of the control device extends to  $-40 \text{ }^\circ\text{C}$ , although in practice, the minimum achievable ambient temperature in the tunnel is about  $-24 \text{ }^\circ\text{C}$ . The control device is connected to an RTD-type (Resistance Thermocouple Detector) temperature probe which is positioned inside the tunnel between the turning vanes and the honeycombs. This location for the temperature probe was chosen after a specially designed series of experiments was carried out, in which the performance quality of the RTD probe and its reaction to sudden changes in ambient temperature were checked by parallel monitoring of the same parameter in the test section of the tunnel. For this purpose, five T-type thermocouples were installed at different locations in the test section.

The coolant material in the refrigerating system is Ammonia ( $\text{NH}_3$ ) which is circulated by a 75 HP rotary compressor equipped with a condenser, an evaporator, a water pump, and a ventilator. The contact of the circulated moving air with the evaporator leads to a drop in air temperature. The temperature, which is sensed by the RTD, will be read in the tunnel by a PLC (Programming Logic Control) system. This is

an automated system, which controls the operation of the coolant gas compressor in order to set up the desired air temperature. The speed of the air flowing inside the tunnel has a significant effect on the time required to reach the desired air temperature and on the amplitude of air temperature oscillations inside the tunnel. These minimal oscillations in temperature were unavoidable throughout all experiments, as a result of the capacity of the system to regain the temperature desired after addition of the coolant to the cooler or heat exchanger. The higher speed reduces the set-up time and decreases the amplitude of the oscillations of air temperature, while the lower speed extends the set-up time and increases the amplitude of the oscillations of air temperature.

The technique used at CIRT to simulate atmospheric icing processes is to inject warm water into a cold air stream through the nozzles located at the trailing edge of the horizontal spray bar which is designed in the shape of an NACA 0012 airfoil (*Figure 3.4*)



**Figure 3.4.** *Spray-bar with the nozzles*

The spray bar is located just downstream of the honeycomb, 14.4 ft upstream of the middle of the test section, where the icing structure being analysed is usually placed. The water and air are supplied to the three nozzles on the spray-bar through the three independent water and air supply lines. This makes it possible to maintain specific conditions for each nozzle separately, without mutual influence between the lines. The water supply is linked to a reservoir of regular domestic tap water, while the air supply is provided by a compressor using ambient air. Water atomized in nozzles by high-pressure air is entrained by the air wake from the trailing edge into the flowing cooled air stream. As a result, an aerosol cloud of the desired droplet size distribution (DSD) is formed. The droplet size distribution of the aerosol cloud depends on the combination of air and water pressures, and, within a certain range of the thermodynamic parameters, on the flow rate of water in water supply line (Karev, Farzaneh and Mousavi 2002). The liquid water content (LWC) of an aerosol cloud formed in the tunnel is a function of the difference between the pressures in the air and water lines, air speed and, within a certain range of the thermodynamic parameters, on the flow rate of water in the water supply line. To maintain the aerosol cloud with the desired characteristics, it is necessary to control the dynamic parameters in both water and air lines from outside the tunnel. The control panel for monitoring and modulating the dynamic parameters in both lines is presented in *Figure 3.5*. The panel makes it possible to control the water flow rate, and the water and air pressures in three lines independently.

A droplet cloud, covering the distance between the spray-bar and the middle of the test section, undergoes noticeable transformation as a result of the processes of both

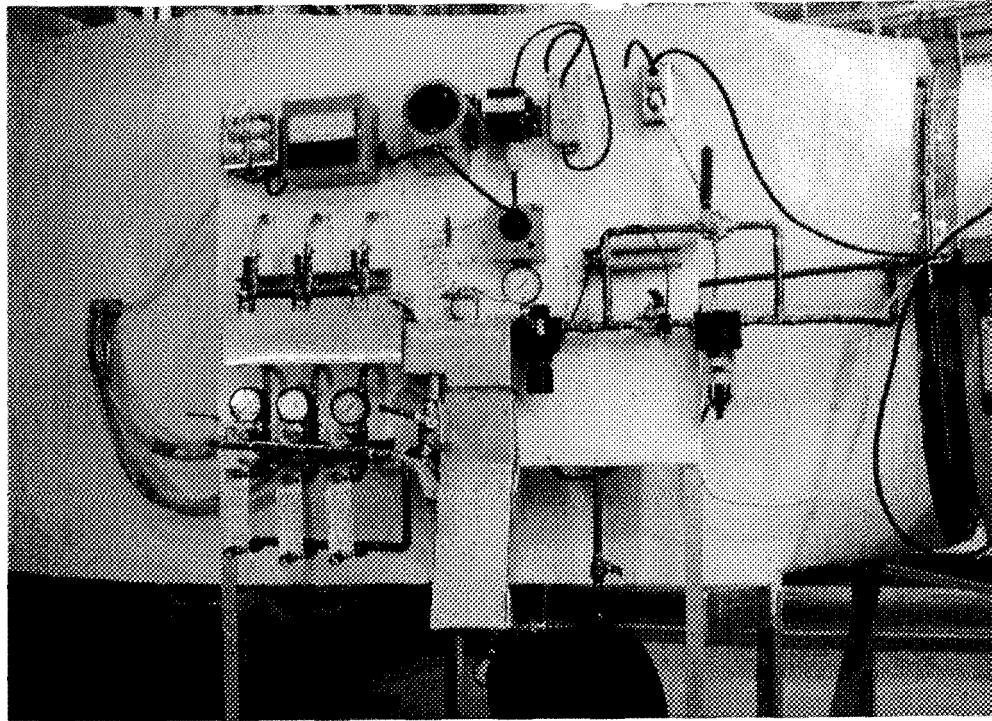


**Fig.3.5.** *Control panel for spray-bar*

heat and mass transfer, thereby becoming supercooled and producing additional water vapor in the gas phase.

### **3.3. Instrumentation**

#### **3.3.1. Air Speed**

A specially designed Pitot tube (Air Flow, UK) for taking measurements in the boundary layer was installed at the mid-point of the test section and connected to a precise differential pressure transducer (Omega, USA). The Pitot tube readings were transferred via this transducer and recorded on a computer using a standard data

acquisition system (InstruNet, United Electronics, USA). Due to the possibility of a dependence of these readings on the ambient air temperatures, the experimentally obtained relationship between the frequency of the AC engine in the CAIRWT and the air velocity was verified at various constant ambient temperatures (5, 0, -5, -10, and -20 °C). The greatest difference observed between results at 5 °C and at -20 °C was less than 2 % at an AC engine frequency of 56 Hz, which is close to its maximal value of 60 Hz. Throughout the duration of the experimental unit, the need for the simultaneous monitoring of air velocity was rendered unnecessary by using the relationship thus obtained. Before and after each icing experiment, the permanence of the streamwise component velocity and boundary layer profile were checked by using the same Pitot static tube. The streamwise component of air velocity was measured periodically in order to make sure that it remained constant (5 or 10 m s<sup>-1</sup>) throughout the experimental units and to ensure test repeatability with the same air speeds. The boundary layer profile of mono-phase air flow near the bottom of the icing wind tunnel was checked with the intention of maintaining repeatability as far as the level of free stream turbulence is concerned. More than four conceptual improvements were made to the construction of the tunnel in order to achieve as high a quality of the flow as possible (Karev and Farzaneh, 2002). A further goal during this dynamic calibration series was to ensure the relative permanence of the air speed in three different cases: firstly, when the test section of the tunnel was empty; secondly, when the bare horizontal cylindrical body was placed inside the test section; and, thirdly, when this cylindrical structure had already undergone the icing process over the duration of the experimental unit. The results of measurements

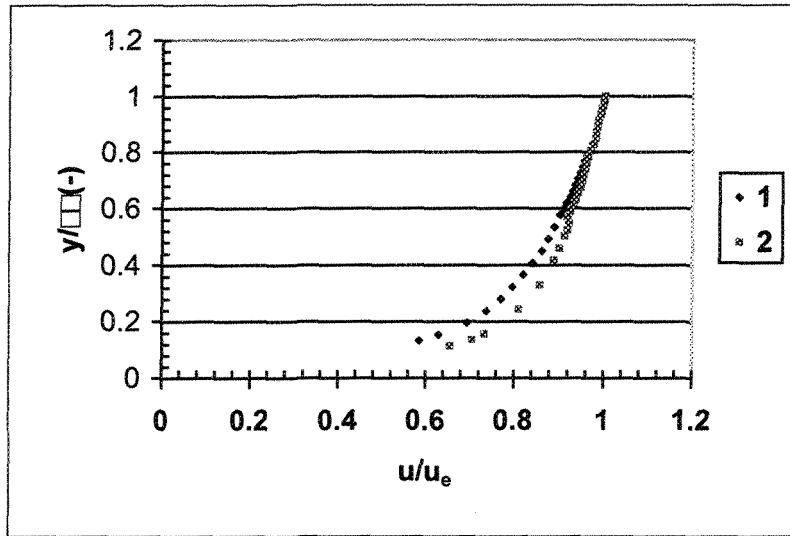


**Fig. 3.6** Boundary layer profiles in test section for two cases: 1. without cylinder inside tunnel, 2. with cylinder inside tunnel.

of air velocity, in two of the three cases mentioned, are presented in *Figure 3.6*. This form of investigation was required in view of the fact that the large-size icicles growing at a high rate of water supply to the surface of the cylinder tend to partially block up the lower half of the tunnel cross-section over the duration of the experimental unit. This may result in an increase in air speed as the icicles increase in size, reinforcing the stripping of water droplets from the surface of the ice accretion and creating additional turbulence in the air flowing past the surface.

### 3.3.2 Air Temperature

The tunnel is equipped with T-type copper/constantan thermocouples, for the measurement of air temperatures. The thermocouples, installed in the two covers in the ceiling of the test section, at the entrance, mid-point and exit point, provide the data on variations in air temperature at these three sites throughout each experiment.

### 3.3.3. Absolute and Relative Air Humidity

Due to the fact that the CAIRWT is not a strictly pressurized icing wind tunnel, the air pressure was not one of the thermodynamic parameters monitored and recorded over the duration of the experiments. It is assumed that all experimental data were collected under conditions of constant static pressure, which is equal to the pressure of 1 NACA Standard Atmosphere at sea level ( $p_{st}=101325 Pa$ ). The air humidity was, however, initially considered as one of the significant thermodynamic parameters, which required monitoring throughout the experiments. The absolute humidity,  $AH (gm^{-3})$ , and the relative humidity,  $\Phi_a(-)$ , were measured using a humidity probe (“Smart” Humidity transmitter, Vaïsa) which was placed inside a plastic/aluminium fairing specially designed to resist freezing. The probe was then set on a rack and introduced through the wall of the tunnel at a 4 ft-distance downstream of the mid-point of the test section, half-way up the cross-section height. Changing the position of the probe with respect to the middle line of the test section makes it possible to obtain the lateral distribution of air humidity, which has proved to be an important factor influencing the final shape of the ice accretion. The air humidity at the middle line of the test section was, however, found to be relatively constant over each specific experiment and repeatable to an acceptable degree when the values are compared over the various experimental units.

### 3.3.4. LWC and DSD of the Aerosol Cloud

The LWC was measured at the centre of the cross-section of the test section using accepted standard techniques such as the rotating icing cylinder method (Stallabrass, 1978). The uniformity of the LWC field at all other points in the cross-section of the test

section was measured by using another accepted standard technique called the circumference of ice accretion method (Ide, 1990). For the measurement of DSD using the collargol slide impact method (Godard, 1960), a special tool for collecting droplets was designed by at CIGELE based on the one proposed by Du (1987) and including several functional innovations. This version of the cylindrical impact droplet sampler is a horizontal cylinder covered with an aluminium pipe which slides under the influence of a compressed spring. The outer diameter of the sliding part is 1½ inches; a small slide (1½ inches long by ¾ inches wide) is placed inside the horizontal cylinder. The aluminium pipe has a rectangular opening for exposing the slide to the two-phase flow. Exposure time can be regulated by adjusting the force of the spring.

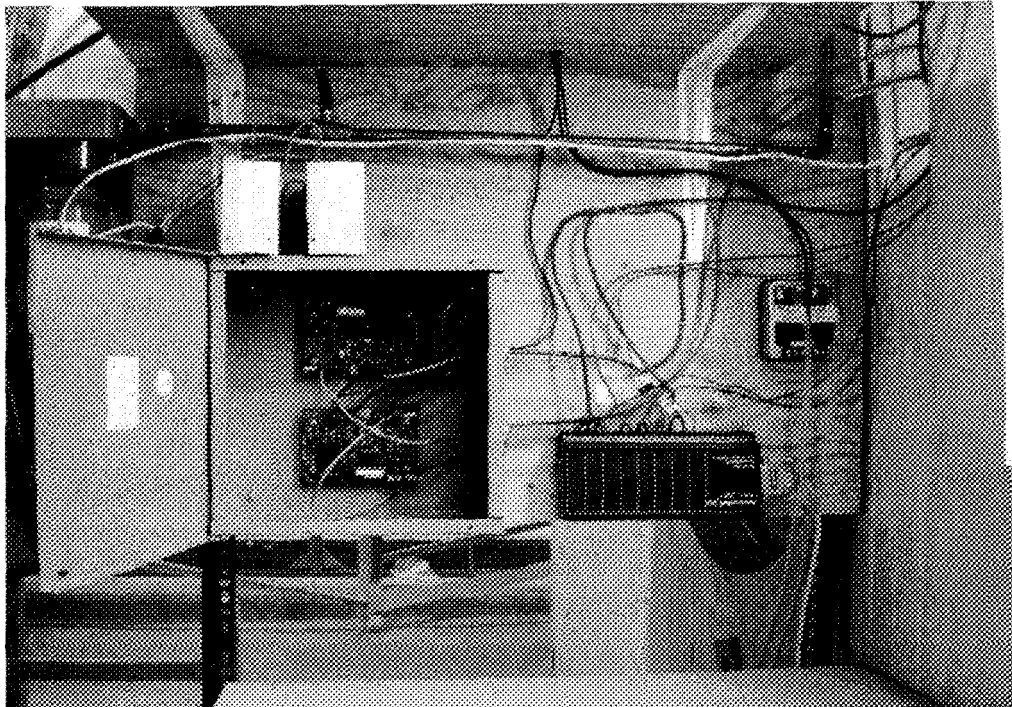


**Fig. 3.7.** *Data Acquisition System*

### **3.3.5. Data Acquisition System**

During the calibration phase and performance of the main tests, the physical effects that were sensed by the thermocouples, the humidity meter and the manometers, were transmitted by electrical pulses to a Data Acquisition System (DAS). *Figure 3.7.* shows the DAS of the InstruNet (United Electronics, USA).

The procedure for the application of all techniques mentioned in this study will be described in Chapter 5.

## **CHAPTER 4**

### **DESCRIPTION OF THE LOZOWSKI ET AL. MODEL (1979) AND THE MAKKONEN MODEL (1984)**

#### **4.1. Introduction**

Each typical model of ice formation on a structure embedded within a flowing aerosol cloud is compounded of two significant and mutually interdependent mathematical parts called the aerodynamic and thermodynamic components. The former deals with the flow of the aerosol particles, while the latter concerns the thermodynamic aspect of growing ice surfaces. The main output of the aerodynamic aspect is the collection efficiency of icing surfaces as it determines which part of the aerosol reaches the icing surface. In the thermodynamic aspect, the most important output is the freezing factor determining which portion of the impinging droplets converts into ice. This chapter will deal with the presentation of two selected icing codes and their comparison in the light of the natural processes occurring around and on the icing surface.

#### **4.2. Lozowski et al. (1979) Icing Code**

##### **4.2.1 General Structure**

The Lozowski et al. (1979) model is a classic two-dimensional icing model dealing with the flow of a supercooled mixed aerosol cloud around a non-rotating horizontal cylinder. The collection efficiency of this model is calculated based on the results of Langmuir and Blodgett (1946). The thermodynamic aspect of the ice accretion around the cylinder leads to the heat balance equation of an icing surface in a state of equilibrium,

proposed initially by Messinger (1953). The equation is solved for each 5-degree angular interval around the cylinder, and deduces the temperature of the equilibrium surface and the fraction of water that freezes in each angular sector. The model assumes that the water droplets remain in a liquid state after they reach the icing surface where during their spreading they form a water film which begins to freeze from below. It is also assumed that the total runback water that reaches the last angular sector will shed into the airflow. For conditions with mixed aerosol flow, when the cloud consists of supercooled water droplets and ice crystals, the model supposes that the ice crystals stick uniformly to the icing surface if the ice growth regime is wet, i.e. the temperature of the surface is about 0°C. This condition was defined by Cansdale and McNaughtan (1977) and does not take into account any other type of interaction between the icing surface and ice crystals.

#### **4.2.2 Input and Output Parameters of the Model**

The following are the input parameters in the model: air pressure; air velocity; air temperature; and liquid water content (LWC) in the airflow. The heat convection coefficient is chosen either for a smooth surface or a rough surface. Several types of output obtained from the model may be divided into groups according to the part of the model to which they are related. The aerodynamic outputs are: local collection efficiency,  $B$ ; total collection efficiency,  $E$ ; and, maximum angle achievable by droplets of a given diameter, as measured from the contact line. The thermodynamic outputs calculated for each angular sector of the cylinder are: the temperature the icing surface,  $t_s$ ; the freezing fraction of water,  $n$ ; different forms of heat conduction and convection; icing flux,  $R$ ; and

runback water flux,  $R_w$ . Runback water is the part of the water in each sector that remains in a liquid state and moves from one sector to a neighbouring sector.

In *Chapter 5*, the entire procedure will be discussed in detail using model outputs to obtain the final ice load in an icing tunnel for a certain time interval,  $\Delta t$ . Here, however, we will limit discussion to ways of using icing flux to obtain ice mass only. Generally, when the temperature of the icing surface is below zero, i.e.  $t_s < 0$ , the droplets impinging on the icing surface freeze immediately upon contact with the icing surface without first spreading over it. The ice growth regime, in this case, is called a dry icing regime, and the direction of the ice build-up growth, called hard rime, is assumed to be parallel to the air flow. The ice thickness in the direction parallel to the air flow at any angular location from the stagnation line may be expressed as follows:

$$h_i = \frac{R\Delta t}{\rho_i \cos \theta} \quad (4.1)$$

where  $R$  is the icing flux obtained by the model;  $\theta$  is the angle from the stagnation line for which the calculation is made;  $\rho_i$  is the density of the growing ice layer, which is lower than maximal ice density; and,  $\Delta t$  is the duration of the icing event.

Alternatively, when the temperature of the icing surface is  $0^\circ\text{C}$ , the impinging droplets do not freeze immediately upon contact with the icing surface, but form a thin water film by collision and spreading, which may be put into motion after its subsequent thickening. The ice growth regime, in this case, is called a wet icing regime, and the direction of ice formation is radial. The thickness of the ice in a radial direction is then defined as follows:

$$h_r = \frac{2R\Delta t / \rho_i}{1 + \sqrt{1 + 4R / \rho_i D}} \quad (4.2)$$

where  $D$  is the cylinder diameter. The ice density is assumed to be constant and equal to  $920 \text{ kg m}^{-3}$  for this wet icing regime. By finding the thickness of the ice for each angular position, it is possible to obtain the ice accretion profile for each sector from zero to  $90^\circ$ . Since concept of collection efficiency is one of the principal for understanding both models, several fundamental studies related to it will be discussed in a separate section.

### 4.3 Collection Efficiency

#### 4.3.1 General Concept and Theory of Collection Efficiency

Seminal studies by Taylor (1940), and by Langmuir and Blodgett (1946), have laid the foundation for the concept of the impingement of icing particles on structures, and in recent years, for the theory of the inertial depositing of aerosol particles on objects. The collection efficiency,  $E$ , for a stream of particles moving horizontally towards a circular cylinder placed perpendicular to the airflow is defined as the ratio of two quantities. The first is the mass of impinging particles on the upstream portion of the cylinder, while the second is the mass that would be experienced by the surface if the particles had not been deflected by the effects of the air stream. The trajectories of the particles released as a result of velocity are called the grazing trajectories with reference to the surface; consequently, particles released upstream will collide with the cylinder surface. In a similar fashion, if  $l$  is the upstream height of a grazing trajectory on a sphere, then the collection efficiency is defined as the ratio of the actual collision cross-section to the frontal cross section of the sphere, or  $\pi l^2 / \pi r_0^2$ , where  $r_0$  is the radius of the sphere.

### 4.3.2 Taylor Work (1940) on Collection Efficiency- based of the work of Poets

(Ref: 30)

“This study was concerned with a wartime project on the design of an icing wind tunnel to investigate the icing and de-icing of aircraft wings. Taylor was interested in determining conditions under which the trajectories of droplets retained dynamic similarity when the diameter, the speed, or the density of the droplets was changed. For simplicity, Taylor (1940) considered the deflection of droplet trajectories in attached potential flow (APF) past a circular cylinder. By assuming the Stokes drag force, the vector equation for the motion of the droplet becomes:

$$\frac{4}{3}\pi r_d^3 P_d \frac{dv^*}{dt} = 6\pi\mu_a (v - v^*) \quad (4.3)$$

subject to the boundary condition

$$v^* \rightarrow u_i \text{ as } |r| \leq \infty \quad (4.4)$$

Introducing the dimensionless variables  $V^* = v^* / U$ ,  $V = v / U$ ,  $\tau = Ut / r_0$ ,  $R = r / r_0$

Equations (4.3) and (4.4) reduce to

$$St \cdot dV^* / d\tau = (V - V^*), \quad V^* \rightarrow u_i \text{ as } |R| \rightarrow \infty \quad (4.5)$$

and  $St = \frac{1}{9} \frac{P_d}{P_a} \left( \frac{r_d}{r_o} \right)^2$  Re is known as the Stokes number. Thus, Taylor established that

different droplet trajectories are dynamically similar for the same value of  $St$ ”[Ref: 30].

### 4.3.3 Work of Langmuir and Blodgett (1946) on Collection Efficiency- based of the work of Poots( Ref:30)

“The motivation for this study was to investigate in-cloud icing on aircraft wings. Once again the flow regime of APF past a circular cylinder was employed for simplicity. In practice, the droplet Reynolds number  $Re_d \gg 1$ , and therefore the Stokes drag formula, as used by Taylor (1940), was replaced by the empirical formula:

$$C_D Re_d / 24 = 1 + 0.197 Re_d^{0.63} + 2.6 \times 10^{-4} Re_d^{1.38} \quad (4.6)$$

which was provided by Goldstein (1938). The numerical solution to the vector equation of motion for a droplet is:

$$\frac{4}{3} \pi r_d^3 P_d \frac{dv^*}{dt} = 6\pi \mu_a r d (v - v^*) (C_D Re_d / 24) \quad (4.7)$$

subject to boundary condition (4.4) and carried out by using a differential analyzer.

From the trajectory calculation of the collection efficiency of the cylinder ( $E$ ), local collection efficiencies at points on the surface are deduced as a function of  $U$ ,  $r_d$  and  $r_0$ . These results may be used to determine the rate of the impingement of droplets on the windward side of a non-iced cylinder, and thus provide the initial icing intensities of ice accretion. The theoretical data, based on droplet impact velocities, as compiled by Langmuir and Blodgett, have now become central to the construction of icing models for in-cloud icing”[Ref: 30]. Because this present research is restricted to the Makkonen model (1984) and to the Lozowski et al. (1979) model, the following sub-section (4.3.4)

will describe the collection efficiency of the latter, while the collection efficiency of the former will be described in a later sub-section (4.6).

#### 4.3.4 Lozowski et al. (1979) on Collection Efficiency- based of the work of Lozowski et al ( Ref:19)

“Considering that the collection efficiency in this study is a function of angles around the cylinder, the upwind face is divided into angular sectors, each  $5^\circ$  in width and centred on angles  $\theta_i = 5i^\circ$ ,  $i = 0, 1, 2, \dots, 18$ . Each sector has the same surface area per unit of cylinder length, but the component of the surface area normal to the undisturbed flow diminishes as  $\cos\theta_i$  changes. The droplet size is divided into nine diameter categories,  $j = 1, 2, \dots, 9$ . For the purposes of estimating collection efficiency, all the droplets in each size category are treated as if they had a centre value diameter,  $D_j$ . For each value of  $D_j$ , (i) the stagnation line collection efficiency,  $B_{0j}$ , (ii) the overall collection efficiency  $E_j$ , and, (iii) the maximum impingement angle  $\theta_{mj}$  are calculated according to the formulas established by Langmuir and Blodgett. In order to do this, three droplet parameters must first be evaluated. The droplet Reynolds number  $Re_j$  is defined by

$$Re_j = \frac{\rho_a U D_j}{\mu_a} \quad (4.8)$$

where  $\rho_a$  and  $\mu_a$  are the density and the dynamic viscosity of air, respectively, and  $U$  is the free stream speed. The non-dimensional inertia parameter  $K_j$  is defined by

$$K_j = \frac{2\lambda_{sj}}{D_c} \quad (4.9)$$

where  $\lambda_{sj} = \frac{\rho_w \mu S_j}{18 \mu_a}$ ;  $\rho_w$  is the droplet density,  $D_c$  is the cylinder diameter, and  $\lambda_{sj}$  is the droplet range when released as a projectile with initial velocity,  $\mu$ , into still air under the assumption that the Stokes approximation holds.

Since the Stokes approximation is not valid at the velocities which are of concern to this study, an adjustment to  $K_j$  must be made in order to permit the use of the results obtained using the approximation. Such an adjustment is made by defining the following:

$$k_{0j} = 0.125 + (k_j - 0.125) \left( \frac{\lambda}{\lambda_s} \right)_j \quad (4.10)$$

where  $\lambda$  is the actual droplet ballistic range, and where  $\left( \frac{\lambda}{\lambda_e} \right)_j = \frac{1}{1 + 0.0967 \text{Re}_j^{0.6367}}$

The above formula is an empirical formula, which is based on Langmuir and Blodgett (1946). Using  $K_{0j}$ , values of  $B_{0j}$ ,  $t_j$  and  $\theta_{mj}$  may be calculated according to”[Ref: 19]:

$$B_{0j} = E_j = \theta_{mj} = 0 \quad K_{0j} < 0.125 \quad (4.11)$$

$$B_{0j} = \frac{1.4(K_{0j} - 0.125)^{0.84}}{1 + 1.4(K_{0j} - 0.125)^{0.84}} \quad 0.125 \leq K_{0j} < 7.5 \quad (4.12)$$

$$B_{0j} = \frac{K_{0j}}{1 + K_{0j}} \quad 7.5 \leq K_{0j} \quad (4.13)$$

$$E_j = 0.489(\log(8K_{0j}))^{1.978} \quad 0.125 < K_{0j} < 0.9 \quad (4.14)$$

$$E_j = \frac{K_{0j}}{\frac{\pi}{2} + K_{0j}} \quad 0.9 \leq K_{0j} \quad (4.15)$$

$$\theta_{mj} = \tan^{-1}(1.7(K_{0j}-0.125)^{0.76}) \quad 0.125 < K_{0j} < 10 \quad (4.16)$$

$$\theta_{mj} = \tan^{-1}K_{0j} \quad 10 \leq K_{0j} \quad (4.17)$$

“In order to calculate the variation of the collection efficiency using the angles around the cylinder for each droplet size, the relation given below was formulated:

$$\beta_j(\theta_i) = \beta_{ij} = \beta_{0j} \cos\left(\frac{\pi \theta_i}{2 \theta_{mj}}\right) + \frac{\pi^3}{\theta_{mj}^3 (\pi^2 - 4)} \left( t_j - \frac{2\theta_{mj}\beta_{0j}}{\pi} \right) \left( \theta_i^2 \sin\left(\pi \frac{\theta_i}{\theta_{mj}}\right) \right) \quad (4.18)$$

for  $\theta_j < \theta_{mj}$  and  $B_{ij}=0$  for  $\theta_j > \theta_{mj}$ . This equation satisfies the physical constraints

$$B_j(0^\circ) = B_{0j}, B_j(\theta_{mj}) = 0 \text{ and}$$

$$E_j = \frac{1}{\theta_{mj}} \int_{\theta}^{\theta_{mj}} \beta_j(\theta) d\theta$$

(4.19)

The overall collection efficiency for each sector is the mass-weighted mean overall droplet size categories:

$$\beta(\theta_i) = \beta_i = \sum_{j=1}^9 f_j \beta_{ij} \quad (4.20)$$

where  $f_j$  is the fraction of the total droplet mass flux in the undisturbed flow consisting of droplets in the  $j^{\text{th}}$  size category; and the liquid water mass flux ( $\text{kgm}^{-2}\text{s}^{-1}$ ) impinging on each sector is

$$R_{wi} = B_i U w \quad (4.21)$$

where  $w$  is the volumetric concentration in  $\text{kgm}^{-3}$  of liquid water in the airflow (LWC)"[Ref: 19].

#### 4.4 Steady State Heat Balance Equation

Based on the Messinger (1953) approach for the heat balance of the accretion surface which is in thermal equilibrium with the ambient surroundings, or, in other words, by equating the sum of all heat sources to the sum of all heat sinks, Lozowski et al. (1979) were able to proposed the seven following heat terms as will be discussed below.

Heat sinks include: i) conduction and convection through the cylinder boundary layer,  $Q_{cc}$ ; ii) latent heat transfer due to evaporative and sublimate mass transfer through the boundary layer,  $Q_e$ ; iii) warming of the accreted water to the equilibrium surface temperature,  $Q_d$ ; iv) conduction into previously deposited ice and along the cylinder itself,  $Q_i$ . For the sake of simplicity, the term 'heat sinks' was disregarded by authors.

Heat sources include: v) latent heat of freezing at the equilibrium surface temperature,  $Q_f$ ; vi) aerodynamic heating due to adiabatic compression of the air and viscous work in

the boundary layer,  $Q_v$ ; vii) kinetic energy of the impinging droplets,  $Q_k$ . The authors mentioned that, under certain circumstances, the heat transfer may be significant due to the shedding of water, whether by splashing or melting. Based on these assumptions, the heat balance equation may be written as:

$$H(t_a - t_s) + H \left( \frac{\text{Pr}}{\text{Sc}} \right)^{0.63} \frac{\alpha_v}{\rho C_p} (e_a(t_a) - e_s(t_s)) + R_w \bar{c}_w (t_a - t_s) + n R_w l_f(t_s) + \frac{1}{2} \frac{H r_c \mu^2}{C_p} + \frac{1}{2} R_w \mu^2 = 0 \quad (4.22)$$

The above-listed terms in the heat balance equation will now be presented in greater detail.

i) The first term describes heat loss by convection and conduction into the air,  $Q_{cc} = H(t_a - t_s)$ , where  $t_a$  is the air temperature;  $t_s$  is the temperature of cylinder surface;  $H$  is the convection coefficient in terms of the dimensionless Nusselt number  $Nu$ .  $H$  is given by  $k_a D_c^{-1} Nu$ , where  $k_a$  is the thermal conductivity of air, and  $D_c$  is the cylinder diameter. In general, the Nusselt number is a function of the following factors: the angle around the cylinder,  $\theta$ ; the Reynolds number for the cylinder,  $\text{Re}_c = \frac{U D_c \rho_a}{\mu_a}$ ; the cylinder roughness

(if any), which is characterized by the ratio of the roughness height to the cylinder diameter; the Prandtl number of the fluid (a constant for air and equal to 0.71); and, the level of free stream turbulence. For a smooth cylinder in a non-turbulent air stream (~ 1% turbulence intensity), the Nusselt number from Achenbach's (1974) data may be approximated by the relation:

$$Nu = R_c^{0.5} \left( 1 - \left( \frac{2\theta}{\pi} \right)^3 \right) \quad (4.23)$$

Based on the results from Achenbach (1974), the following equation is applied for local heat transfer from a cylindrical rough surface:

$$Nu = R_c^{0.5} (2.4 + 1.2 \sin(3.6(\theta - 25^\circ))) \quad (4.24)$$

“The roughness of an icing cylinder depends on the local character of the ice accretion, where, if the surface is dry, ( $t_s < 0^\circ\text{C}$ ). The deposit is generally smooth except near the edges where ice feathers tend to develop. If the droplets freeze individually rather than coalesce before freezing, then the roughness parameter for such a surface would likely be of the same order of magnitude as the ratio between the median volume droplet (MVD) diameter and the cylinder diameter, or about  $10^{-3}$ . When the accretion becomes wet ( $t_s > 0^\circ\text{C}$ ), and a film of runback water covers part of the surface, the roughness of the ice deposit increases. The roughness parameter will then be a function of  $\theta$ , and experiments indicate values as high as  $10^{-1}$  depending on how the dimensions of the roughness elements are defined”[Ref: 19].

ii) The second term in equation (4.22) describes the latent heat transfer due to evaporative and sublimate mass transfer through the boundary layer. This term may be written in the following form:

$$Q = H \left( \frac{\text{Pr}}{\text{Sc}} \right)^{0.63} \frac{\epsilon l_v}{PC_p} [e_a(t_a) - e_s(t_s)] \quad (4.25)$$

where  $Pr$  is the Prandtl number for air which is equal to 0.71;  $Sc$  is the Schmidt number which is equal to 0.595;  $\varepsilon$  is the ratio of the molecular weight of water vapour to dry air, which is equal to 0.622;  $P$  is the static pressure in the air stream;  $C_p$  is the specific heat capacity of dry air at constant pressure;  $e_a$  and  $e_s$  are the saturation vapour pressure of moist air at local temperatures above the boundary layer and at the equilibrium surface;  $l_v$  is the specific latent heat of vaporization. Since there may be both ice and liquid water on the surface at any given time, the appropriate latent heat is that of sublimation or of vaporization, or a combination of both. “ Even at equilibrium surface temperatures somewhat below 0°C, a water film may exist on the surface because of the finite length of time required for total freezing of the impinging droplets. In view of this, and in order to avoid a discontinuous transition between the latent heat of vaporization and sublimation, Lozowski et al. (1979) have chosen to use the latent heat of vaporization in this term under all conditions”[Ref: 19].

iii) Heat transfer due to warming of the accreted water to the equilibrium surface temperature

$$Q_w = R_w C_w (t_a - t_s) \quad (4.26)$$

where  $R_w$  is the mass of water which impinges on each angular sector and is defined by equation (4.21).

iv) Latent heat of freezing at the equilibrium surface temperature is defined by

$$q_f = R_w l_{fm} n \quad (4.27)$$

where  $n$  is the fraction of the accreted mass which freezes;  $l_{fm}$  is the specific latent heat of freezing at  $t_m$ .

v) Aerodynamic heating due to adiabatic compression of the air and viscous work in the boundary layer may be expressed as follows:

$$q_k = \frac{1}{2} \frac{hr_c v^2}{c_p} \quad (4.28)$$

where  $r_c$  is called the recovery factor and is based on Seban (1960), as follows

$$r_c = 0.75 + 0.25 \cos 2\theta \quad (4.29)$$

vi) Heat loss by conduction

$$q = k_i(t_s - t_a) \quad (4.30)$$

where the  $t_s$  is the temperature of the cylinder;  $k_i$  is thermal conductivity of ice. The term for heat loss by radiation is disregarded by Lozowski et al. (1979).

#### 4.5 Application of Model to Different Conditions

The model can be applied to two different conditions, namely, to a supercooled liquid aerosol flow and to a mixed aerosol flow containing liquid water and ice particles. In each case, the model may be applied with runback or non- runback water. The subsection below describes the model under conditions with a liquid aerosol flow, where the presence of runback water will change the original equation.

## Runback Water Conditions

In order to bring about water runback on a thermodynamic surface such as a stationary icing cylinder, the model assumes that all of the unfrozen water in any sector flows into the next downstream sector. "The runback water participates in the heat exchange at this location by adjusting to the new equilibrium surface temperature of the sector, and it is frozen in the same proportion as the directly impinging water. Since a steady state is assumed, the runback velocity is not required. If  $R_w^*(\theta_i)$  represents the runback mass flux into sector  $i$  centred on angle  $\theta_i$ , while  $R_w$  represents the directly impinging mass flux, then the heat balance equation becomes:

$$H(t_a - t_s) + H\left(\frac{Pr}{Sc}\right)^{0.63} \frac{\epsilon l_v}{\rho C_p} (e_a(t_a) - e_s(t_s)) + R_w \bar{c}_w (t_a - t_s) + nR_w l_f(t_s) + \frac{1}{2} \frac{Hr_c \mu^2}{C_p} + \frac{1}{2} R_w \mu^2 + R_w^* \bar{c}_w (t_s^* - t_s) + nR_w^* l_f(t_s) = 0 \quad (4.31)$$

The last two terms represent the heat of cooling and freezing of the runback water, respectively. The incoming temperature  $t_s^*$  of the runback water is assumed to be the equilibrium surface temperature of the sector immediately upstream, which is :

$$t_s^*(\theta_i) = t_s(\theta_{i-1}) \quad (4.32)$$

also, since

$$R_w^*(\theta_i) = (1 - n)R_w(\theta_{i-1}) + R_w^*(\theta_{i-1}) \quad (4.33)$$

for the first sector, because there is no sector upstream,  $R^*(\theta_1) = 0$ , and since the runback from sector 1 is split, half proceeding to the upper cylinder surface and half to the lower surface, the equation must be modified for the second sector only so that

$$R_w^*(\theta_2) = (1 - n) + R_w(\theta_1) \quad (4.34)$$

and, it is assumed that the runback from the final sector is shed into the air stream”[Ref: 19].

#### **4.6 General Structure of Makkonen Model (1984)- based of the work of Makkonen (Ref: 22)**

Makkonen (1984) presented a time-dependent numerical model of icing on wires which considers the icing wire mainly as a growing, slowly rotating, circular cylinder. This idea is based on the observation that ice deposits on transmission line cables are often nearly cylindrical, and furthermore, the results indicate that the icing rate is not very sensitive to small deviations from the cylindrical shape.

##### **4.6.1. Model Input and Output**

The input items of the model are the same as those for the Lozowski et al. (1979) model, namely: air pressure; air velocity; air temperature; LWC in the air flow; and, the duration of the experiment. The output items of the model are: icing intensity,  $I$ , which is

defined as the rate of increase in the mass of ice divided by the portion of the surface area of the windward ice deposit. On a circular cylinder the icing intensity is:

$$I = \frac{2}{\pi} EnVw \quad (4.35)$$

where  $E$  is the collection efficiency,  $n$  is the freezing fraction,  $V$  is the wind speed and  $w$  is the LWC in the air. The quantities  $I$ ,  $E$  and  $n$  are the overall values for the part of the object surface that faces the wind.

Ice growth is considered wet when  $n < 1$ , which means that there is some run-off from the ice deposit as a whole. This run-off is assumed to shed into the wind at the edges of the cylinder. In dry growth  $n = 1$  and there is no run-off from the deposit, although the local freezing fraction may be less than unity near the stagnation line. Ice load,  $M_i$ , and ice diameter,  $D_i$ , are also further output items of the model and are discussed further on in the text.

#### 4.6.2. Collection Efficiency of the Makkonen Model- 1984

As in the Lozowski et al. (1979) model, the calculation of collection efficiency is based on the numerical solution provided by Langmuir and Blodgett (1946) for the dimensionless equation for the motion of a droplet in the airflow. The calculation will lead to the collection efficiency,  $E_m$ , based on the median volume droplet diameter (MVD),  $d_m$ , of the droplet size distribution (DSD). The equation for the motion of a droplet in the airflow is:

$$K \frac{dv_d}{d\tau} = \frac{c_d \text{Re}_\tau}{24} (\overrightarrow{V_a - V_d}) \quad (4.36)$$

where  $\tau$  is the time,  $K = \frac{\rho_w v d^2}{9\mu D}$  is the inertia parameter, and  $C_d$  the droplet drag coefficient while the Reynolds number is

$$\text{Re}_\tau = p_a d \left| \overline{V_a - \vec{V}_d} \right| / \mu \quad (4.37)$$

“The droplet Reynolds number is based on the droplet relative velocity, where  $\vec{V}_a = V_a / V$  is the dimensionless droplet velocity. The variable  $d$  is the droplet diameter,  $\rho_w$  is the water density,  $\mu$  is the absolute viscosity of air,  $D$  is the cylinder diameter, and  $P_a$  the air density. The air velocity vector,  $V_a$ , is obtained from the equation for the potential flow around a cylinder, and the drag coefficient,  $C_a$ , as a function of  $Re_\tau$  is found from the experimental data recorded by Langmuir and Blodgett (1946). The solution of the motion equation of a droplet may then be used to calculate the droplet trajectories from which the total collection efficiency,  $E_m$ , is obtained. The results of this calculation are provided by Langmuir and Blodgett (1946). Makkonen made the following matches to the numerical data used in the model:

$$E_m = 0.5 [\log(8K_0)]^{1.6} \quad K_0 \leq 0.8 \quad (4.38)$$

$$E_m = K_0^{1.1} (K_0^{1.1} + 1.426)^{-1} \quad K_0 > 0.8 \quad (4.39)$$

where

$$K_0 = K \left[ 0.087 \text{Re}_d (0.76 \text{Re}_d^{-0.027} + 1) \right]^{-1} \quad (4.40)$$

and

$$K = \frac{\rho_w v d^2}{9\mu D} \quad (4.41)$$

Equation (4.41) was obtained by Cansdale and McNaughtan (1977). Here,  $K$  is the inertia parameter, and  $Re_d$  is the Reynolds droplet number based on the free stream velocity

$$Re_d = \frac{\rho_a \cdot d \cdot u}{\mu} \quad (4.42)$$

For the droplet impact speed,  $V_0$ , at the stagnation line, Makkonen (1984) used the following formulas

$$V_0 = V(-0.174 + 1.464K_0 - 0.816K_0^2) \quad \text{for } K_0 \leq 0.55 \quad (4.43)$$

$$V_0 = V(0.561 + 0.592 \log K_0 - 0.26(\log K_0)^2) \quad \text{for } K_0 > 0.55 \quad (4.44)$$

where  $K_0$  is determined from equation (4.40). The calculation of  $E_m$ , as explained above, is made by using the median volume diameter,  $d_m$ , of the droplets. Makkonen (1984) mentions that in natural conditions, however, the icing cloud is not mono-disperse, but has a certain DSD. This means that the real collection efficiency,  $E$ , should be calculated separately for each size category, and the total value of  $E$  is then the sum of these collection efficiencies for specific droplet size multiplied by the fraction of the liquid

water content represented by that droplet size. The collection efficiency , $E$ , is calculated by using the empirical equation”[Ref: 22]

$$E = 0.69E_m^{0.67} + 0.31E_m^{1.67} \quad (4.45)$$

### 4.6.3. Freezing Fraction

As in the model designed by Lozowski at al. (1979), the freezing fraction can be calculated from the heat balance of the icing surface, which in this case is the front half of the cylindrical ice deposit.

$$n = \frac{\pi H}{2EVwl_f} \left[ -t_a + \frac{Kl_e}{C_p \rho_a} (e_0 - e_a) \right] - \frac{rV^2}{2c_p} - \frac{t_a}{l_f} (C_w + \frac{\pi\sigma_a}{2EVw}) \quad (4.46)$$

In equation (4.46), the overall heat transfer coefficient  $H$  is written in terms of the Nusselt number  $Nu$  as follows:

$$H = k_a \frac{Nu}{D} \quad (4.47)$$

where  $k_a$  is the thermal conductivity of air. Makkonen used of the following parameterisation for the model:

$$Nu = 0.32 Re^{0.85} \quad (4.48)$$

where  $R_e = \frac{\rho_a D v}{\mu_a}$  is the cylinder Reynolds number. Equation (4.48) is a linear fit for the front half of his roughest test cylinder in the range of  $7 \times 10^6 < Re < 9 \times 10^5$  based on the data provided by Achenbach (1977).

#### 4.6.4. Heat Balance Equation

The heat balance equation for the icing surface of Makkonen's model is

$$q_f + q_v + q_k + q_a = q_c + q_e + q_l + q_s + q_i \quad (4.49)$$

where:  $q_f$  is the latent heat released during freezing;  $q_v$  is frictional heating of air;  $q_k$  is kinetic energy of the impinging water;  $q_a$  is heat released in cooling the ice from its freezing temperature ( $0^\circ\text{C}$ ) to the surface temperature  $t_s$ ;  $q_c$  is loss of sensible heat to air;  $q_e$  is heat loss due to evaporation (wet growth) or sublimation (dry growth);  $q_l$  is heat loss in warming the impinging water to  $0^\circ\text{C}$ ;  $q_s$  is heat loss due to long wave radiation; and,  $q_i$  is heat loss into the ice due to conduction. In comparison with the Lozowski et al. (1979) model, the Makkonen (1984) model applies heat loss due to the effects of radiation. The remaining parameters are the same as those applied by Lozowski et al. (1979).

#### 4.6.4. Time Dependence in the Makkonen Model

Time dependence is the main aspect of the Makkonen model, and is due to observation of changes in the diameter of the icing object during the ice accretion

process. This means that the collection efficiency,  $E$ , and the freezing factor,  $n$ , depend on time  $\tau$ . When the atmospheric conditions are kept unchanged, the ice load per unit length of the wire,  $M_i$ , at time,  $\tau_i$  is:

$$M_i = \int_0^{\tau_i} I(\tau) \frac{\pi}{2} D(\tau) d\tau = V_w \int_0^{\tau_i} E(\tau) n(\tau) D(\tau) d\tau \quad (4.50)$$

“The process of the calculation of the model is carried out in a step-wise manner. For each time-step,  $i$ , the collection efficiency,  $E_i$ , and freezing fraction,  $n_i$ , are determined. The icing intensity,  $I_i$ , is obtained from equation (4.35), and the ice load,  $M_i$ , where the sub-index,  $i$ , refers to the time-step, is defined as follows:

$$M_i = M_{i-1} + I_{i-1} \frac{\pi}{2} D_{i-1} \Delta \tau \quad (4.51)$$

The ice deposit diameter,  $D_i$ , corresponding to the ice load,  $M_i$ , is calculated from

$$D_i = \left( \frac{4(M_i - M_{i-1})}{\pi \rho_i} + D_{i-1}^2 \right)^{1/2} \quad (4.52)$$

Equation (4.52) means that the cross-sectional shape of the ice deposit is assumed to be cylindrical”[Ref: 22].

#### 4.6.5. Ice Density

“Because of the time-dependent nature of the Makkonen model (1984), it is necessary that, using the density, the ice growth at the object diameter be related to the ice mass. For this purpose Makkonen (1984) used the density parameter from the Macklin (1962) model:

$$X = -(V_0 d_m / 2t_s) \quad (4.53)$$

where  $X$  is the density parameter,  $d_m$  is the MVD diameter of the DSD ( $\mu\text{m}$ ),  $V_0$  is the impact speed of the droplets at the stagnation line ( $\text{ms}^{-1}$ ), based on Langmuir and Blodgett (1946); and  $t_s$  is the mean surface temperature of the ice deposit ( $^{\circ}\text{C}$ ). Based on Macklin’s laboratory experiments and on the measurements in natural icing conditions taken by Bain and Gayet (1983), Makkonen derived the following relations for ice density:

$$\rho_i = 0.1 \quad X \leq 0.9 \quad (4.54)$$

$$\rho_i = 0.11X^{0.76} \quad 0.9 \leq X \leq 10 \quad (4.55)$$

$$\rho_i = X(X + 5.6) - 1 \quad 10 < X \leq 60 \quad (4.56)$$

$$\rho_i = 0.92 \quad X > 60 \quad (4.57)$$

The droplet impact speed,  $V_0$ , is calculated from the equations (4.43) and (4.44) based on the study made by Langmuir and Blodgett (1946). The mean surface temperature,  $t_s$ , is solved numerically from the heat balance equation of the dry growth process ( $n=1$ )

$$\pi EV_w (l_f + C_w t_a - C_i t_s) = H[t_s - t_a] + \frac{Kl_e}{C_p \rho_a} (e_0 - e_a) - \frac{rV^2}{2c_p} - \sigma_a (t_s - t_a) \quad (4.64)$$

Finally, the total ice density,  $\rho_i$ , for the time step,  $i$ , is determined by

$$\rho_i = 4M_i (\pi D_i^2 - \pi D_0^2)^{-1} \quad (4.65)$$

where  $D_0$  is the initial wire diameter”[Ref: 22].

## CHAPTER 5

# COMPARISON OF EXPERIMENTAL RESULTS WITH MODE PREDICTIONS: VERIFICATION OF WATER RUN-BACK ICING MODEL

### 5.1 Selecting a Basis for Comparison

#### 5.1.1 Icing Intensity and Ice Load

The basis chosen as most suitable for comparing the results from modelling the ice accretion process, as obtained both experimentally and theoretically, was the ice load accreted on the surface of a non-rotating horizontal cylinder in an icing wind tunnel over 60 minutes of exposure to a flowing supercooled aerosol cloud,  $M$ . This amount of ice accretion will be termed an *experimental unit* from now on in this study and will be measured in  $\text{g} \cdot \text{hour}^{-1}$ , while the corresponding 60-minute exposure time-interval will be termed the *duration of the experimental unit* and will be measured in hours. As Lozowski et al. (1979) so aptly observed, the model predictions pertain only to a short time (a few minutes) interval at the outset of the icing process, while the experimental results refer to the entire duration of the experimental unit. In order to draw a comparison between the results of both theoretical and experimental modelling, either the icing rate should be integrated over the duration of the experimental unit, or the ice mass accreted during this time-interval should be used for its differentiation over small time steps, in order to obtain the corresponding mean icing rates during each time step. The type of

experimental construction used in this icing wind tunnel dictated the choice of ice mass for comparison rather than icing intensity. The mass may be measured conveniently after the experiment is concluded; while the intensity, which is, in fact, the actual output of the mathematical model, should be permanently monitored over the entire duration of each experiment. The experimental structure, represented by aluminium cylinders (88.5cm length) of different diameters, was placed horizontally across the test section and inserted into two bearings mounted rigidly on each facing wall of the test section. This type of construction does not, however, allow for monitoring the ice load accretion process, as was possible in the experiments carried out by Personne and Gayet (1988). In their investigation, the experimental icing cylinder, which modeled the OHTL cable, was mounted on a spring which had been specially designed to take into account the stiffness of a natural cable rotating under the weight of ice accreted on the side exposed to the wind. Although the lack of an opportunity to monitor the ice mass accretion process over the duration of each experiment using a non-rotating cylinder may be a possible drawback of this type of construction, it is offset to some degree by the considerable advantage of being able to carry out experiments while also using a rotating cylinder with the same experimental construction (See *Chapter 6*). The duration of the experimental unit was set at 60 minutes in order to obtain a noticeable difference in ice mass (if any), when the cylinders of different diameters are exposed to an aerosol cloud under the same thermodynamical and aerodynamic conditions.

### 5.1.2 Spatial Integration Procedure

A brief explanation is required for the conversion of icing intensity, as yielded by the icing model, into the mass of ice accreted over the duration of the experimental unit in the icing wind tunnel. One of the main outputs of the model (Lozowski et al., 1979) is the icing intensity,  $R$ , which is measured in  $\text{kg}\cdot\text{s}^{-1}\cdot\text{m}^{-2}$  and defined for 18 equal control volumes on the windward part of the top half of the cylinder surface. The control volumes are obtained by dividing the  $90^\circ$  arc, representing this quarter-cylinder, into angular sectors of  $5^\circ$  each. To obtain the theoretically modeled ice accretion mass during a one second time-interval, this icing intensity should be spatially integrated over the area of the accretion surface in two directions: along the cylinder length and along the  $90^\circ$  arc representing the windward top quarter of the cylinder. Integration over the lateral spatial coordinate along the cylinder is carried out using a 2-inch interval, as was used during calibration of the liquid water content (LWC) and droplet size distribution (DSD) in this icing wind tunnel (Karev et al., 2002). It should be noted that the spatial distribution of LWC in the cross-section of the icing wind tunnel was measured with a 2x2-inch grid during the above-mentioned experimental series. The spatial field of the LWC, as obtained by measuring the circumference of the ice accretion on non-rotating pipes (Ide, 1990), particularly for low air speeds, was found to be strictly non-uniform (see *Section 5.2.4*). Integration over the angular coordinate was carried out by using a spatial interval equal to the length of the angular sectors of  $5^\circ$  each. In order to take into account the non-uniformity of the LWC recorded earlier, the model was applied to 17 consecutive  $90^\circ$  arcs obtained at distances of every 2 inches along the cylinder. Since the water film flow is presented only implicitly in the model and does not take into account the dynamics of its

flow, the axial symmetry with respect to the stagnation line on the cylinder was automatically pre-assumed in the ice accretion shape. Such a simplification, which depends on the free stream air velocity, may be counted as reasonable for high air speeds and/or low LWC, but it is not appropriate for low air speeds and/or high LWC, as applied in certain of the experiments in this series. The reasoning and conditions for this simplification will be the theme of further discussion later on in the text. By taking into account the proposed axial symmetry of the ice accretion shape with respect to the stagnation line, the mass of the ice accreted on the windward side of the cylinder in one second may be found by the simple procedure of doubling the ice accretion mass as obtained for the top part of the windward side of the cylinder only. Generally speaking, on the lee side of the cylinder, the mathematically modeled ice accretion is formed by the run-back water flux only (if any), defined from the last bin on the windward side of the cylinder. In nature, however, particularly for low air speed conditions ( up to  $5 \text{ m s}^{-1}$ ), or under conditions of a high rate of unfrozen water on the icing surface, only a few frozen rivulets may be observed on the lee side of the cylinder, forming icing rings around it. A two-dimensional representation of the ice accretion in a mathematical model cannot take into account those features of freezing as produced by the natural division of water film flow into separate rivulets. Also, a two-dimensional representation together with a pre-assumed leeward direction of water film flow virtually preclude incorporating a sub-model of icicle growth into the same ice accretion model. The problems arising from such a limitation will be more carefully investigated later on in the concluding section.

### 5.1.3 Time Integration Procedure

A factor that further complicates the issue is the time independence of the model. Over the duration of the experimental unit, the true diameter of the icing structure increases progressively, while the shape of the ice accretion changes radically. These transformations produce irreversible changes in the dynamic and thermodynamic parameters responsible for the local collection rate (collection efficiency) of supercooled water droplets on the icing surface, as well as for the rate of transfer to the environment of heat released through the conversion of water into ice (heat transfer coefficient). When extrapolating the model-predicted rate of icing intensity in time, these effects, as reported by Lozowski et al. (1979) cannot be taken into account. One of the relatively simplified solutions to this problem was proposed in a study carried out by Brown and Horjen (1989) where the concept of an *effective cylinder diameter* was introduced. After each time step, once the new local ice accretion thickness on the cylinder becomes known, a new diameter for the ice-covered cylinder is re-calculated by integrating accreted ice mass over all windward angular positions and subsequently averaging it over the same windward surface. This procedure takes into account the changing cylinder diameter, but does not consider the modified ice accretion shape, which may bring about profound changes in the character of the heat transfer. This study and subsequent ones will attempt to consider several different types of extrapolation and interpolation in time, and will distinguish between the advantages and drawbacks of each:

- i) Simple extrapolation in time for constant cylinder diameter;
- ii) Extrapolation in time with an effective cylinder diameter;

- iii) linear interpolation applied for initial diameter of bare cylinder and final diameter of an ice-covered cylinder as extracted from digital photos.

#### **5.1.4 Influence of Ice Sample Density and Sponginess**

Lozowski et al. (1979, p.47) listed some of the problems arising from uncertainty in the density of the growing ice layer,  $\rho_i$ , which were encountered while converting model-predicted icing intensity into ice load. The goal of this study, which was to verify the level of predictability of glaze ice formation by means of two atmospheric icing models, dictated that the experimentally obtained ice accretion patterns should have the ice density typical of glaze ice formation, or  $\rho_{i,gl} = 918 \text{ Kg m}^{-3}$ . Thus, the thermodynamic parameters were selected with great care (see sub-sections 5.2.1 thru 5.2.3 and section 5.3), in order to obtain ice accretion of such a density, or as close to it as possible. Due to the non-uniformity of LWC and DSD fields, as observed during calibration of the icing wind tunnel (Karev et al., 2002), however, there existed a slight probability that, during experimental ice accretion, lateral changes of ice density along the horizontal cylinder might occur. The potential for this occurrence would be when the conditions in the icing wind tunnel, over the duration of the experiment, were fairly close to those characterizing the boundary between the two different icing regimes. These regimes, which are termed in the literature “wet” and “dry”, produce distinctive ice patterns, called glaze ice and rime ice, respectively. Close to this boundary, a minimal change in the LWC or DSD fields along the cylinder can cause a shift across the boundary line from one distinct regime into another, each with its typical pattern of ice accretion. To ensure that this does not occur during any of the experiments, the supplementary measurements of local ice

density were added to the procedure of final ice mass weighing. These measurements were similar to those designed by Karev et al. (2002) to evaluate the influence of the non-uniformity of the LWC and DSD fields in the test section of an icing wind tunnel on the final results of experimental modelling. At the conclusion of each experiment, the ice accretion on the cylinder was weighed, and several digital color prints were then made of the ice accretion as a whole, while certain of its distinctive segments were also recorded. Finally, ice accretion patterns were collected from three locations along the stagnation line of the cylinder: the mid-point; 8 inches left; and 8 inches right of the centre of the cross-section. The patterns of ice accretion were collected exclusively from the stagnation line or, in some special cases, within a range of 30 degrees above and below it, in order to avoid the potentially misleading data produced by ice density dependence on the angle formed by the stagnation line and the site of sample extraction (Bain and Gayet, 1983). The density of the ice accretion patterns, as collected from different locations in the cross-section, was then tested by using the displacement method. The method consists of weighing the ice accretions first in air and then in oil of a known density. The density of the ice accretion pattern may be calculated by evaluating the Archimedes force from the second weighing. The original method was improved on, here, by calculating the density of the ice accretion including interstitial air. Any potential changes of density were attributed to local changes of the LWC and DSD fields, when all other parameters were maintained constant throughout the duration of each experimental unit. For the theoretical evaluation of the results obtained, the classical water run-back icing model (Lozowski,1979) was modified by introducing into it the dependence of ice density,  $\rho_i$  ( $\text{kg m}^{-3}$ ), on the Macklin parameter,  $X$ , (Macklin,1962). This dependence was used in its

modified form, taking into account an additional dependence on the Stokes number,  $K$ , as proposed by Castellano et al. (2000). Comparison of ice accretion densities from some of the experimental units, as obtained by experimental and theoretical modelling, are presented in *Figure 5.1*. It may be seen from this figure that, in almost all of the experiments, the ice samples collected had an icing density which was marginally lower than that of typical of glaze ice,  $\rho_{i,gl}=918 \text{ kg m}^{-3}$ , a fact which maybe attributed to the

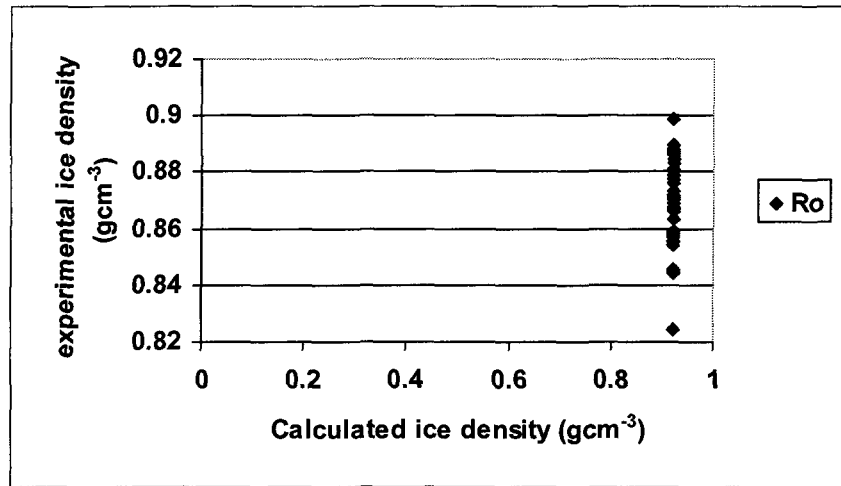


**Fig.5.1** Ice density as obtained in the experiments

level of accuracy of the experimental displacement method. The ice accretion patterns observed were generally transparent, typical of glaze ice. Accepting the assumption that the ice accretion type occurring everywhere along the cylinder is glaze ice, it is automatically accepted also that the icing intensity obtained from the model,  $R$ , and measured in  $\text{kg s}^{-1} \text{m}^{-2} (\text{S}^\circ)^{-1}$ , represents a radial growth of ice on the cylinder,  $h$  ( $\text{m s}^{-1} (\text{S}^\circ)^{-1}$ ). The latter growth, for the time interval  $\Delta t$ , may be obtained from the following expression (*c.f.* Lozowski, 1979):

$$h = \frac{2R \cdot \Delta t / \rho_i}{1 + \sqrt{1 + \frac{4R}{\rho_i \cdot D_c}}} \quad (5.1)$$

where  $D_c$  (m) is the diameter of the experimental cylinder. If the assumption  $\rho_i = \rho_{i,gl} = 918 \text{ Kg m}^{-3}$  is not correct, then the assumed ice growth direction is not correct either, since in this case, the ice has a tendency to grow counter-streamwise to the air flow (see reasoning provided by Lozowski et al., 1979, p.48). This fact should obviously influence the theoretically obtained results of atmospheric icing.

The sponginess of experimentally obtained ice patterns from the three locations along the stagnation line of the cylinder, as mentioned earlier, is more complicated to investigate than density. In fact, from the very beginning, this parameter was not included as a feature of the investigation. It should be noted that the unjustified exclusion of the role of sponginess was due to a lack of the appropriate experimental equipment available at CAIRWT at the time when this study was planned. In the above-mentioned study, carried out by Lozowski et al. (1979), the authors were able to make some of the experimental results obtained in the wind icing tunnel, particularly at low air speeds, coincide with the theoretical predictions only by means of incorporating 25-45 % of the sponginess factor of the accreted ice sample. A portable calorimeter for field measurements of ice sponginess was designed and built by Lozowski and Blackmore (described in a personal communication, 2002), introducing a new concept for the use of the calorimetric approach proposed in earlier studies of hailstones (Gitlin et al., 1968; Lessins et al., 1980). Sponginess of the growing ice layer was, therefore, not considered

in this study, although it has proved to be one of the significant factors influencing the final results of modelling.

## **5.2 Selecting Experimental Conditions**

### **5.2.1 Air Speed**

Air velocities as observed in nature, which are typical of an atmospheric icing phenomenon leading to glaze ice formation, lie in a range from ultra-low to medium speeds. Therefore, three values of air speed covering this range were chosen initially for the study:  $2 \text{ m}\cdot\text{s}^{-1}$ ;  $5 \text{ m}\cdot\text{s}^{-1}$ ; and  $10 \text{ m}\cdot\text{s}^{-1}$ . During the dynamic calibration of the CIGELE Atmospheric Icing Research Wind Tunnel (CAIRWT), however, it was found that, at air speeds of  $2 \text{ m}\cdot\text{s}^{-1}$ , the influence of gravity on the spatial uniformity of the LWC and DSD fields in the test section was significant, possibly influencing the final results of the experimental modelling of atmospheric icing phenomena. Thus, bearing this critical fact in mind, the choice was limited to only two air speeds:  $5 \text{ m}\cdot\text{s}^{-1}$  and  $10 \text{ m}\cdot\text{s}^{-1}$ . The relationship between the frequency of the AC engine in the CAIRT and the air velocity was obtained during the same dynamic calibration series. Throughout the duration of every experiment, the need for the simultaneous monitoring of air velocity was rendered unnecessary by using the relationship thus obtained.

### **5.2.2 Air Temperature**

Two ambient temperature values were selected for this study:  $-5 \text{ }^\circ\text{C}$  and  $-10 \text{ }^\circ\text{C}$ , as representative of warm and cold icing conditions, respectively. This terminology will be preserved further on in the text for the discussion of the experimental results.

Throughout the duration of the experiments, the ambient temperature in the icing wind tunnel was permanently monitored by three T-type thermocouples mounted in the ceiling of the tunnel at various locations in the test section: its inlet, mid-point, and outlet. This set-up made it possible to maintain permanent monitoring of the streamwise temperature gradient in the test section, the influence of which was expected to manifest clearly at low and ultra-low air speeds. This parameter, however, was taken as negligible by the end of this study. All temperature data were collected using a standard data acquisition system (InstruNet, United Electronics, USA).

### **5.2.3 Air Pressure and Air Humidity**

It is assumed that all data pertaining to the experimental units were collected under conditions of constant static pressure, which is equal to the pressure of 1 NACA Standard Atmosphere at sea level ( $p_{st}=101325 Pa$ ). The relative humidity,  $\Phi_a$ , tended to oscillate within the range from 0.81 to 0.92. The reason for this lies in the fact that the icing wind tunnel was always well cooled before the beginning of each experiment, and the water supply to the nozzles was maintained constant for each specific droplet size distribution (DSD). On the basis of comparison of the recorded results from monitoring relative humidity over the duration of several experimental units, it was decided, for the first approximation, to omit the relative air humidity at the mid-line of the test section from the calculation. This does not imply, however, that air humidity is not an important thermodynamic factor for the further verification of the models. It only means that, under the conditions considered in this experimental study, the influence of this factor is of the same order of magnitude as the experimental error arising during final ice load

measurements. Thus, the parameter was dropped from further consideration in this instance.

### **5.3 Liquid water Content and Water Droplet Size Distribution**

Since both liquid water content (LWC) and droplet size distribution (DSD) were found to be dependent on the thermodynamic and dynamic parameters of air flow presented earlier, and because they are of crucial importance to the final results of experimental modelling, information concerning them will be discussed in a separate section.

#### **5.3.1. Water Supply Rate: Liquid Water Content (LWC) or Precipitation Rate**

Glaze ice typically forms on structures under freezing rain conditions when relatively large water droplets with diameters of an order of magnitude  $O(mm)$ , reach the freezing surface, having been, in the meantime, well-cooled to about water fusion temperature. These conditions, however, are difficult to model experimentally in a horizontal closed-loop icing wind tunnel, due to the adverse influence of the sedimentation process of large droplets combined with insufficient cooling from the initial room temperature to their final temperature over the time period of active droplet residence in the test section (Karev and Farzaneh, 2002). This time interval, obtained by dividing the distance covered by a moving droplet (on its path between spray-bar and centre of test section) by the air speed, should be chosen to ensure a maximum of cooling and a minimum of sedimentation. The cooling is a function of droplet diameter and air velocity, among other factors. As a result, the spectra of large droplets may have different

temperatures for different air speeds upon their impingement on the icing surface, once they have been dispersed in an icing wind tunnel for modelling DSD during freezing rain phenomena. Moreover, various droplet spectra may also have distinct temperatures even for the same air speed. This may happen as a result of the cooling process in such spectra which continues beyond the instant of contact with the icing surface. This fact will undoubtedly have an influence on the final outcome of the experimental modelling of atmospheric icing and, in particular, on the spacing of icicles. Makkonnen and Fujii (1993) reported not being able to record temperatures for water droplets impinging on the icing surface during their experiments. The droplet temperature problem mentioned does not exist for the medium-sized droplets which characterize the cloud droplet range, and which have a diameter of an order of magnitude of several tens of microns,  $O(\sim 10 \mu m)$ . This is the result of a relatively weak sedimentation process and the fairly rapid cooling of droplets of this size range, as dictated mainly by air relative humidity and air temperature. Based on the above information, it was decided to carry out the experiments by using nozzles to produce cloud droplets,  $O(\sim 10 \mu m)$ , and then to find the relationship between the water supply characteristics in both the cases mentioned: LWC, (in  $g \cdot m^{-3}$ ), for cloud droplets; and precipitation rate, H, (in mm/h), for rain phenomena.

### **5.3.2. Relationship between LWC and Air Velocity**

During the LWC calibration of the CIGELE Atmospheric Icing Research Wind Tunnel (CAIRWT) (Karev et al., 2002), it was revealed that the LWC in the test section is directly proportional to the air velocity for the low air speed range considered during calibration (from 5 to 15  $m \cdot s^{-1}$ ). Since the range of air speed used in this experimental

series ( $5 \text{ m s}^{-1}$  to  $10 \text{ m s}^{-1}$ ) lies inside the range considered during calibration, these results will be applied here. The dependence of the LWC on the dynamic parameters of the nozzle system and the tunnel may be expressed in the following way:

$$w = f(V_a, \partial P, Q_w)$$

(5.3)

where  $w(\text{kgm}^{-3})$  is the LWC,  $V_a (\text{m s}^{-1})$  is the air speed;  $dP = P_w - P_a (\text{N m}^{-2})$  is the differential pressure between the pressure in the water and air lines of the nozzle system;

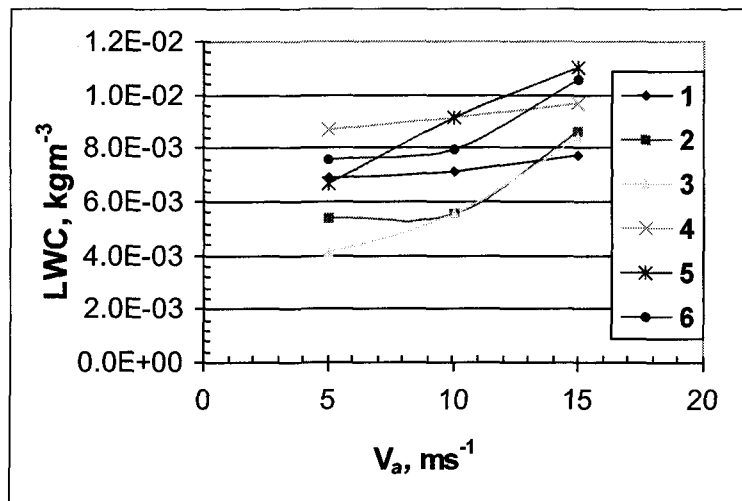


**Fig. 5.2.** Experimental relationship between LWC ( $\text{kgm}^{-3}$ ), and air speed,  $V_a (\text{m s}^{-1})$ , for various pressures in the air line,  $P_a$ , and differential pressure,  $dP$ ,: 1, 2, and 3,  $P_a=25 \text{ psi}$  and  $dP$  is equal to 3 psig, 24 psig, and 55 psig, respectively; 4, 5, and 6,  $P_a=40 \text{ psi}$  and  $dP$  is equal to 9 psig, 19-24 psig, and 40 psig, respectively(Karev, Farzaneh and Mousavi, 2002).

and  $Q_w$  is the water flow rate in it. Figure 5.2 shows the experimentally obtained relationships between the LWC and air speed for different combinations of the dynamic parameters of the nozzle system as obtained in the above-mentioned calibration series.

The LWC was measured at the mid-point by using standard techniques for measuring LWC in an icing wind tunnel described by Stallabrass (1978). It will be observed from this figure that the LWC inside the tunnel is directly proportional to the air speed. The difference between these results and the results obtained for high and ultra-high air speeds in the LEWICE Icing Research Wind Tunnel (Ide, 1990), where the LWC was found to be inversely proportional to air speed, may be explained by the changing role of air velocity within various air speed ranges. The existence of a relationship between LWC and air speed implies that the LWC will not be the same for different air speeds when other parameters remain constant. Since DSD was also found to be dependent on air speed, air temperature and air humidity, the best way to work with thermodynamic and dynamic parameters is to divide them into two different sets each one composed of either independent or dependent parameters. The former set would unite those thermodynamic parameters which remain constant with the change of other parameters; air temperature and air speed belong to this group. The LWC and DSD would be united in the latter set, because they tend to change when other parameters inside the tunnel are modified. When the selection of the thermodynamic and dynamic parameters is made and choice of the values for independent parameters for experimental verification is decided upon (see *Section 5.2*), then the selection of the dependent parameters is limited by the experimental relationships presented in *Figure 5.2*. This part of the investigation is devoted to verifying the two icing models for specific values of independent thermodynamic and dynamic parameters in the tunnel, i.e. air temperature and air speed. Further investigation, at a later date, will evaluate the models for constant dependent thermodynamic parameters in the tunnel, i.e. the LWC and DSD, which require the

variation in independent parameters. Since the main axis of this investigation is glaze ice accretion, all experiments were carried out under maximum flow rate performance as were all experiments during the calibration series (Karev et al., 2002). Two combinations of nozzle pressure parameters used during the same calibration series were applied in this

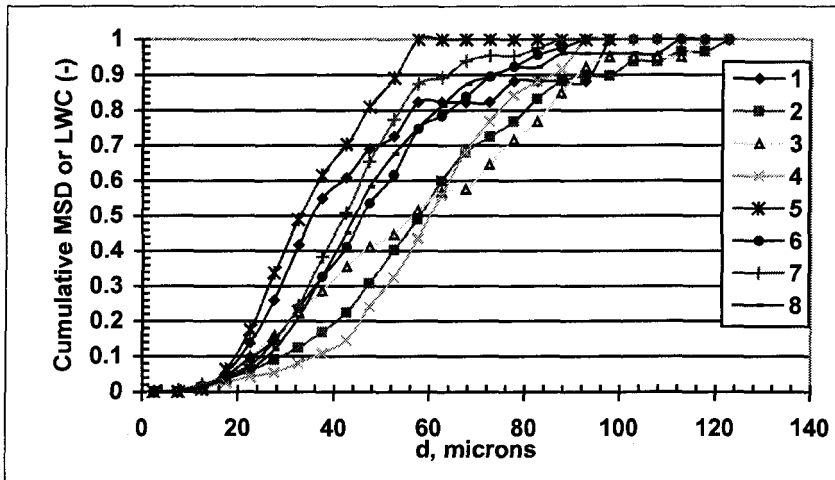


**Fig.5.3.** Two cumulative mass-based droplet size distributions (MSD) used for investigation of LWC/DSD uniformity: 1-4 A-type distribution; 5-8 B-type distribution; 1, and 5, near spray bar; 3, and 7, mid-point of cross-section; 2, and 6, lateral patterns 8 inches left of centre; 4, and 8, lateral patterns 8 inches right of centre. Ambient temperature  $t_a=5^\circ\text{C}$ ; relative humidity in the range of  $0.73 < \Phi_a < 0.85$ ; air speed  $V_a=5\text{ms}^{-1}$  (Karev et al., 2002).

investigation so as to obtain two distinct DSD's, called A-type and B-type, below. The first was obtained by a combination of  $P_w=53$  psi and  $P_a=25$  psi, and the second, by a combination of  $P_w=53$  psi and  $P_a=40$  psi. The A-type DSD, as used during CAIRT LWC calibration, had a median volume droplet diameter (MVD) of about  $57\ \mu\text{m}$ , and the B-type DSD had a MVD of about  $42\ \mu\text{m}$ . This may be seen from the cumulative mass size distribution (MSD) presented in Figure 5.3. A-type DSD, at different stages of its development in the wind tunnel, is presented in Figure 5.4. The two selected DSD's are

sufficiently different to produce an obvious ice mass difference for single thermodynamic condition on the same icing cylinder.

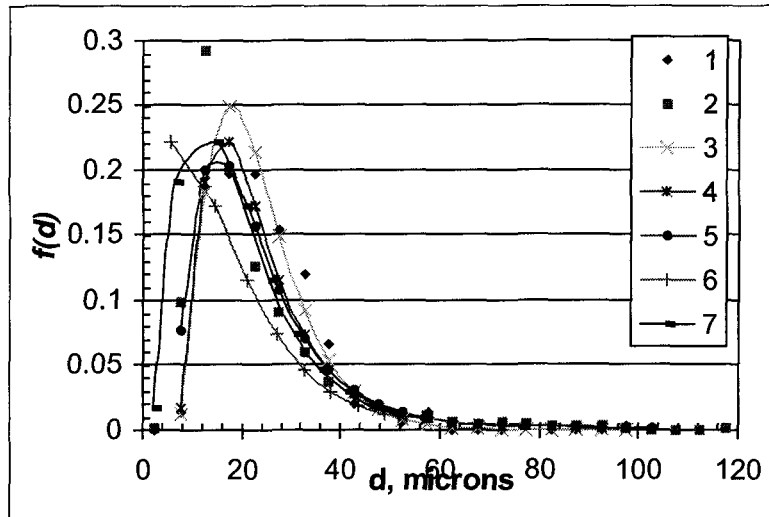


**Fig.5.4.** Comparison of experimentally recorded droplet size distribution: 1-close to spray-bar and 2- middle of test section; 3- and 4- best matches of distribution under 1; 5- best match of distribution under 2; 6- forecast of 5 using 4, where  $\Phi_a=0.7$ ; 7- forecast of 5 using 4, where  $\Phi_a=0.9$  (Karev and Farzaneh, 2002).

### 5.3.3. Non-Uniformity of LWC and DSD in the Test Section and Lengthwise on the Experimental Cylinders

During the LWC calibration of the CAIRT (Karev and Farzaneh, 2002), it was found that the spatial field of the LWC is strictly non-uniform, when obtained by measuring the circumference of the ice accretion on non-rotating pipes (Ide, 1990), particularly for low air speeds. This produced certain difficulties in calculating the ice accretion load from the icing intensity as yielded by model application. In order to compare the experimental and theoretical results correctly, a procedure was introduced and explained in Section 5.1 for overcoming difficulties encountered as a result of the recorded lack of uniformity in the LWC and DSD fields. As mentioned earlier, the spatial distribution of LWC in the cross-

section of the icing wind tunnel was measured with a 2x2-inch grid using the cylinders placed in the tunnel at different heights. The procedure involves measurement of the local LWC along the cylinder using the circumference of the ice accretion method (Ide,1990) already mentioned. In this method, the local LWC is defined by the following experimental relation:

$$w(x, y) = w_c \cdot \frac{C(x, y) - C_{pipe}(x, y)}{C_c - C_{pipe}(x, y)} \quad (5.4)$$

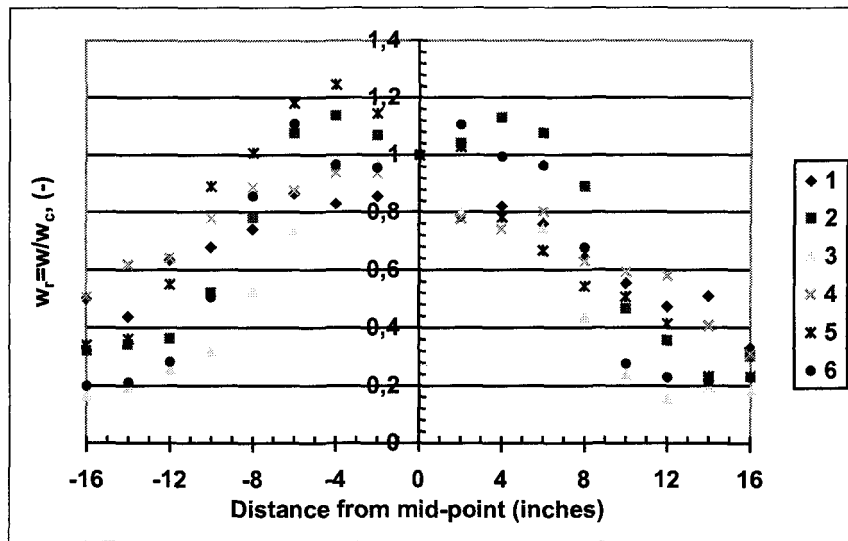


**Fig.5.5.** Experimentally obtained profiles of dimensionless relative LWC,  $w_r$ , along the horizontal centre line of cross-section for different air speeds and various DSD's: 1, 2, and 3, A-type DSD for air speeds  $5 \text{ ms}^{-1}$ ,  $10 \text{ ms}^{-1}$ , and  $15 \text{ ms}^{-1}$ , respectively; 4, 5, and 6, B-type DSD for air speeds  $5 \text{ ms}^{-1}$ ,  $10 \text{ ms}^{-1}$ , and  $15 \text{ ms}^{-1}$ , respectively (Karev et al., 2002).

where  $w(x, y)$  is the LWC at any point in the cross-section;  $w_c$  is the LWC at the mid-point of the test section of the icing wind tunnel;  $C(x,y)$  is the circumference of the ice-covered cylinder at any point in the cross-section;  $C_c$  is the circumference of the ice-covered cylinder at the mid-point; and,  $C_{pipe}$  is the circumference of the bare cylinder. *Figure 5.5* presents the results of such measurements made along the cylinder placed transversal to the flow. Using graphs 5.2 and 5.5, the local LWC along the cylinder

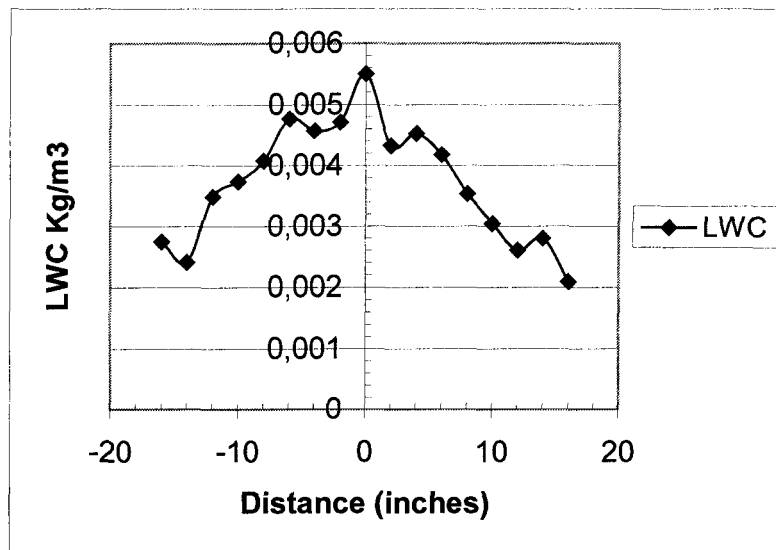


**Fig. 5.6** Distribution of the LWC along the cylinder for the following ambient condition:  $T_a = -5\text{ }^\circ\text{C}$ ,  $V = 5\text{ m s}^{-1}$ , and the nozzle dynamic parameters  $P_a = 25\text{ psi}$ ,  $P_w = 53\text{ psi}$ .

may be obtained. A typical example of such a distribution, obtained from *Figures 5.2* and *5.5*, is presented in *Figure 5.6*.

As may be seen from *Figure 5.5*, two selected DSD's have fairly different LWC's in a lateral direction for the same independent thermodynamic and dynamic parameters (air temperature and air speed). As will be seen later, this fact may produce distinguishable ice masses for specific thermodynamical conditions and specific cylinder diameters, concealing the effect produced by the distinction between the DSD's.

## **5.4. Geometrical Parameters**

### **5.4.1 Cylinder Diameter**

Four 36-inch long aluminum cylinders were used in fixed and rotating icing experiments, with  $\frac{1}{4}$  inch;  $\frac{3}{4}$  inch;  $1\frac{1}{4}$  inches; and,  $1\frac{3}{8}$  inches diameters. Before starting each experiment, the chosen cylinder was placed in a supercooled air stream inside the wind tunnel during the cooling procedure in order for the cylinder to reach the temperature of a supercooled air stream.

### **5.4.2. Shape of Ice Accretion: Icicle Formation**

After each experiment the shape of the ice accretion on the experimental cylinder was recorded by taking a digital photo of the entire cylinder and certain of its characteristic parts, revealing specific features of each ice accretion. As *Figure 5.6* shows, the LWC distribution along the cylinder does not display uniformity. Varying the quantity of the LWC along the cylinder led to non-uniform ice mass distribution in most of the experiments. In the centre, the ice accretion was usually relatively uniform in thickness, while towards the ends of the cylinder, the thickness gradually decreased. For this series, the icicles appeared at a fairly early stage in a number of the experiments, and immediately displayed developing non-symmetry of the growing ice accretion. At the end of the experiments, most of the recorded ice accretion patterns were noticeably asymmetric, even if the icicle formation had not been monitored during experimental unit. The appearance of icicles introduces an entirely new issue into the concept of heat

exchange between the accreting ice surface and the ambient aerosol cloud. By increasing the surface area of the heat exchange and total collection of liquid water on the icing surface, this effect produces considerable changes in the concept of atmospheric icing under conditions of excessive LWC and/or a low degree of ambient supercooling.

### **5.5. Final Adjustment of the model**

In order to carry out a correct evaluation of the experimental results obtained in the wind tunnel, the model was adjusted by introducing: i) a new mass size droplet distribution (MSD); ii) a modification of the MSD; iii) the dependence of evaporation on relative humidity; iv) the dependence of ice density on Macklin's parameter. The results of experimental modelling will be compared to the results of theoretical modelling made for two modes of heat transfer; the first mode is obtained for a smooth heat exchange surface, while the second is for a rough heat exchange surface of accreting ice. An explanation of both modes of heat transfer is provided in Section 4.4.

### **5.6. Results and Discussion**

Figures 5.7 to 5.14 present the modelled ice mass as a function of the cylinder diameter on which ice had accreted, as obtained in experimental and theoretical modelling using the Lozowski et al. (1979) model for various ambient conditions. The comparison of experimental and theoretical results will be made for two modes of heat transfer from accreting icing surfaces: smooth and rough icing surfaces; two types of DSD: A-type (with  $P_a = 25$  psi and  $P_w = 53$  psi), and B-type (with  $P_a = 40$  psi and  $P_w = 53$  psi); two air speeds  $5 \text{ m s}^{-1}$  and  $10 \text{ m s}^{-1}$ ; and, two ambient temperatures  $-5 \text{ }^\circ\text{C}$  and  $-10$

°C. Only one procedure out of three mentioned earlier in this section was used for conversion of the model-yielded icing intensity into the mass of the ice accretion in the results presented. This procedure was the simple extrapolation in time for constant cylinder diameter.

### 5.6.1. Conditions of High and Ultra-High LWC

As mentioned earlier, due to the dependence of the LWC on the air speed, each type of DSD in the results presented corresponds to a specific value of LWC for given values of air speed. The effect of DSD on the final mass accretion cannot be investigated, however, since it is concealed by the more pronounced effect of the LWC. *Figures 5.7 through 5.10*, in particular, which present the results of modelling of the icing process obtained with an A-type DSD (MVD= 57  $\mu\text{m}$ ), correspond to a LWC of 5.4  $\text{g m}^{-3}$  and 5.6  $\text{g m}^{-3}$  for air speeds 5  $\text{m s}^{-1}$  and 10  $\text{m s}^{-1}$ , respectively. *Figures 5.11 through 5.14*, which present the results of modelling of the icing process obtained with a B-type DSD (MVD= 42  $\mu\text{m}$ ), correspond to a LWC of 8.7  $\text{g m}^{-3}$  and 9.2  $\text{g m}^{-3}$  for air speeds 5  $\text{m s}^{-1}$  and 10  $\text{m s}^{-1}$ , respectively, (see *Figure 5.2*, line 2, which represents an A-type DSD, and line 4 which represents a B-type DSD). When comparing the corresponding figures for the same thermodynamic conditions, but for different DSD's, as for example *Figure 5.7 and Figure 5.11*, it may be observed that the ice mass obtained for a B-type DSD is always greater than the corresponding ice mass for an A-type DSD. Such a result appears to be due to the effect of LWC, which is greater for the B-type DSD, as mentioned above. This is in spite of the fact that the collection efficiency for a B-type DSD is lower for the same dynamic conditions as a result of a lower MVD. In other words, the effect of the

increased LWC for the B-type DSD conceals the effect of a decreased collection efficiency compared to the A-type DSD. Under such conditions, it is impossible to reveal any influence of different DSD's on the final experimentally-modeled ice mass, while the effect of the LWC, however, is revealed very clearly when comparing the two conditions mentioned. Therefore, from now on, the A-type DSD will represent conditions with high LWC, and the B-type DSD will represent conditions with ultra-high LWC.

### **5.6.2. Effect of Excessive LWC**

As is observable at first sight, the experimentally-modelled ice mass, for conditions of ultra-high LWC is always greater than the theoretically modelled one (see *Figures 5.11 through 5.14*). Under conditions of high LWC, there is a high degree of coincidence between the experimentally and theoretically modelled ice masses (*Figures 5.7 through 5.10*). Under such conditions of high LWC, the difference between the experimental and theoretical results is greater for the cylinder with a smaller diameter as a result of the application of a simple extrapolation in time. The coincidence between theoretical and experimental results here, for cylinders with greater diameters, is almost perfect when the heat transfer from a rough surface is considered in the model, and relatively good when the heat transfer from a smooth surface is considered (except under conditions of cold icing as presented in *Figure 5.10*). Under conditions of excessive LWC, to explain the results entails more complexity, because of the influence of several independent effects. The difference between the experimentally- and theoretically-modelled results, however, even under such conditions, diminishes by increasing the cylinder diameter. This difference is a result of the simplification in integration of ice mass over time by simple

interpolation with a constant cylinder diameter, while in reality the diameter of the accumulated ice sample increases progressively over the duration of the experiment.

### **5.5.3. Effect of Cylinder Diameter**

The considerably distinct behaviour of the final ice mass as a function of the cylinder diameter may be noted, when comparing the results of theoretical and experimental modelling. Though the theoretical modelling promotes the pronounced dependence of the ice load on the cylinder diameter in both heat transfer modes considered in the model, the results of the experimental modelling are evidence of the completely different behaviour of the ice load with regard to the cylinder diameter. It may be a closely constant function (*Figure 5.7*), slightly increasing function (*Figures 5.8, 5.9 and 5.13*), slightly decreasing function (*Figure 5.12*), or decreasing/increasing function (*Figures 5.11, 5.10 and 5.14*) of the cylinder diameter in the range of the dimensions considered in the experiments. Such indifferent behaviour of the ice load with respect to the cylinder diameter on which the ice accreted, had already been predicted and obtained in theoretical and experimental investigations (Makkonen, 1986). In the study, the ice load was independent of cylinder diameter in the range of conditions representing the regions with different icing regimes and the transition areas between them. This investigation confirms the results obtained earlier, while it also suggests an independence of the ice load from the cylinder diameter in a wider range of ambient conditions representing the wet regimes with shedding and without. The differences arising in the results of theoretical and experimental modelling may be explained by excluding the

phenomenon of icicle formation in the theoretical modelling for ultra-low and low air speeds, and for excessive LWC.

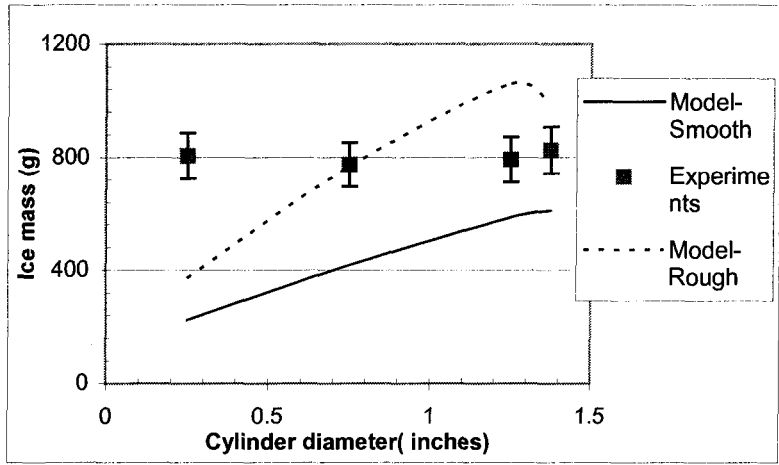


**Fig. 5.7.** Comparison of the results of experimental and theoretical modelling obtained for two heat transfer modes: smooth and rough surfaces. Ambient conditions: A-type DSD ( $MVD=57\mu\text{m}$ ) with air temperature  $T_a = -5\text{ }^\circ\text{C}$ , and air speed  $V_a = 5\text{ m s}^{-1}$

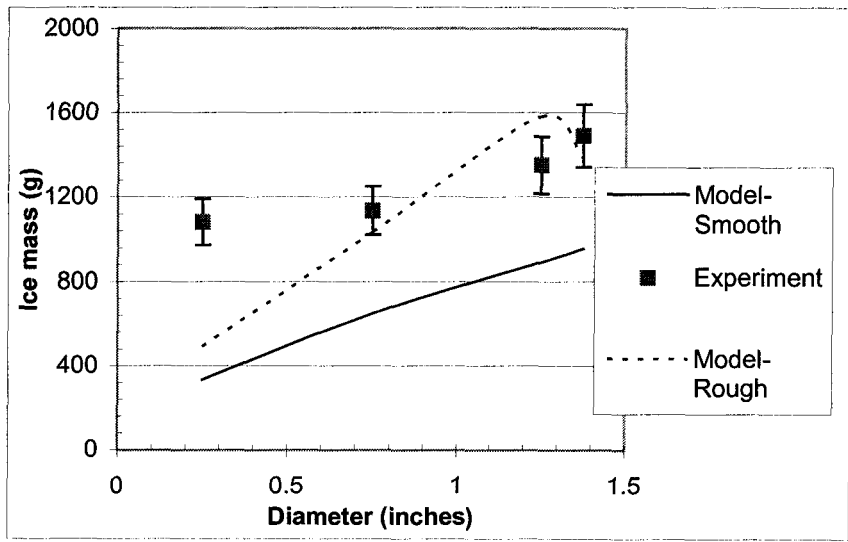


**Fig. 5.8.** Comparison of the results of experimental and theoretical modelling obtained for two heat transfer modes: smooth and rough surfaces. Ambient conditions: A-type DSD ( $MVD=57\mu\text{m}$ ) with air temperature  $T_a = -5\text{ }^\circ\text{C}$ , and air speed  $V_a = 10\text{ m s}^{-1}$

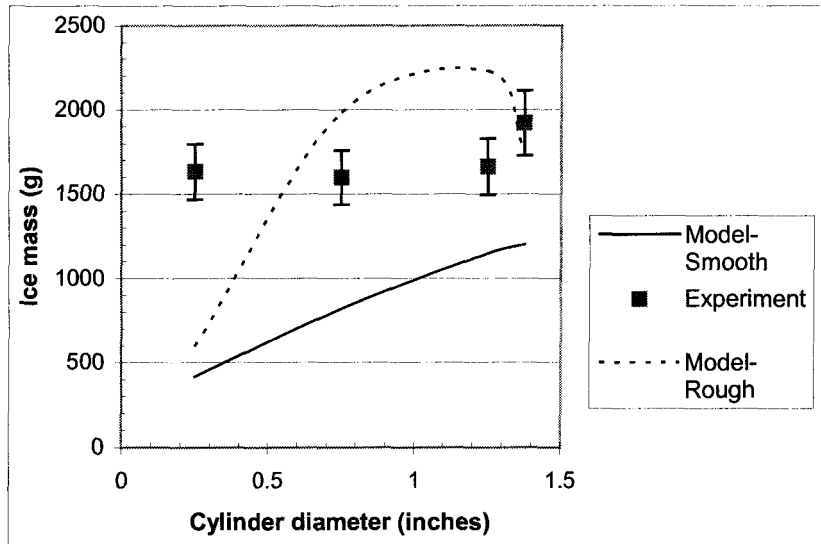


**Fig. 5.9.** Comparison of the results of experimental and theoretical modelling obtained for two heat transfer modes: smooth and rough surfaces. Ambient conditions: A-type DSD ( $MVD=57\mu\text{m}$ ) with air temperature  $T_a = -10^\circ\text{C}$ , and air speed  $V_a = 5\text{ m}\cdot\text{s}^{-1}$

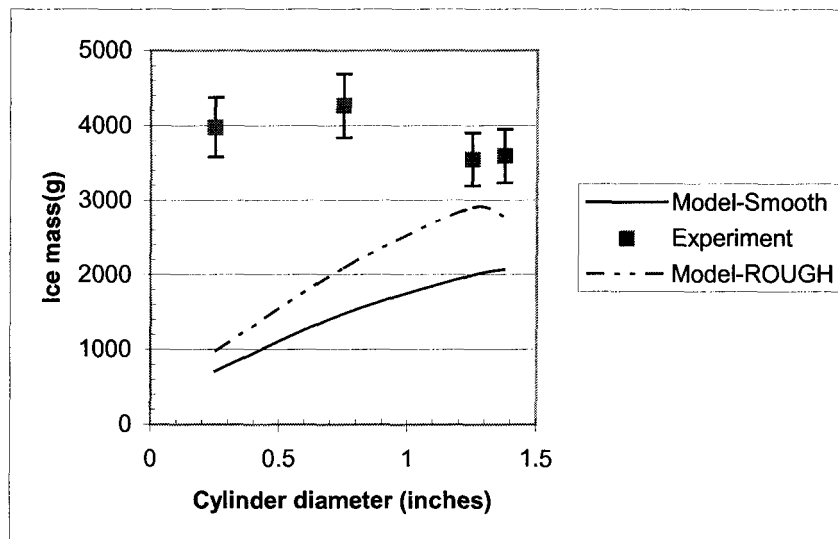


**Fig. 5.10.** Comparison of the results of experimental and theoretical modelling obtained for two heat transfer modes: smooth and rough surfaces. Ambient conditions: A-type DSD ( $MVD=57\mu\text{m}$ ) with air temperature  $T_a = -10^\circ\text{C}$ , and air speed  $V_a = 10\text{ m}\cdot\text{s}^{-1}$

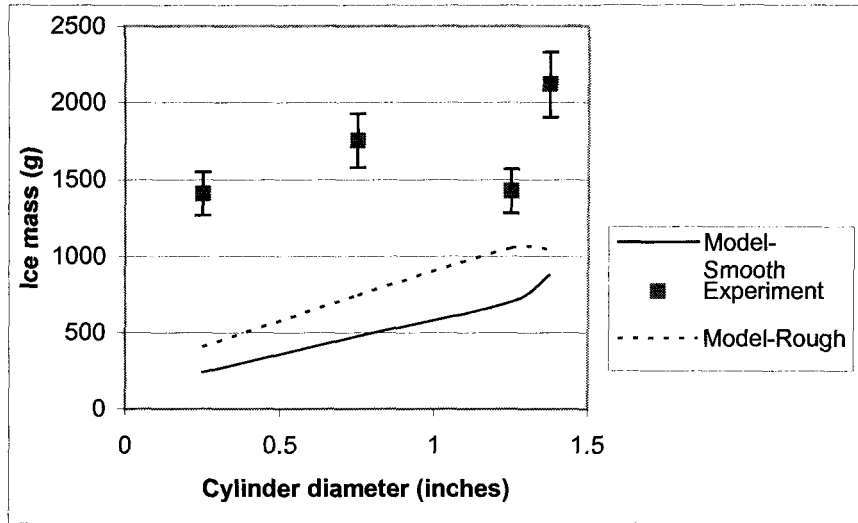


**Fig. 5.11.** Comparison of the results of experimental and theoretical modelling obtained for two heat transfer modes: smooth and rough surfaces. Ambient conditions: B-type DSD (MVD= 42  $\mu\text{m}$ ) with air temperature  $T_a = -5^\circ\text{C}$ , and air speed  $V_a = 5\text{ m s}^{-1}$

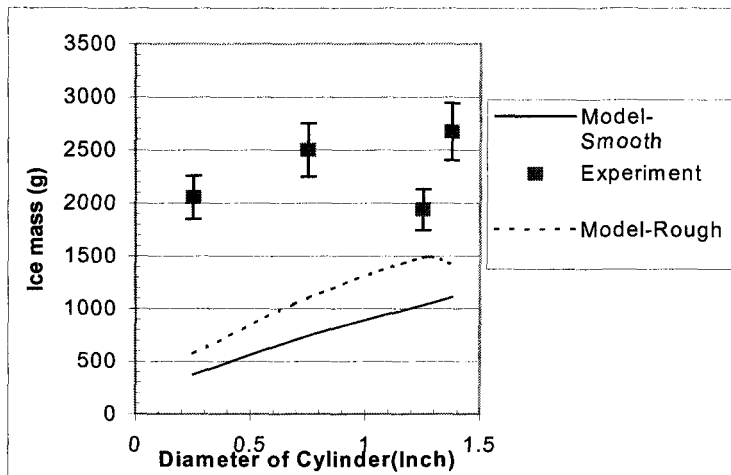


**Fig. 5.12.** Comparison of the results of experimental and theoretical modelling obtained for two heat transfer modes: smooth and rough surfaces. Ambient conditions: B-type DSD (MVD= 42  $\mu\text{m}$ ) with air temperature  $T_a = -5^\circ\text{C}$ , and air speed  $V_a = 10\text{ m s}^{-1}$

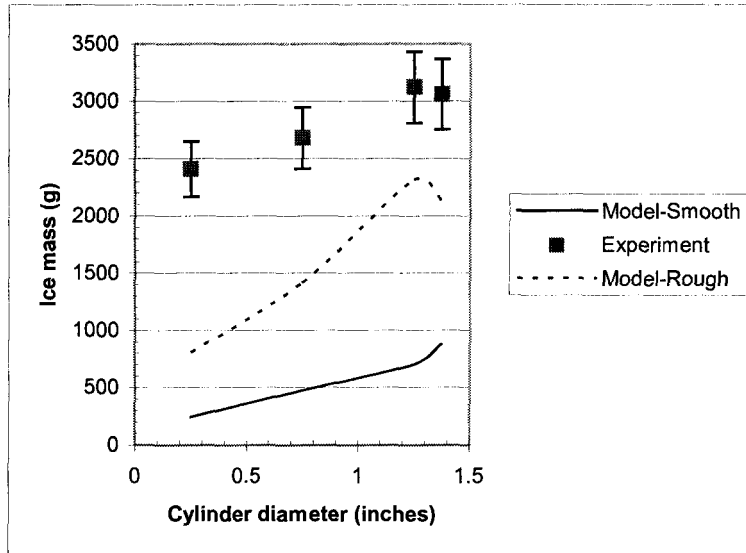


**Fig. 5.13.** Comparison of the results of experimental and theoretical modelling obtained for two heat transfer modes: smooth and rough surfaces. Ambient conditions: B-type DSD (MVD= 42 $\mu$ m) with air temperature  $T_a = -10$  °C, and air speed  $V_a = 5$  m·s<sup>-1</sup>

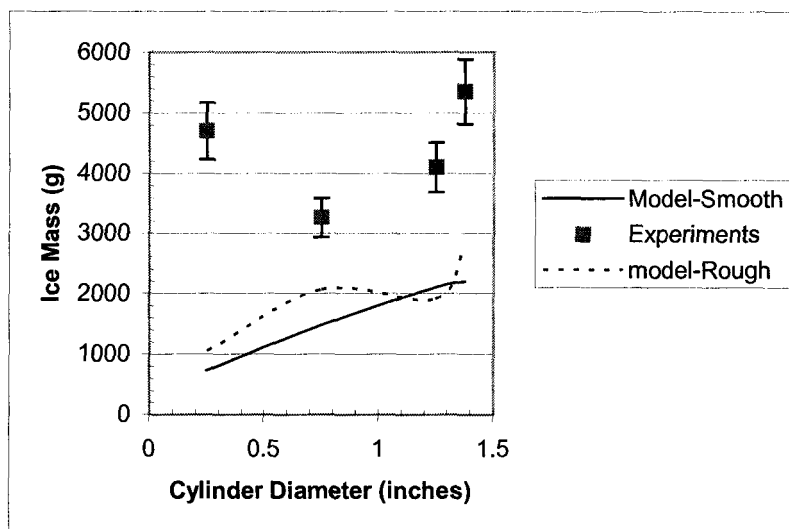


**Fig. 5.14.** Comparison of the results of experimental and theoretical modelling obtained for two heat transfer modes: smooth and rough surfaces. Ambient conditions: B-type DSD (MVD= 42 $\mu$ m) with air temperature  $T_a = -10$  °C, and air speed  $V_a = 10$  m·s<sup>-1</sup>

## 5.6. Concluding Remark

The model predicts to a good degree, the mass of ice load under conditions of high LWC ( $5 \text{ gm}^{-3}$  to  $6 \text{ gm}^{-3}$ ) for all cylinder diameters except for the smallest one. Under conditions of ultra-high LWC ( $9 \text{ gm}^{-3}$  to  $11 \text{ gm}^{-3}$ ) and low air flow ( $5 \text{ ms}^{-1}$  to  $10 \text{ ms}^{-1}$ ), it underestimates the natural ice load. A two-dimensional representation of the ice accretion in a mathematical model and a pre-assumed leeward direction of water film flow are the limitations of the model preserving incorporation of icicle model and incorporation of the phenomenon of rivulet formation. The model, however, may easily be developed into 3-D shape.

## **CHAPTER 6**

### **COMPARISON OF THE EXPERIMENTAL RESULTS WITH MODEL PREDICTIONS: VERIFICATION OF THE MAKKONEN MODEL (1984)**

#### **6.1. SELECTING A Basis for Comparison**

##### **6.1.1 Specifics of Ice Load Calculations**

This comparison will proceed in a similar fashion to the one made for the Lozowski et al. (1979) icing model presented in an earlier chapter, where the mass of ice accreted on the surface of a horizontal non-rotating cylinder for 60 minutes of exposure to a supercooled aerosol flow was chosen as the experimental unit of verification for the model. There are, however, several distinct features of this model, which impose different procedures for ice load calculation.

The first difference here consists in the fact that a slow rotation of the horizontal cylinder is considered in this model. In order to model, experimentally, this rotation of the tested cylinder, the experimental set-up was designed in such a way as to be used for the verification of icing models of both rotating and non-rotating cylinders in the tunnel. This construction, which was described in detail in Chapters 3 and 5, makes it possible to apply three different rates of cylinder rotation: 1, 2, and 5 rpm. In this investigation, only an ultra-slow rotation rate of 1 rpm was used. The rotation of the cylinder is produced by an AC electrical motor transferring the angular momentum to the inner ring of one of two bearings mounted on the walls of the test section of the tunnel. From this bearing, the angular moment was transferred to the experimental cylinder screwed into it. The other end of the cylinder remains unriveted inside the second bearing.

The second distinctive feature of the Makkonen model (1984), when compared to the Lozowski et al. model (1979), consists in the fact that it provides the predicted ice mass accretion directly, where the shape of the ice is assumed to be cylindrical. The model was originally developed for a dry regime of icing on wires, for a wet regime and, particularly, for the transition region between two regimes. The assumption of the cylindrical shape for the ice accretion is, however, not implemented under conditions of ultra-high LWC in an aerosol cloud, as used in some of the experiments in this series (B-type DSD, see section 5.3). As a result of an overabundance of the liquid water supply to the icing surface in the experiments mentioned, the phenomenon of icicle formation could not be avoided. Due to rotation of the experimental object, however, the natural conical shape of icicles was transformed into curved blade-like bumps (protuberances) on the uneven icing surface. At the end of such experiments, the ice accretion was often covered with regular hook-like relatively flat bumps, which, as may be supposed, increase the total water collection on the icing surface considerably by increasing the surface area exposed to a supercooled aerosol flow. The modified shape of the ice accreted resulted in increased heat transfer coefficient and greater production of ice. These changes in the heat transfer coefficient, however, were not taken into account. Quite the contrary, the Lozowski et al. model (1979) makes allowance for different shapes of ice accretion, although the corresponding changes in the heat transfer coefficient are absent as well. As will be seen at the end of this chapter, the absence of a concept for a non-static flexible heat transfer coefficient which is capable of rapid reaction to the changes in shape of the ice accretion, plays a crucial role in the related non-coincidence of experimental and theoretical results obtained under conditions of ultra-high LWC.

The third specific feature of the model under consideration is the fact that the MVD diameter is used for the calculation of aerodynamic and thermodynamic blocks, while in the Lozowski et al. model (1979), the mass droplet size distribution (MSD) with given characteristics was used for the same purposes. Also, it was proven (Makkonen, 1984), that the MVD diameter represents the entire spectrum of droplets with a great level of precision. In the light of possible modification of the DSD in the tunnel depending on the thermodynamic parameters there (Karev and Farzaneh, 2002), however, the last mentioned distinction between the models makes it preferable to use the model with the MSD (Lozowski et al., 1979) rather than the MVD diameter model (Finstad, Lozowski, Makkonen and Gates (1988)).

### **6.1.2 Spatial Integration Procedure**

Since the output of the model is the ice mass accreted on a slowly rotating cylinder per unit of length and per unit of time, the angular integration, which was used for modelling ice mass based on the model-yielded angular ice intensity (Lozowski et al., 1979), is not required here. This spatial integration procedure is already subsumed in the model by allowing the cylinder to fulfil a slow rotation which helps to redistribute the unfrozen water over the entire surface of the ice-covered cylinder. Integration over the coordinate lengthwise along the cylinder is carried out in the same way as it is for a non-rotating cylinder using a 2-inch interval. As mentioned in *Chapter 5*, this integration step was imposed by the spatial resolution used during calibration of the LWC and DSD in the tunnel (Karev et al., 2002). The non-uniformity of the spatial field of the LWC, particularly lengthwise along the cylinder, as obtained during the above-mentioned

experimental series, dictates such a procedure for the calculation of the ice mass by analogy with the one presented in *Chapter 5*. The only difference in this case is the fact that the mass of ice accretion is used for integration lengthwise along the cylinder instead of the icing intensity used in the model for the non-rotating cylinder. In doing this procedure of integration, however, an initial assumption about the shape of the ice accretion in the model is violated, wherein this shape is cylindrical. The lateral cross-sections of the ice accretions formed in this series were, more often than not, *biconvex lenticular or ellipsoidal* in shape, indicating *lenticular or ellipsoidal cylinders* as shape for the entire ice accretions. In order to use the same formula for heat transfer coefficient, as was used in the model, it is necessary to suppose that, in general, the entire heat transfer from the bodies having exact cylindrical and biconvex lenticular cylindrical shapes is closely the same as from cylindrically-shaped bodies.

### **6.1.3. Ice Sample Density, Ice Sponginess and Rotation of Experimental Cylinder**

The density of the growing ice accretion at the cross-section three points: midpoint, and 20 cm right and left of the centre were regularly checked after each experiment. This ice density was measured using the same displacement method described in the previous chapter, i.e. immersing the accretion sample, collected from the angular location close to the stagnation line, in oil of a known density, and then measuring the Archimedes force. The experimentally obtained values of ice density were compared to those predicted by the model. Ice density, under all ambient conditions employed in this series of experiments was always equal to a maximum ice density,  $\rho_i = \rho_{i,0}$ .

A far more interesting issue in this experimental series is the influence of rotation on the morphology of ice accretion, on its density and, particularly, on its sponginess. To the best of our knowledge, there have been no similar investigations made, to date. It is not possible to find any relationship between the ice density and the nature of the exposure of the icing object (cylinder) to a supercooled aerosol cloud by comparing the density of the ice samples from rotating and non-rotating series (see *Figure 5.1.*), This does not, however, imply that a relationship does not exist. It is clear that the rotation of the icing body should result in the redistribution of the water supply to its surface. In this experimental series under high and ultra-high LWC, however, this redistribution has not any effect on the density of growing ice. By decreasing the LWC it would probably be possible to obtain a contrary result, arising from permanent changes in the local phase state of the surface through rotation. Such an effect would emerge under conditions promoting the change of icing regime. Further investigation into this field will cast greater light on the role of the manner of exposure of an icing object, as well as on the nature of its motion with regard to the changes in the local density of a growing ice layer.

## **6.2. Experimental Conditions**

The experimental conditions chosen for a rotating cylinder series were exactly the same as for a non-rotating series, as presented in the previous chapter. The entire discussion with regard to the division of the thermodynamic and dynamic parameters into two principal groups is applicable to this series also.

### **6.2.1 Air Temperature and Air Speed**

The pre-selected temperatures for the experiments were the same as for the non-rotating series:  $-5\text{ }^{\circ}\text{C}$  and  $-10\text{ }^{\circ}\text{C}$ . The two low air speeds for the experiments were set at  $5\text{ m}\cdot\text{s}^{-1}$  and  $10\text{ m}\cdot\text{s}^{-1}$ . As mentioned earlier, low air speed was chosen in both series to model the most frequent dynamic conditions prevailing during freezing rain phenomena in nature.

### **6.2.2. LWC and DSD**

The two selected water DSD's are exactly same as those that were used during the experiments with a non-rotating cylinder, and described in the previous chapter. Also, as mentioned in *Chapter 5*, an A-type DSD (MVD=  $57\text{ }\mu\text{m}$ ) corresponds to a LWC of  $5.4\text{ g}\cdot\text{m}^{-3}$  and  $5.6\text{ g}\cdot\text{m}^{-3}$  for air speeds of  $5\text{ m}\cdot\text{s}^{-1}$  and  $10\text{ m}\cdot\text{s}^{-1}$ , respectively, and produces conditions with a high LWC. A B-type DSD (MVD=  $42\text{ }\mu\text{m}$ ) corresponds to a LWC of  $8.7\text{ g}\cdot\text{m}^{-3}$  and  $9.2\text{ g}\cdot\text{m}^{-3}$  for air speeds  $5\text{ m}\cdot\text{s}^{-1}$  and  $10\text{ m}\cdot\text{s}^{-1}$ , respectively, and produces conditions with an ultra-high LWC.

### **6.3. Geometrical Factors**

Experimental cylinders with a diameter of  $\frac{1}{4}$  inch;  $\frac{3}{4}$  inch;  $1\frac{1}{4}$  inches and  $1\frac{3}{8}$  inches each, were used for the experiments.

### **6.4 Two Modes of Heat Transfer-based on works of Makkonen(REF: 24)**

The rate of heat transfer from an icing object is directly dependent on the roughness conditions of the icing surface. Increasing the roughness tends to increase the heat transfer rate, and it also causes an earlier transition from a laminar to a turbulent

layer. “To calculate the roughness, the Makkonen model makes use of a boundary-layer model, similar to that of MacArthur (1981), which determines the local heat transfer coefficient over the front half of a *circular* cylinder. The basic formula for calculating the roughness is the Bernoulli relation used in heat transfer calculations. Using this approach, the Makkonen model assumes an infinitely long circular icing cylinder. Also, the boundary layer of a supercooled airflow is steady and two dimensional, as well as incompressible on an icing surface from  $\theta=0^\circ$ (stagnation point) to  $\theta=90^\circ$ , where  $\theta$  is the angle from stagnation line. It was also assumed that the ratio of the boundary layer thickness to the cylinder diameter is so small that curvature can be disregarded. The air properties are assumed to be constant, and the temperature of the surface is constant, at 0 °C (wet regime of ice accretion); under these assumptions the equation for the boundary layer under forced convection is reduced to:

$$u \frac{\partial u}{\partial x} + v \frac{\partial u}{\partial y} = -\frac{1}{\rho} \frac{dp}{dx} + \frac{1}{\rho} \frac{\partial \tau}{\partial y} \quad (6.1)$$

where  $u$  and  $v$  are the flow velocity components,  $\rho$  is the air density,  $p$  is the pressure and  $\tau$  is the sheer stress at  $y=0$ . The continuity equation may be written as follows:

$$\frac{\partial u}{\partial x} + \frac{\partial v}{\partial y} = 0 \quad (6.2)$$

and the boundary conditions are:

$$y=0, v=0, w=0; \quad (6.3)$$

$$y=\infty \quad u=u_\infty(x), v=0 \quad (6.4)$$

The solution to equation (6.1), which is obtained by integrating with respect to the variable  $y$  from  $y=0$  to  $y=\infty$ , was applied to the different regions of airflow movement (laminar, turbulent, transition). This made it possible to obtain several relations for calculation the coefficient of heat transfer convection,  $H$ . For laminar free stream flow, the Nusselt number may be expressed as follows:

$$Nu_L(x) = \frac{h(x)D}{Ka} = \frac{0.293Du_\infty^{1.435}(x)}{v^{0.5} \left( \int_0^x u_\infty^{1.87}(x) dx \right)^{0.5}} \quad (6.5)$$

For the turbulent region the Nusselt number is:

$$Nu_T(x) = \frac{St(x)u_\infty \rho C_p}{Ka} \quad (6.6)$$

where  $\rho$  is the air density;  $C_p$  is the specific heat capacity of air;  $D$  is the cylinder diameter; and,  $u_\infty$  is the air velocity outside the boundary layer obtained from the assumption of potential flow, which is defined as follows :

$$u_{\infty}=1.58 \sin (1.233\theta (x)) u, \quad (6.7)$$

and

$$\theta=2x/D \quad (6.8)$$

$St$  is the Stanton number based on the friction velocity and is calculated from the investigation carried out by Kays and Crawford (1980) for developed turbulent flow over completely rough surfaces”[Ref: 24].

## 6.5. Results and Discussion

Figures 6.1 through 6.8 show the comparison of the experimental and theoretical results under conditions with high LWC defined by an A-type DSD (where the 3 nozzle dynamical parameters are  $P_a=25$ psi;  $P_w=53$  psi; and water flow rate  $F=0,3$  cm<sup>3</sup>/min per channel) and under conditions of ultra-high LWC defined by a B-type DSD (where the nozzle dynamical parameters are  $P_a=40$  psi;  $P_w=53$  psi; water flow rate  $F=0.2$  cm<sup>3</sup>/min per channel).

### 6.5.1. Effect of Excessive LWC

From the first investigation of the experimental and theoretical results in Figures 6.1 through 6.8, it may be concluded that, under all the experimental conditions considered in this study, the model overestimates the natural ice load, presented here by the experimental data from the wind tunnel. This behaviour of the model outcomes may be expected when the initial range of applicability of the model is taken into account. In fact, the model was developed preferable for application under conditions producing

transition of ice growth regime from wet icing regime to dry icing regime and also under conditions producing ice growth regimes close to this transition region between two distinct ice regimes. Application of the model to conditions of high and ultra-high LWC's reveals a number of its limitations under specific conditions. The fact that, for cold icing conditions with high LWC (*Figure 6.3.*) the coincidence is better than for warm conditions, confirms the observation about the limitation of the model applicability for ultra-high LWC. Also, as may observe at first sight, under conditions of high LWC (*Figures 6.1 to 6.4*), the degree of coincidence between the experimentally and theoretically modelled results is relatively good, in comparison to the experiments under conditions of ultra-high LWC. When comparing the difference between the experimental and theoretical results with corresponding differences obtained in the non-rotating cylinder series, however, it may be noticed that the difference in this series is minimal for the smallest cylinder diameter as opposed to the series with a non-rotating cylinder. This observation is based on the fact that, for the smallest cylinder diameter, the total water collection on the icing surface is minimal. The overestimation of the ice load by the model is usually maximal for the largest cylinder diameter. In particular, there is a higher frequency of non-coincidence between the theoretical and experimental results to be observed for conditions of ultra-high LWC, which in fact, confirms the statement that the applicability of the model, in its present form, cannot be expanded to the conditions of high and ultra-high LWC characteristic of freezing rain phenomena.

### **6.5.3. Effect of Cylinder Diameter**

Examination of the experimental results, as compared to the theoretical predictions provided by the model with regard to cylinder diameter, reveals the same developments

in the behaviour of the experimental data as were observed in the non-rotating series. That is to say, under the conditions investigated in this study, the ice mass accreted on a cylindrical body does not depend on the cylinder diameter.

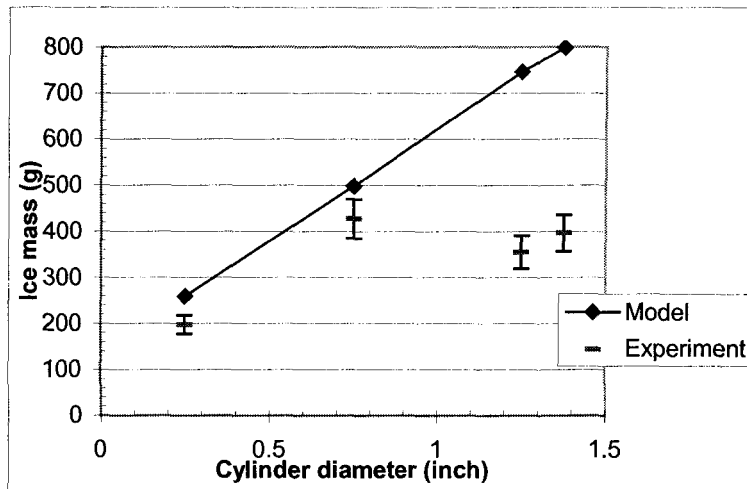


**Fig. 6.1.** Comparison of the experimentally obtained ice mass with the one theoretically predicted by using the Makkonen model (1984); Ambient conditions: A-type DSD ( $MVD = 57 \mu\text{m}$ ) with air temperature  $T_a = -5 \text{ }^\circ\text{C}$ , and air speed  $V_a = 5 \text{ m s}^{-1}$

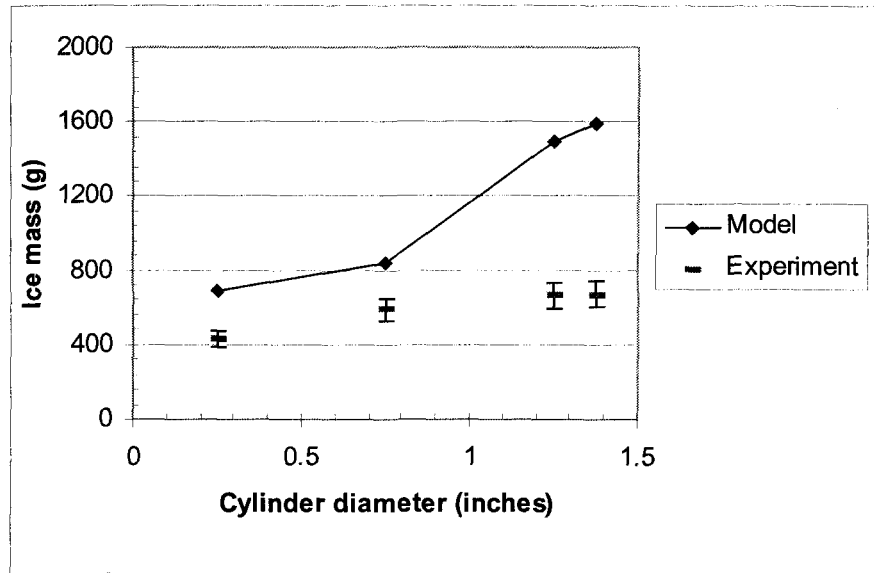


**Fig. 6.2.** Comparison of the experimentally obtained ice mass with the one theoretically predicted by using the Makkonen model (1984); Ambient conditions: A-type DSD (MVD= 57 $\mu$ m) with air temperature  $T_a = -5$  °C, and air speed  $V_a = 10$  m s $^{-1}$

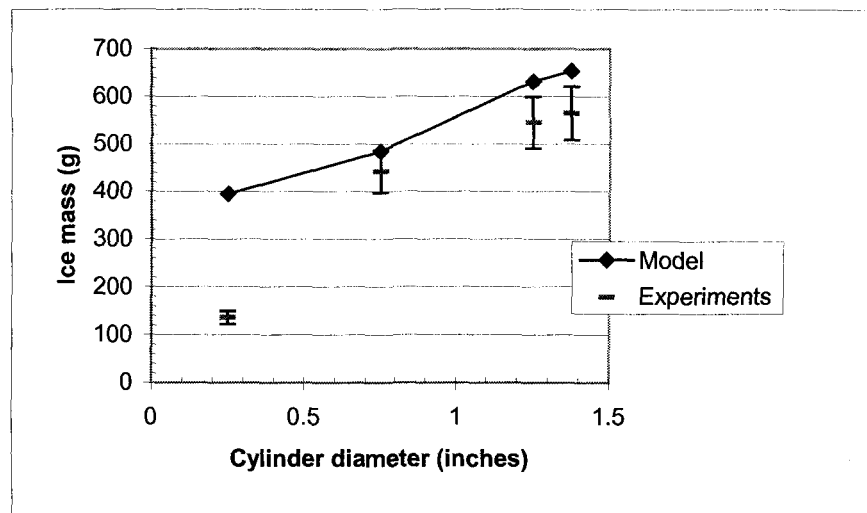


**Fig. 6.3.** Comparison of the experimentally obtained ice mass with the one theoretically predicted by using the Makkonen model (1984); Ambient conditions: A-type DSD (MVD= 57 $\mu$ m) with air temperature  $T_a = -10$  °C, and air speed  $V_a = 5$  m s $^{-1}$

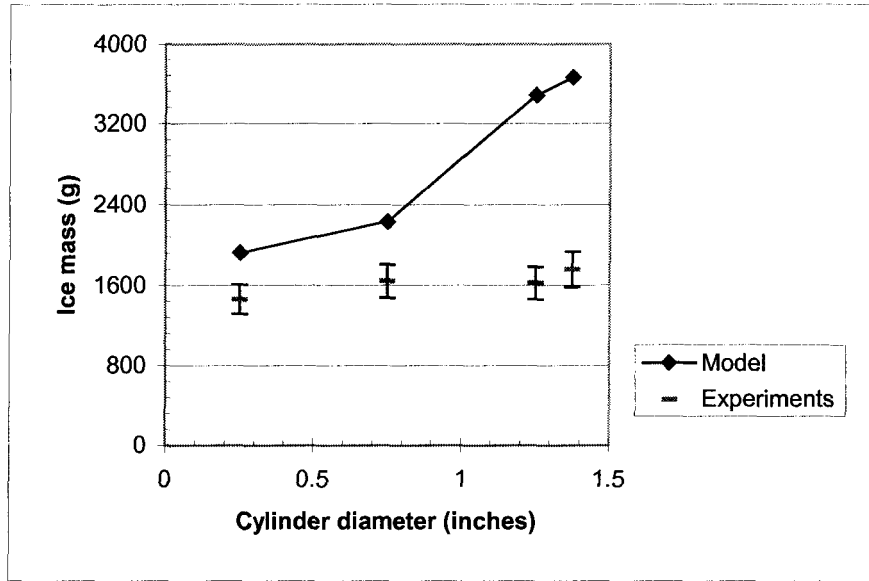


**Fig. 6.4.** Comparison of the experimentally obtained ice mass with the one theoretically predicted by using the Makkonen model (1984); Ambient conditions: A-type DSD ( $MVD= 57\mu\text{m}$ ) with air temperature  $T_a= -10\text{ }^\circ\text{C}$ , and air speed  $V_a=10\text{ m}\cdot\text{s}^{-1}$

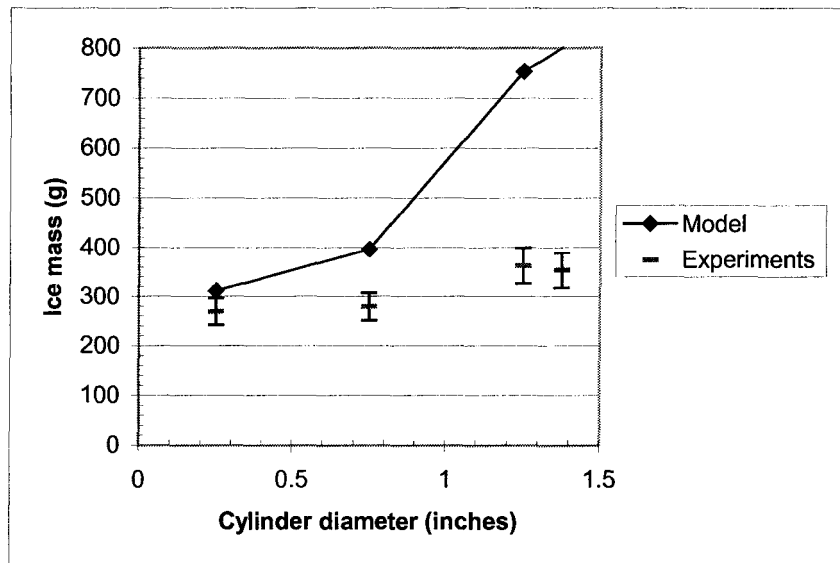


**Fig. 6.5.** Comparison of the experimentally obtained ice mass with the one theoretically predicted by using the Makkonen model (1984); Ambient conditions: B-type DSD ( $MVD= 42\mu\text{m}$ ) with air temperature  $T_a= -5\text{ }^\circ\text{C}$ , and air speed  $V_a=5\text{ m}\cdot\text{s}^{-1}$

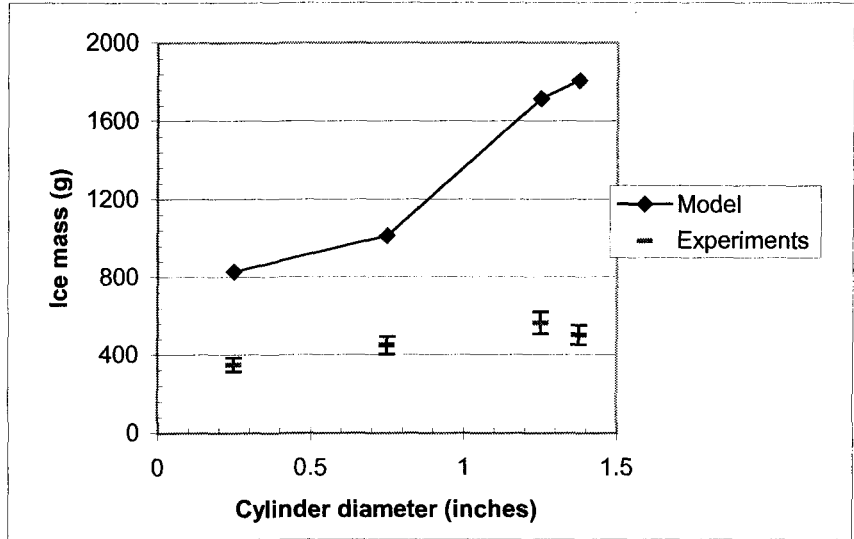


**Fig. 6.6.** Comparison of the experimentally obtained ice mass with the one theoretically predicted by using the Makkonen model (1984); Ambient conditions: B-type DSD ( $MVD=42\mu\text{m}$ ) with air temperature  $T_a = -5\text{ }^\circ\text{C}$ , and air speed  $V_a = 10\text{ m s}^{-1}$

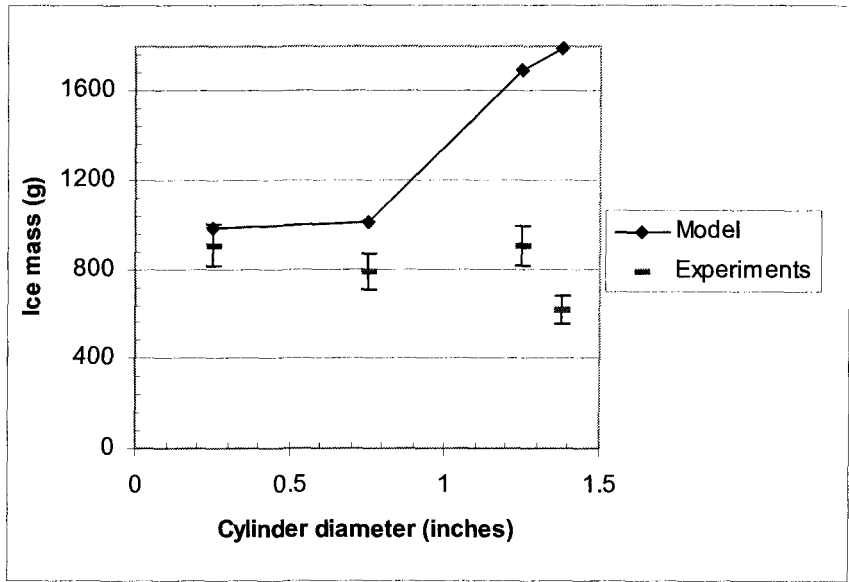


**Fig. 6.7.** Comparison of the experimentally obtained ice mass with the one theoretically predicted by using the Makkonen model (1984); Ambient conditions: B-type DSD ( $MVD=42\mu\text{m}$ ) with air temperature  $T_a = -10\text{ }^\circ\text{C}$ , and air speed  $V_a = 5\text{ m s}^{-1}$

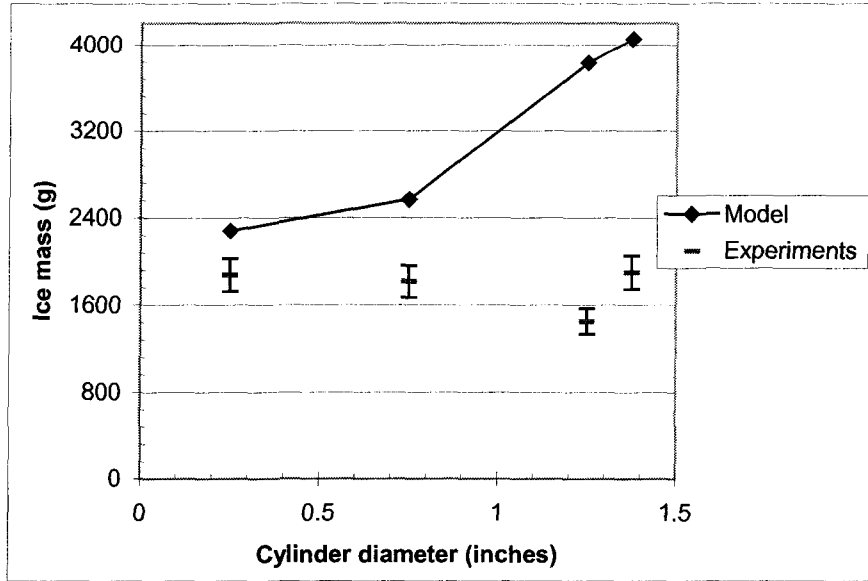


**Fig. 6.8.** Comparison of the experimentally obtained ice mass with the one theoretically predicted by using the Makkonen model (1984); Ambient conditions: B-type DSD ( $MVD= 42\mu\text{m}$ ) with air temperature  $T_a= -10\text{ }^\circ\text{C}$ , and air speed  $V_a=10\text{ m}\cdot\text{s}^{-1}$

## 6.6. Conclusion

The model predicts to a satisfactory degree, what would be the mass of ice load under conditions of high LWC for the small and medium cylinder diameters. Under conditions of ultra-high LWC, the predictability of the model is relatively poor, especially for the large cylinder diameter. The limitation of the model lies in the fact that the freezing fraction and heat transfer coefficient are calculated for the entire ice accretion. This, however, under conditions of ultra-high LWC, produces an overestimation of real ice load due to impossibility of accurately taking into account the processes of shedding and stripping of water from the freezing surface. The rotation is

incorporated in the model implicitly and this produces a discrepancy between the theoretical and experimental results.

## **CHAPTER 7**

### **SUMMARY AND RECOMMENDATIONS**

In the first part of this chapter, a comparative evaluation is made of the results obtained from the rotating and non-rotating cylinder series for both theoretical and experimental modelling. The comparison helps to reveal the advantages of the models under discussion and to provide a qualitative assessment of the level their accuracy and predictive capacity as regards the mass of ice under the ambient conditions investigated in this series. The second part of this chapter enumerates the sequence of the processes to be taken into account for improving the quantitative results of the prediction and diagnosis of the ice mass accreted under given conditions. Finally, recommendations are presented for the manner of use of the models and for further investigation in this field.

#### **7.1. Mutual Comparison of Rotating and Non-Rotating Icing Cylinders Series:**

##### **Experimental and Theoretical Results**

The two atmospheric icing models presented here were evaluated theoretically and experimentally for the degree of their potential for the correct prediction of ice accreted on a cylindrical surface, whether rotating and non-rotating, during freezing rain phenomena, modelled here through the ambient conditions of high or ultra-high LWC. The evaluation of the two selected atmospheric icing models is made with a view to their potential application in the modelling of a specific type of atmospheric ice accretion, called glaze ice, forming on overhead transmission lines (OHTL) during freezing rain atmospheric phenomena. The latter is modelled by the ambient conditions of high or

ultra-high LWC in flowing aerosol cloud inside a wind tunnel. It should be noted that both models were originally developed for a different application from the one presented in this study and they were subsequently applied to a wider range of thermodynamic conditions. It is highly probable that, due to this fact, both models do not always display the exact same behaviour as that of OHTL cable. In fact, the cable cannot be represented by a non-rotating horizontal cylinder when the icing model is applied, which was provided by Lozowski et al. (1979), nor can it rotate at 1 rpm which facilitates the homogeneous redistribution of unfrozen water around the cylinder. The natural degree of cable rotation, as it is predicted by the theory and presented by the results of the experimental investigation, is considerably slower than it is in such experimental modelling. As it was noted in the previous chapter, this fact may play a crucial role in the modelling of the heat transfer coefficient and the freezing fraction from the icing surface.

A comparative verification is presented of the results obtained in the experimental series with rotating and non-rotating cylinders experiments, supplied additional theoretical evaluation of the results obtained when applying the Makkonen model (1984) and the Lozowski et al. model (1979). This comparison may be seen here in *Figures 7.1 through 7.8*.

*Figures 7.1 through 7.4* present theoretical and experimental results obtained under conditions of high LWC (A-type DSD with the nozzle dynamic parameters  $P_a = 25$  psi,  $P_w = 53$  psi,  $F = 0.3$  cm<sup>3</sup>/min per channel); *Figures 7.5 through 7.8* present theoretical and experimental results obtained under conditions of ultra-high LWC (B-type DSD with the nozzle dynamic parameters  $P_a = 25$  psi,  $P_w = 53$  psi,  $F = 0.2$  cm<sup>3</sup>/min per channel).

In general, under conditions of high LWC, the predictability of both models is better than for conditions of ultra-high LWC. A high level of non-coincidence between experimental and theoretical results for the conditions of ultra-high LWC is based on the absence of a model for icicle growth and model for droplet stripping during rotation of icing object. These problems will be developed in the next section. As a result, it should be mentioned that the model for icing of non-rotating cylinders often underestimates the natural ice mass, particularly under conditions of high LWC. Since a rotation of 1 rpm under conditions of high LWC promotes adequate stripping and shedding of excess of water from the surface of the accreting ice, the model for the icing of rotating cylinders under such a condition overestimates the natural ice mass. As regards the different cylinder diameters, under conditions of high LWC, the non-rotating cylinder model predicts better ice mass for the largest cylinder diameter, and underestimates it for the small cylinders. The rotating cylinder model provides better results for small diameters. This is a consequence of the method of time integration used in the study, as mentioned in *Chapter 5*, that is to say, interpolation for a constant radius. By using the alternative method of time integration, which incorporates, for example, the concept of effective diameter, the result will be improved considerable. Under conditions of high LWC, the model for rotating cylinders, however, is a good predictor for the ice mass on the cylinders with small diameters, but overestimates it for the large diameters. Both models propose the power dependence of ice mass accreted on the surface of icing cylinders, while the experimental results from both series, however, confirm that this type of dependence does not exist.

## 7.2. Process to be Developed and Incorporated in Appropriate Icing Code

The mass of ice accretion obtained in the wind tunnel experiment, is frequently different from the mass of ice calculated by the model. This discrepancy may be explained by the following:

1. As may be seen from the experimental and theoretical results presented, the roughness of the accreting surface may have a pronounced effect on the final ice mass accumulation. The introduction of the roughness factor usually closes the gap between results obtained theoretically and experimentally. It should be noted, that the effect produced by surface roughness was accounted for in the non-rotating cylinder model (Lozowski et al., 1979) by using Achenbach's (1974) formula to include the influence of homogeneous surface roughness on an increase of heat transfer to the air stream. An appropriate heat transfer formula was put forward with the surface roughness to be decided *a posteriori*, taking into account the highly complex and unsteady behavior of surface roughness, which is a natural consequence of the prevailing thermodynamic conditions as well as of the relevant angle formed with the stagnation line. The behavior of the roughness zone is, in actual fact, far more complex than previously believed and it is distinctly unsteady. The expanding zone of roughness influences the air boundary layer, provoking an increase in local heat transfer, which, in turn, accelerates the process of expansion of the zone. The same reasoning may be applied to a rotating icing cylinder model (Makkonen, 1984)

2. The processes of icicle formation, droplet stripping and shedding during rotation of the icing object affect the final outcome of experimental modelling. Both models disregard the formation of icicles as a factor, although experimental modelling was frequently accompanied by icicles. The conditions which would effectuate the rapid appearance of icicles are characterized by the presence of one or several of the following alternatives: excessive LWC; ultra-low ambient supercooling, when the air temperature is close to  $0^{\circ}\text{C}$ ; and/or abundant liquid water flux to the icing surface. The non-rotating cylinder model was developed for moderate-to-strong air shear stresses capable of overcoming the influence of gravity, which impedes the rapid development of water film flow on the upper half of the cylinder. Under weak air shear stresses, at airspeeds applied in this series of experiments from  $5\text{ m s}^{-1}$  to  $10\text{ m s}^{-1}$ , which are not strong enough to overcome the influence of gravity over the greater part of the surface of the upper half of the cylinder, the water film flows counter-current to the air stream towards the lower half of the cylinder. Further accumulation of water results in the formation of a wavy water surface at the bottom of the cylinder with the subsequent development of ripples. The water film, in this case, is governed by gravity and surface tension alone, and has, as a result, icicle formations growing from the bottom of the lower half of a horizontal cylinder. The processes of water droplets stripping and shedding from the icing surface during its rotation are still poorly investigated. Physical understanding of these processes will help to improve the rotating cylinder model (Makkonen, 1984).

3. Concurrent air and water film flow on the cylindrical icing surface was assumed in the original model (Lozowski et al., 1979) for application under conditions of aircraft

icing, when the water film starts to flow from a certain location fairly close to the stagnation line under the influence of strong air-created shear stress. In other words, it was assumed that the water film always flows in a direction that goes from the stagnation line towards the rear of the cylinder, i.e. when the angular coordinate changes from around  $0^\circ$  to  $90^\circ$ . This is, in fact, the reason why the icing model is called a water runback model. This assumption cannot be applied to most of the experimental conditions used in this series of experiments. As described above, under conditions of weak air shear stresses, the water film forming on the icing surface flows counter-current to the air stream towards the lower half of the cylinder. From a certain angular position, defined mostly by air speed and liquid water supply, when the growing air shear stress finally overcomes the impeding effect of gravity, the water film starts to flow in a backward direction. The rate of water flow, however, is not high enough to form a continuous flow, which, under such conditions, usually divides into separate rivulets. The rivulets may convert into ice more easily than continuous water film flow. As a result, under conditions of a high rate of unfrozen water on the icing surface which was divided into both concurrent and counter-current flow, only a few frozen rivulets may be observed on the lee side of the cylinder, forming icing rings around it. This may have a significant influence on the changes in the local heat transfer coefficient and, thus, on the rate of icing.

### **7.3. Recommendations**

Several recommendations to be made apropos of this study may be formulated as follows:

1. In the vicinity of the supporting structure, where a high level of conductor twisting is prevented, the icing of power line conductors may be modeled with a great level of accuracy using a non-rotating cylinder model (Lozowski et al., 1979). The points that should be taken into account are: the method of time integration; the implicit presentation of water film flow, depending on the factors considered; and, particularly significant, modelling of pendant ice structures. To model latter effect properly, the model should be improved to include the third spatial dimension.
2. The applicability of the rotating cylinder model is limited by the following conditions: the cable to be modelled should be far away from the supporting structure, when conditions of high LWC (but not ultra-high) prevail for cables of relatively small diameter only. Once again, the importance of the incorporation of the third spatial dimension into the model should be emphasised here.
3. Under conditions of an overabundant liquid flux to the icing surface, both models overestimate or underestimate the natural experimentally obtained values. There is a probability that, a certain amount of modifications made to one of the models mentioned would be a liable alternative, as would a hybrid model incorporating features of both. Further attempts at satisfactory ice modelling in the domain of atmospheric icing would be most productive at this stage of research.

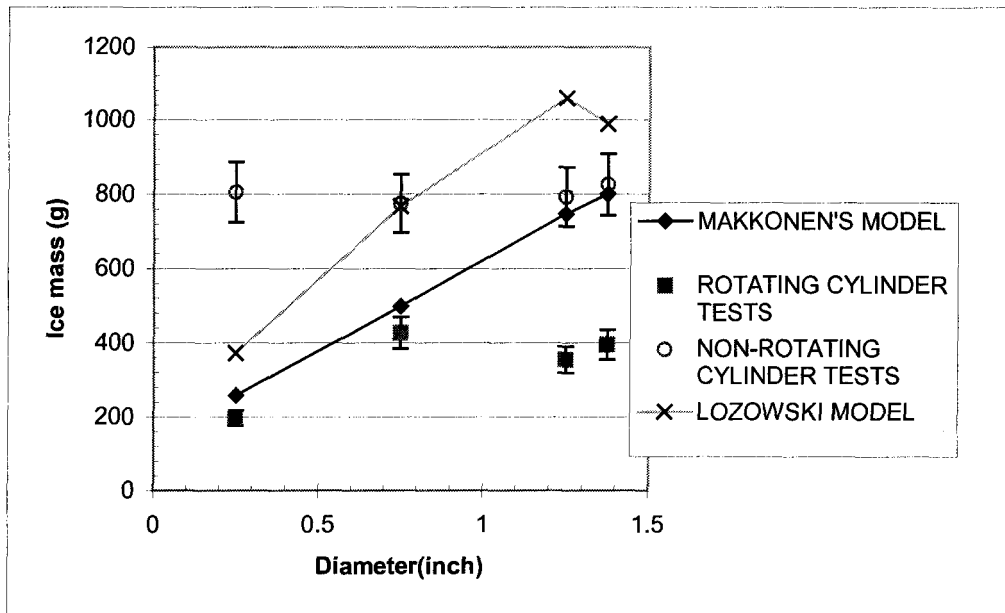


**Fig.7.1.** Comparison of rotating and non-rotating cylinder experiments in addition to the results the Makkonen model and the Lozowski at al. model (1979); ambient onditions: A-type DSD (MVD= 57  $\mu\text{m}$ ), air temperature is  $T_a = -5^\circ\text{C}$  and air speed  $V_a = 5 \text{ ms}^{-1}$ .

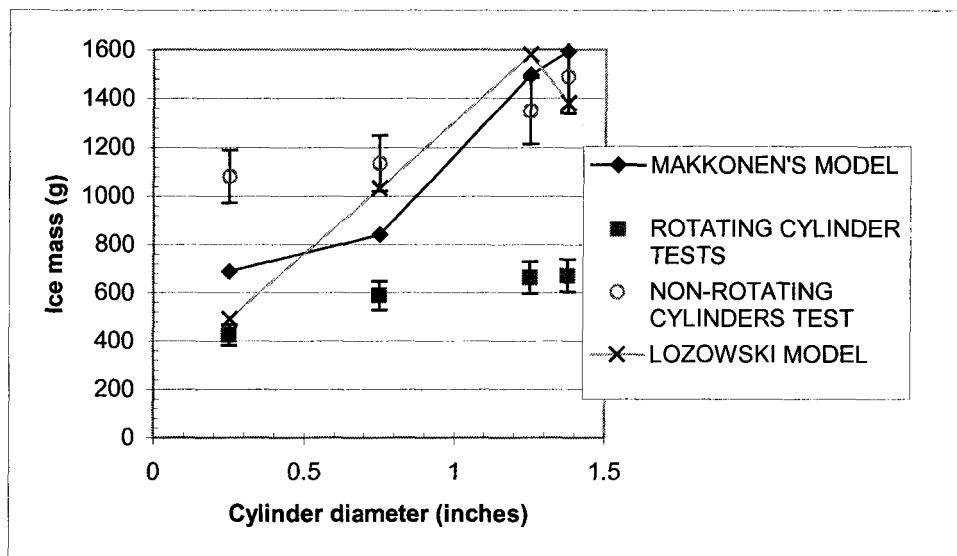


**Fig.7.2.** Comparison of rotating and non-rotating cylinder experiments in addition to the results the Makkonen model and the Lozowski at al. model; ambient conditions: A-type DSD (MVD= 57  $\mu\text{m}$ ), air temperature is  $T_a = -5^\circ\text{C}$  and air speed  $V_a = 10 \text{ ms}^{-1}$ .

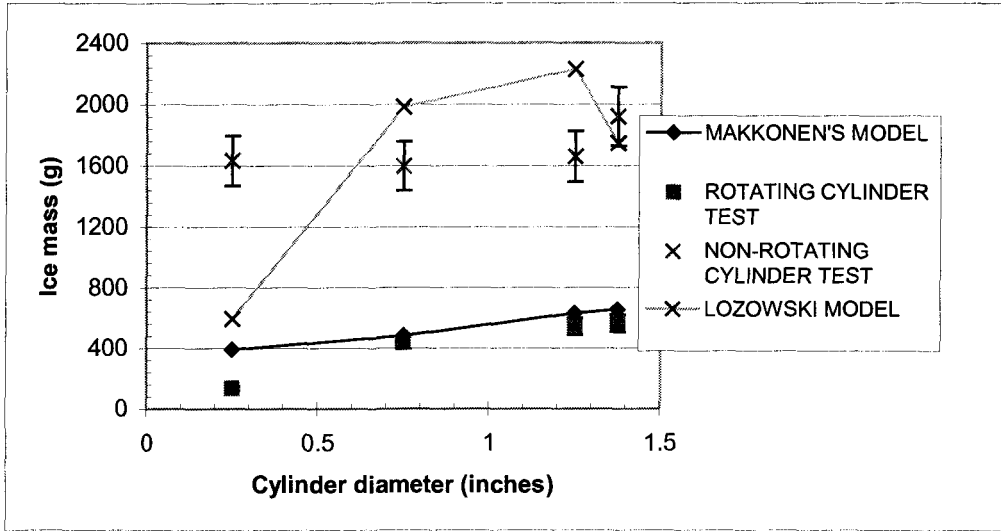


**Fig.7.3.** Comparison of rotating and non-rotating cylinder experiments in addition to the results the Makkonen model and the Lozowski at al. model; ambient conditions: A-type DSD (MVD= 57  $\mu\text{m}$ ), air temperature is  $T_a = -10^\circ\text{C}$  and air speed  $V_a = 5 \text{ ms}^{-1}$ .

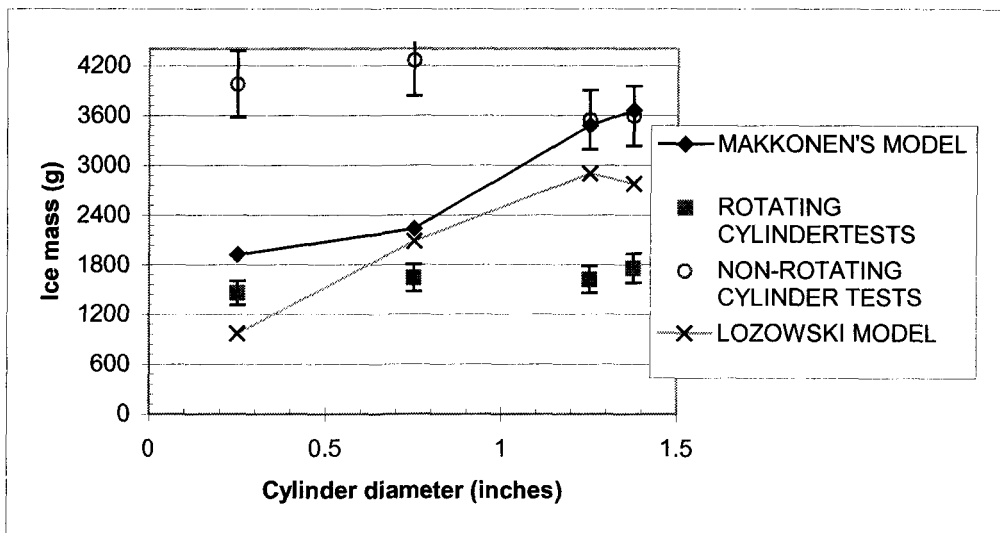


**Fig.7.4.** Comparison of rotating and non-rotating cylinder experiments in addition to the results the Makkonen model and the Lozowski at al. model; ambient conditions: A-type DSD (MVD= 57  $\mu\text{m}$ ), air temperature is  $T_a = -10^\circ\text{C}$  and air speed  $V_a = 10 \text{ ms}^{-1}$ .

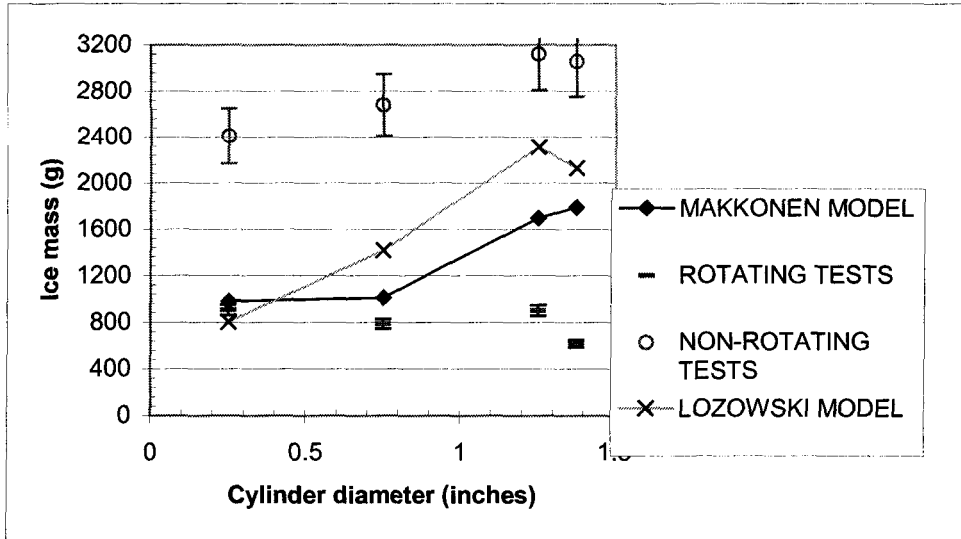


**Fig.7.5.** Comparison of rotating and non-rotating cylinder experiments in addition to the results the Makkonen model and the Lozowski at al. model; ambient conditions: B-type DSD (MVD= 42  $\mu\text{m}$ ), air temperature is  $T_a = -5^\circ\text{C}$  and air speed  $V_a = 5 \text{ ms}^{-1}$ .

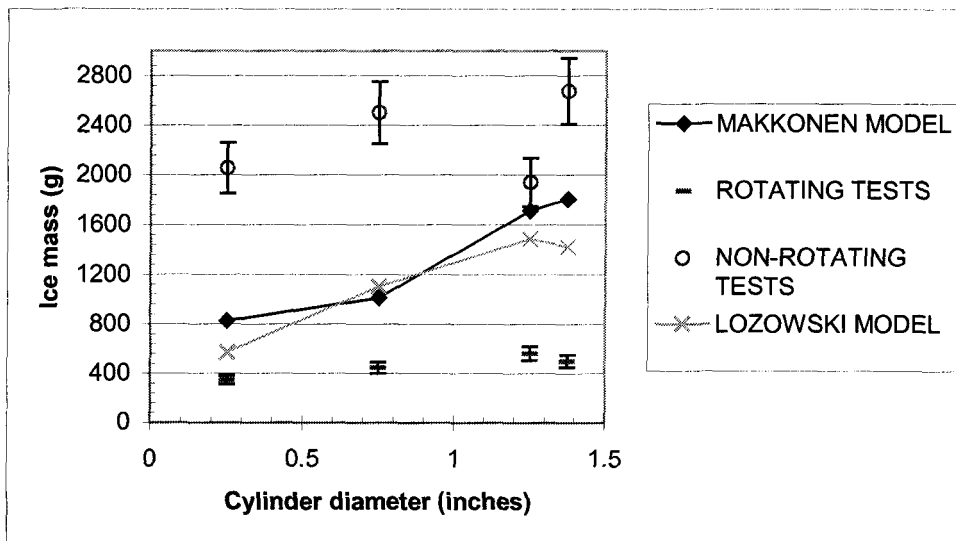


**Fig.7.6.** Comparison of rotating and non-rotating cylinder experiments in addition to the results the Makkonen model and the Lozowski at al. model; ambient conditions: B-type DSD (MVD= 42  $\mu\text{m}$ ), air temperature is  $T_a = -5^\circ\text{C}$  and air speed  $V_a = 10 \text{ ms}^{-1}$ .

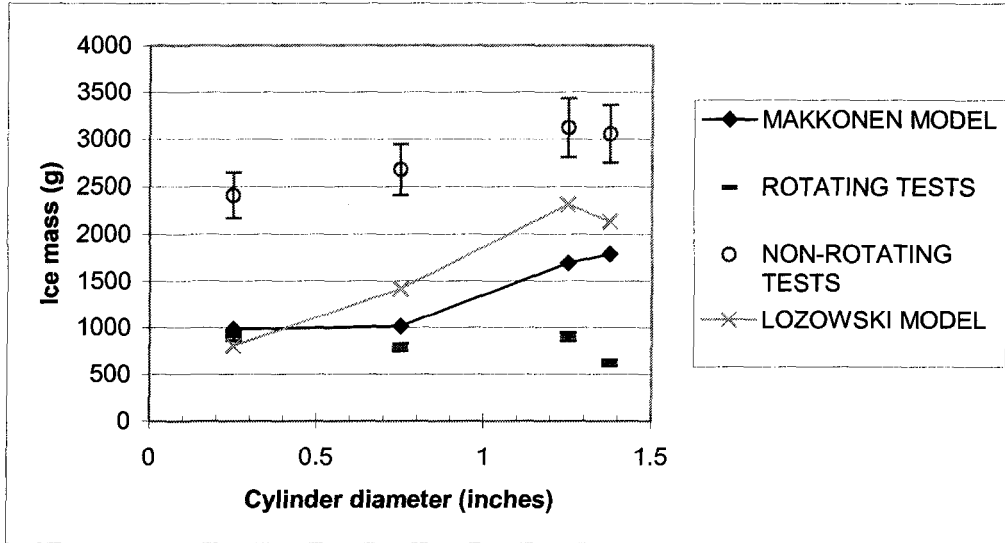


**Fig.7.7.** Comparison of rotating and non-rotating cylinder experiments in addition to the results the Makkonen model and the Lozowski at al. model; ambient conditions: B-type DSD (MVD= 57  $\mu\text{m}$ ), air temperature is  $T_a = -10^\circ\text{C}$  and air speed  $V_a = 5 \text{ ms}^{-1}$ .

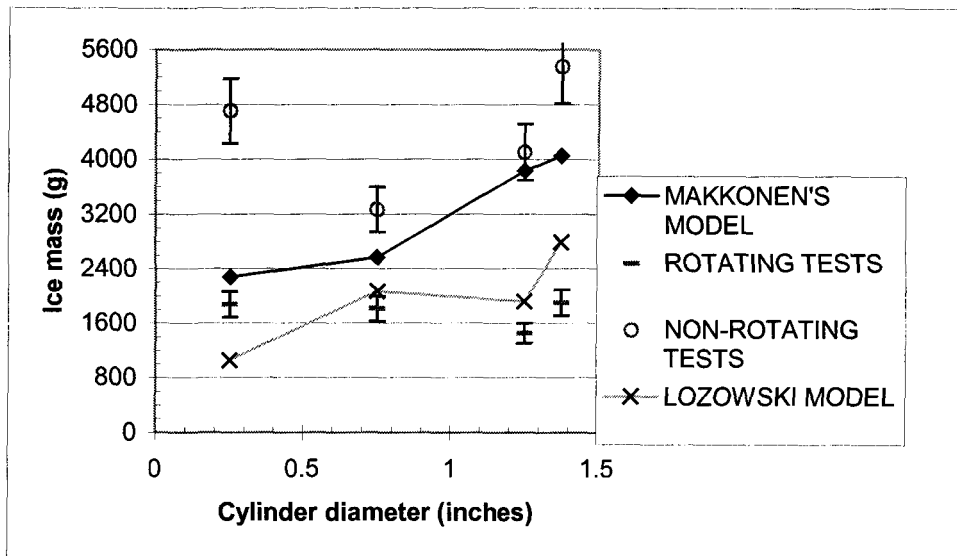


**Fig.7.8.** Comparison of rotating and non-rotating cylinder experiments in addition to the results the Makkonen model and the Lozowski at al. model; ambient conditions: B-type DSD (MVD= 42  $\mu\text{m}$ ), air temperature is  $T_a = -10^\circ\text{C}$  and air speed  $V_a = 10 \text{ ms}^{-1}$ .

## REFERENCES

- [1] **Achenbach, E.**, (1974): “ *Heat transfer from smooth and rough surfaced circular cylinders in a cross flow*”, Proceedings of the 5<sup>th</sup> International Heat Transfer Conference, Tokio, 229-233.
- [2] **Ackley, S. F., and Templeton, M. K.**, (1978): “*Numerical simulation of atmospheric ice accretion* ”, Paper presented at the 2nd International Symposium on Snow Removal and Ice Control Research, Hanover N. H., May 1978o 27 p.
- [3] **Bain, M., and Gayet, J. F.**, (1983) “, Contribution to the modelling of the ice accretion process: ice density variation with the impacted surface angle”, *Annals of Glaciology*, 4, 19-23.
- [4] **Brown, R. D., and Horjen, I.**, (1989): “*Evaluation of the state-of-the-art drilling platform icing models* “, Canadian Climate Centre Rep. No.89-10, 78p.
- [5] **Castellano, N. E., Nasello, O. B., and Levi, L.**, (2000): “*Study of hail density parameterisations*”, Proceedings of the 13<sup>th</sup> Int. Conf. On Clouds and Precipitation, Reno, Nevada USA,14-18 August 2000, V.2, 1081-1084.
- [6] **Châiné PM and Castonguay, G.**, (1974) “*New Approach to Radial Ice Thickness Concept Applied to Bundle-Like Conductors*”, Industrial Meteorology-Study IV, Environment Canada, Toronto, 11 pp.
- [7] **Chen H.C, and Ettema R.**, (1993). “*Atmospheric-ice loading of power transmission cables: laboratory experiments* ”, International Workshop on Atmospheric Icing of Structures, IWAIS (1993), Pages 412-416.
- [8] **Du N.-D.**, (1987) *Études des méthode par impact et à l’huile utilisées pour déterminer le diametre des gouttelettes dans les brouillards naturels et artificiels*”, M. Sc. Thesis, University of Quebec in Chicoutimi, December 1987.
- [9] **Finstad, Lozowski, Makkonen and Gates.**, (1988)*Journal of the Atmosheric Siences*, 45, 4008-4012.
- [10] **Godard, S.**, (1960) “ *Mesure des gouttelettes de nuage avec un film de collargol*”, *Bulletin de l’Observatoire du Puy de Dome*, n2, 41-45.

- [11] **Good Win, E.J. III, Mozer, J.D. AM. Digioia, Jr. and Power, B.A.,** “*Predicting Ice and Snow Loads For Transmission Lines*”, proceedings ”,First IWAIS, 1983, PP. 267-273.
- [12] **Ide, R. F.,** (1990) “*Liquid water content and droplet size calibration of the NASA LEWIS Icing Research Tunnel*”,ASA TM-102447
- [13] **Imai, I.,** (1953) “*Studies on Ice Accretion*”, Research on snow and Ice, No1., 1953, pp.34-44.
- [14] **Jones, KF.,** (1996), “*A Simple Model for Freezing Rain Ice Loads,*” Proc 7<sup>th</sup> International Workshop on Atmospheric Icing of Structures, Chicoutimi, QC, pp. 412-416.
- [15] **Karev, A. R., and Farzaneh, M.,:** “*Evolution of Droplet Size Distribution in an Icing Wind Tunnel*”, 10<sup>th</sup> IWAIS, Brno, Czech Republic, 2002.
- [16] **Karev, A.R., Farzaneh, M., and Mousavi, M.,**(2002) “*Influence of non-uniformity of droplet size distribution on an ice accretion* ” , 10<sup>th</sup> IWAIS, Brno, Czech Republic, 2002.
- [17] **Langmuir, I. P. and Blodgett, K. B.,** (1946): “*A mathematical investigation of water drop trajectories*”, AAF Technical Report No. 5418, 47 pp.
- [18] **Lenhard, R.W.,** “*An Indirect Method for Estimating the Weight of Glaze on Wires*”, Bull.Amer, Meteor. Soc.,Vol.36, 1995, PP.1-5.
- [19] **Lozowski, EP, Stallabrass, JR, and Hearty, PF.,** (1979): “*The icing of an unheated, non-rotating cylinder in liquid Water droplet – ice crystal clouds* “, National Research Council Canada,-Division of Mechanical Engineering, pp . 1-50
- [20] **Macklin W.C.,**(1962): “*The density and structure of ice formed by accretion,*” Quarterly Journal of the Royal Meteorological Society, 88, 1962, 30-50.

- [21] **Macklin, W.C, and Payne, G. S.,** (1967): “ *A theoretical study of the ice accretion process* ”, Quarterly Journal of the Royal Meteorological Society, 1993, Pages 195-213.
- [22] **Makkonen, L.,** (1996). “*Modelling Power Line Icing in Freezing Precipitation*”Proc 7<sup>th</sup> International Workshop on Atmospheric Icing of Structures, Chicoutimi, QC, pp. 195-200.
- [23] **Makkonen, L.,** (1984). “*Modelling of Ice Accretion on Wires,*” *J Clim. Appl. Meteorol.*, Vol 23, No 6, pp. 929-939.
- [24] **Makkonen, L.,** (1984): “ *Heat transfer of a rough cylinder*”, Cold Regions science and technology, Vol.8, 1984.
- [25] **Makkonen, L.,** (1986): “*The effect of conductor diameter on ice load as determined by a numerical model,*” In Proc.3<sup>rd</sup> Int. workshop on Atmospheric Icing of structures, pp. 81-89
- [26] **Makkonen, L.,** (1986): “*Modeling Power Line Icing In Freezing Precipitation,*” In Proc.7<sup>e</sup> Int. workshop on Atmospheric Icing of structures, pp. 81-89
- [27] **Messinger, B. L.,** (1953): “ *Equilibrium temperature of an unheated icing surface as a function of airspeed*”, Journal of the Aeronautical Sciences, 20, pp. 195- 200.
- [28] **Pellet, J.L. and A. S. Dennis.,** (1974): “*Effects of heat storage in hailstones*”, Preprints of the Conference on Cloud Physics, Tucson, pp. 63-66.
- [29] **Personne, P. and Gayet J.-F.,**(1988): “*Ice Accretion on Wires and Anti-Icing Induced by Joule Effect,*” *J. Appl. Meteorol.*, V.27, p.101-115
- [30] **Poots, G.,**(1996) ” *Ice and Snow Accretion on Structures,*” Research Studies Press LTD.
- [31] **Porcu,F. Smargiassi, E. and. Prodi., F.** “*2D and 3D Modelling of Ice Accretion on Wires*”, IWAIS 93, PP: 53-55.
- [32] **Rae, W. H. and Pope, A.,** (1984) “ *Low-speed tunnel testing*”, 2<sup>nd</sup> ed., New York, N.Y.: J. Wiley and Sons, 534p.

- [33] **Savadjiev, K, Farzaneh, M.,** (2001). “ *Study of icing and related metrological parameters distributions during atmosphere icing events* ”, Proceeding of the eleventh International and Polar Engineering Conference Stavanger, Norway (2001), V.1. p. 52-54
- [34] **Skelton, P.L.I, Poots, G.,** (1998). “ *Approximate predictions of ice accretion on an overhead transmission line which rotates with constant angular velocity.* IMA Journ. of App. Maths. 40, 23-45.
- [35] **Skelton ,P.L.I, Poots, G.,**(1998), “*The Icing Clock Model,*” Ice and Snow Accretion on Structures”, Wiley Inc, PP: 40-47.
- [36] **Stallabrass, J.R.,** (1978) “*An appraisal of the single rotating cylinder method of liquid water content measurement*”, National Research Council of Canada, Division of Mechanical Engineering, Rep.LTR-LT-92, Nov. 1978.
- [37] **Szilder, K, and Lozowski, EP,** (1995). “*Simulation of Icicle Growth Using a Three-Dimensional Random Walk Model,*” *Atmospheric Research*, Vol 36, No 1, pp. 243-249.
- [38] **Szilder, K, and Lozowski, EP.,** (1999). “*Morphogenetic Modelling of Wet Ice Accretions on Transmission Lines as a Result of Freezing Rain*”, Proc. 9<sup>th</sup> Int. Offshore Polar Engng. Conf., *ISOPE*, Brest, Vol II, pp. 616-621.
- [39] **Szilder, K., Lozowski, E.P., and Gates, E.M.,** (1988). “*Some Applications of a New Time-Dependent Cylinder Ice Accretion Model*”, *Atmospheric Research*, V.22, pp.41-59.
- [40] **Szilder, K., Lozowski, E.P., and Gates, E.M.,** (1987). “*Modelling Ice Accretion on Non-Rotating Cylinders –The Incorporation of Time Dependence and Internal Heat Conduction* ”, *Cold Regions Science and Technology* , V.13, 177-191.
- [41] **Talor, G.I**(1940). Notes on possible equipment and technique for experiments on icing aircraft, Aeronaut. Res.Comm.Rep.No.4350.
- [42] **Tribus, M.,** (1952): “*Modern icing technology. Lecture notes*”, Engineering Research Institute. University of Michigan.
- [43] **Zukauskas, A.,** (1972): “*Heat Transfer from tubes in cross -flow.* In: *Advances in Heat Transfer*, 8, 93-160.

# APPENDICES

## APPENDIX A

### COMPUTER PROGRAM FOR MAKKONEN MODEL

\*\*\*\*\*

\*\*\*\*\* The FORTRAN program of Makkonen's numerical  
model.

\*\*\*\*\*

\*\*\*\*\* Definition of the variables

\*

\* AT, accretion duration; d, droplet diameter; D0, the bare  
cylinder \*

\* diameter; Dc, the cylinder diameter in the each step of  
calculation; \*

\* DeltaT, time step; Dn, the cylinder diameter calculated in  
the \* \* each step; E, cylinder collection efficiency  
calculated as a \*

\* fractional sum of the collection efficiencies for each  
droplet \*

\* size category; EK0, name of the function; Em, collection  
\*

\* efficiency calculated using the median volume droplet; h,  
heat \*

\* transfer coefficient; I, icing intensity; K0, parameter to  
calculate \*

\* E; M, ice load; Mn, ice load in each step; n, freezing  
fraction; \*

\* PI,  $\pi$ ; R, Mackin's density parameter; R0, ice density;  
\*

\* ta, air temperature; TRO, total deposit density; v, wind velocity; \* \* w, liquid water content; Y, counter.

\*

\*\*\*\*\*

\*\*\*\*\*

```
DOUBLE PRECISION AT, d, D0, Dc, DeltaT, Dn, E, Em, h,
I, K0, M,
DOUBLE PRECISION Mn, N, PI, Pa, R, RO, ta, TRO, ts, v,
w, Y
PARAMETER (PI=3.1415926D0)
```

```
WRITE(*,*)'PLEASE INPUT THE AIR TEMPERATURE:'
READ*,ta
WRITE(*,*)'PLEASE INPUT THE WINDSPEED:'
READ*,v
WRITE(*,*)'PLEASE INPUT THE WATER CONTENT:'
READ*,w
WRITE(*,*)'PLEASE INPUT THE DROPLET DIAMETER:'
READ*,d
WRITE(*,*)'PLEASE INPUT THE CYLINDER DIAMETER:'
READ*,Dn
WRITE(*,*)'PLEASE INPUT THE AIR PRESSURE:'
READ*,Pa
WRITE(*,*)'PLEASE INPUT THE ACCRETION DURATION:'
READ*,AT
WRITE(*,*)'PLEASE INPUT THE TIME STEP:'
READ*,DeltaT
```

Mn=0.0D0

D0=Dn

```

OPEN (UNIT=2, FILE="RESULT")

DO 100, Y=0, AT, DeltaT
  M=Mn
  Dc=Dn
  K0=EK0 (v, d, Dc, ta, Pa)
  CALL EEM (K0, Em)
  CALL EQU (Em, E)
  h=EH (v, Dc, ta, Pa)
  CALL En (E, v, w, ta, Dc, h, Pa, n)
  CALL ETS (E, v, w, ta, h, Pa, ts)
  CALL ER (K0, d, ts, v, R)
  CALL ERO (R, RO)
  I=n*E*v*w/PI
  Mn=M+I*PI*Dc*DeltaT*36.0D2
  Dn=(4.0*(Mn-M)/(PI*RO)+Dc**2)**(1.0/2.0)
  TRO=4.0*Mn*(PI*Dn**2-PI*D0**2)**-1
  WRITE (2, 200) Y, Dc*1.0D2, I*2.0d4, RO, M, TRO, n, E
10  FORMAT(1x, f8.2, 2x, f8.4, 2x, f8.4, 2x, f8.4, 2x, f8.4,
  2x,
  & f8.4, 2x, f8.4, 2x, f8.4, 2x, f8.4)
10  CONTINUE

CLOSE(unit = 2)
STOP
END

```

```

*****
*****
*****          Function to calculate the parameter
K0          *

```

```

*****
*****

```

```

DOUBLE PRECISION FUNCTION EK0(v,d,Dc,ta,Pa)
IMPLICIT NONE
DOUBLE PRECISION Row, X, Roa, K, Red, v, Dc, d, ta,
MU,
& a,b,MU0,Pa
Row=1.0D3
X=MU(ta)
mu0=1.8325D-5
Roa=Pa/(287.05*(ta+273.15))
K=(Row*v*d**2.0)/(9.0*x*Dc)
Red=Roa*d*v/x
EK0=K*(0.087*Red**(0.76*Red**-0.027)+1)**-1
RETURN
END

```

```

*****
*****
Function to calculate the absolute
viscosity of air          *
*                          as a function of temperature
*
*****
*****

```

```

DOUBLE PRECISION FUNCTION MU(T)
IMPLICIT NONE
DOUBLE PRECISION MU0,t0,C,T
MU0=1.8325D-5
t0 = 296.16D0

```

C = 120.0D0

MU=MU0\*((t0+C)/(T+273.15+C))\*((T+273.15)/t0)\*\*(3.0/2.0)

RETURN

END

```
*****
*****          Subroutine   to   calculate   collection
efficiency          *
*          calculated using the median volume droplet Em
          *
*****
*****
```

SUBROUTINE EEM(K,Em)

IMPLICIT NONE

DOUBLE PRECISION Em, K, ESE, EGE

IF (K.GT.0.8) THEN

Em = K\*\*1.1\*(K\*\*1.1+1.426)\*\*-1

ELSE

Em = 0.5\*(DLOG10(8.0\*K))\*\*1.6

END IF

RETURN

END

```
*****
*****
*          Subroutine to calculate collection efficiency E
with Em   *
```

```
*****
*****
```

```
      SUBROUTINE EQU (Em, E)
      DOUBLE PRECISION Em, E
      E=0.69*EM**0.67+0.31*EM**1.67
      END
```

```
*****
*****          Function to calculate convective heat
transfer coefficient h      *
*****
*****
```

```
      DOUBLE PRECISION FUNCTION EH(v, Dc, ta, Pa)
      DOUBLE PRECISION v, Dc, ta, Ka, Roa, a, x, mu, Pa
      Roa=Pa/(287.05*(ta+273.15))
      Ka=2.53D-2
      X=MU(ta)
      EH=Ka*0.032*(Roa*Dc*v/X)**0.85/Dc
      END
```

```
*****
*****          Subroutine to calculate the freezing
fraction n                  *
*****
*****
```

```
      SUBROUTINE En(E, v, w, ta, Dc, h, Pa, n)
      IMPLICIT NONE
```

```

DOUBLE PRECISION PI,SBC,Cw,Ci,k,Le,a,Lf,Cp,Pa,r,t1,t2,
& w,h,ea,Dc,n, e0,ts,ta,E,v,c,b,x,y,z
PI=3.1415926D0
Lf=0.3337D6
k=0.62D0
Le=2.5008D6
Cp=1005D0
r=0.79D0
Cw=4218D0
SBC=5.6697D-8
a=8.1D7
CALL EVP(0.0,e0)
CALL EVP(ta,ea)
n=PI*h*(-ta+k*Le*(e0-ea)/(Cp*Pa)-r*v**2.0/(2.0*Cp))/
& (2.0*E*v*w*Lf)-ta/Lf*(Cw+PI*SBC*a/(2.0*E*v*w))
IF (n.GT.1) THEN
n=1
END IF
RETURN
END

```

```

*****
*****
*      Subroutine to calculate the saturation water vapour
pressure  *
*****
*****

```

```

SUBROUTINE EVP(T,E)

```

```

DOUBLE PRECISION T,E
E=0.6112*DEXP(17.67*T/(T+243.5))*1.0D3
RETURN
END

```

```

*****
*****
*   Subroutine to calculate the ice accretion surface
temperature ts *
*****
*****

```

```

SUBROUTINE ETS(E,v,w,ta,h,Pa,ts)
  IMPLICIT NONE
  DOUBLE PRECISION F,F1,F2,PI,SBC,Lf,Cw,Ci,k,ls,Cp,Pa,r,
& E,v,w,h,ea,t1,t2,ts,ta,a,EF,t
  EF(t)=2*E*v*w*(Lf + Cw*ta - Ci*t)/PI - h*((t - ta)
& +k*ls*(0.6112*DEXP(17.67*t/(t+243.5))*1.0D3-ea)/
& (Cp*Pa)-r*v**2/(2*Cp))-SBC*a*(t-ta)
  PI=3.1415926D0
  SBC=5.6697D-8
  Lf=0.3337D6
  Cw=4218D0
  Ci=2106D0
  k=0.62D0
  ls=2.8366D6
  Cp=1005D0
  r=0.79D0
  a=8.1D7
  CALL EVP(ta,ea)
  t1=-40.0D0

```

```

t2=10.0D0
F1=EF(t1)
F2=EF(t2)
10  ts = (t1 + t2)/2.0
    F=EF(ts)
    IF (SIGN(F,F1).EQ.F) THEN
        t1=ts
        F1=F
    END IF
    IF(SIGN(F,F2).EQ.F) THEN
        t2=ts
        F2=F
    END IF
    IF((ABS(t1-t2).GT.1D-10).OR.(F.GT.1D-12))GOTO 10
    IF(F.GT.1D-12) ts=(t1+t2)/2.0
    RETURN
END

```

```

*****
*****          Subroutine to calculate Macklin's
density parameter  *
*****
*****

```

```

SUBROUTINE ER(K0, dm, ts, v, R)
IMPLICIT NONE
DOUBLE PRECISION K0, R, dm, ts, v, v0
IF (K0.LE.0.55) THEN
    v0=v*(-0.174+1.464*K0-0.816*K0**2)
ELSE
    v0=v*(0.561+0.592*DLOG10(K0)-0.26*(DLOG10(K0))**2)

```

```

END IF
IF ((ts.gt.0.0d0).or.(abs(ts).lt.1.0D-8)) THEN
  R=70.0D0
ELSE
  R=-v0*dm*1.0D6/(2.0*ts)
END IF
RETURN
END

```

```

*****
***** Subroutine to calculate ice density
*****
*****

```

```

SUBROUTINE ERO(R,RO)
DOUBLE PRECISION R,RO
IF (R.LT.0.9) THEN
  RO = 100D0
ELSE IF (R.LE.10.0) THEN
  RO = 0.11 * R**0.76*1.0D3
ELSE IF (R.LE.60.0) THEN
  RO=(R*(R+5.61)**-1)*1.0D3
ELSE
  RO=0.92D3
ENDIF
RETURN
END

```

## APPENDIX B

```
*****
The Computer program for Lozowski (1974) Model
*****
10    DIMENSION A(25),B(25), E(25),T(25)
      REAL K0,FNE,FNP,L,L9,K,K1,K2,L1,L2,M,M1,N,N1, MVD, KRO
20
WRITE(*,*)'*****
***'
30    WRITE(*,*)'ICING OF A CIRCULAR CYLINDER IN MIXED
CONDITIONS OF '
40    WRITE(*,*)'SUPERCOOLED WATER AND ICE CRYSTALS USING
ENGLISH/ '
50    WRITE(*,*)'CANSDALE STICKING ASSUMPTIONS FOR ICE AND
ALLOWING '
55    WRITE(*,*)'FOR RUNBACK
'
60
WRITE(*,*)'*****
***'
C
*****
*****
C    * SATURATION VAPOR PRESSURE AND ITS TEMPERATURE
DERIVATIVE
C
*****
**
C120  FUNCTION FNE=((2.59E-04*X+2.7487E-
2)*X+1.4472)*X+4.426E+1)*X
C    1+609.92
C130  FUNCTION FNP=((1.036E-03*X+8.2461E-2)*X+2.8944)*X+44.26
C
*****
*****
C    *                               INPUT VARIABLES FROM KEYBOARD
*
C
*****
*****

OPEN(UNIT=15, FILE='EDMONTON4.DAT', STATUS='NEW', FORM='FORMATT
ED')
C
OPEN(UNIT=16, FILE='EDMO4.DAT', STATUS='NEW', FORM='FORMATTED')
```

```

c190  WRITE(*,*) 'SIX DIGIT DATE:DAY, MONTH, YEAR'
c200  READ(*,*) D7, D8, D9
c210  WRITE(15,220) D7, D8, D9
c220  FORMAT (3F3.0)

      WRITE(*,*) 'AIR TEMPERATURE(DEGREES C) '
      READ(*,*) T2
c      T2=-21
      WRITE(*,*) 'AIR TEMPERATURE=', T2, 'DEG C'
      WRITE(15,*) 'AIR TEMPERATURE=', T2, 'DEG C'

c      WRITE(*,*) 'AIR RELATIVE HUMIDITY(PART OF UNITY) '
c      READ(*,*) FA
      FA=0.85
      FAP=FA*100
      WRITE(*,*) 'AIR RELATIVE HUMIDITY =', FAP, '%'
      WRITE(15,*) 'AIR RELATIVE HUMIDITY =', FAP, '%'

300  WRITE(*,*) 'LIQUID WATER CONTENT KG/CUBIC M'
      READ(*,*) L
      WRITE(*,*) 'LIQUID WATER CONTENT=', L, 'KG/CUBIC M'
      WRITE(15,*) 'LIQUID WATER CONTENT=', L, 'KG/CUBIC M'

c      WRITE(*,*) 'ICE CRYSTAL CONTENT KG/CUBIC M'
c      READ(*,*) L9
      L9=0
      WRITE(*,*) 'ICE CRYSTAL CONTENT=', L9, 'KG/CUBIC M'
      WRITE(15,*) 'ICE CRYSTAL CONTENT=', L9, 'KG/CUBIC M'

c      WRITE(*,*) 'MVD DIAMETER(MICRONS) '
c      READ(*,*) MVD
c      WRITE(*,*) 'MVD =', MVD, 'MICRONS'
c      WRITE(2,*) 'MVD =', MVD, 'MICRONS'

400  WRITE(*,*) 'TYPE OF DISTRIBUTION: 1-A CENTRE,2-A LEFT,
3-A RIGHT'
      WRITE(*,*) '4- B CENTRE, 5- B LEFT, 6- B RIGHT'
      READ(*,*) ITYPE
      WRITE(*,*) 'ITYPE =', ITYPE
      WRITE(15,*) 'ITYPE =', ITYPE

c      WRITE(*,*) 'CYLINDER DIAMETER (METERS) '
c      READ(*,*) D
      D=3.81E-2

```

```

WRITE(*,*) 'CYLINDER DIAMETER=',D,' METERS '
WRITE(15,*) 'CYLINDER DIAMETER=',D,' METERS '

WRITE(*,*) 'AIRSPEED (M/S) :LOW,HIGH, INTERVAL '
READ(*,*) V1,V2,V3
WRITE(*,*) 'ROUGHNESS:SMOOTH=0,ROUGH=1 '
READ(*,*) R7
IF (R7.EQ.1) GO TO 540
WRITE(*,*) 'SMOOTH SURFACE HEAT TRANSFER ASSUMED'
WRITE(15,*) 'SMOOTH SURFACE HEAT TRANSFER ASSUMED'
530 GO TO 570
540 WRITE(*,*) 'ROUGH SURFACE HEAT TRANSFER ASSUMED'
WRITE(15,*) 'ROUGH SURFACE HEAT TRANSFER ASSUMED'
570 WRITE(*,*)
C
*****
**
C      *DEFINE QUASI-PERMANENT VARIABLES VIA PROGRAM
      STATEMENTS      *
C
*****
**
C
*****
**
C      *DROPLET DIAM SPECTRUM PERCENT VOLUME AT
      5,10,...125MICRONS      *
C
*****
**
580  IF (ITYPE .NE. 1) GO TO 590
      DATA A(1)/9.52E-
5/,A(2)/0.1323/,A(3)/1.8199/,A(4)/3.4598/,
      1A(5)/4.6132/,A(6)/6.0162/,A(7)/6.5855/,A(8)/6.1021/,A(
9)/6.779/,
      1A(10)/5.5479/,A(11)/3.5251/,A(12)/6.9468/,
A(13)/5.204/,

1A(14)/0.9365/,A(15)/6.9625/,A(16)/7.0872/,A(17)/5.1296/,
      1A(18)/8.1599/,A(19)/7.2301/,A(20)/2.8224/,A(21)/0/,
      1A(22)/0/,A(23)/0/,A(24)/4.9399/, A(25)/0/
      MVD=56
      GO TO 970
C      DATA
A(1)/6/,A(2)/10/,A(3)/19/,A(4)/29/,A(5)/18/,A(6)/8/,
C      1A(7)/5/,A(8)/3.5/,A(9)/1.5/

```

```

590  IF (ITYPE .NE. 2) GO TO 600
      DATA A(1)/0/,A(2)/0.0398/,A(3)/0.9067/,A(4)/2.5993/,
      1A(5)/2.644/,A(6)/2.9435/,A(7)/3.3039/,A(8)/4.5778/,A(9
) /5.505/,
      1A(10)/8.2923/,A(11)/9.5577/,A(12)/8.6104/,
A(13)/11.0576/,

1A(14)/8.1255/,A(15)/4.3149/,A(16)/4.3922/,A(17)/6.358/,
      1A(18)/5.057/,A(19)/1.4936/,A(20)/0/,A(21)/4.0645/,
      1A(22)/0/,A(23)/2.687/,A(24)/0/, A(25)/3.4691/
      MVD=58
      GO TO 970
600  IF (ITYPE .NE. 3) GO TO 610
      DATA A(1)/0/,A(2)/0.0892/,A(3)/1.2487/,A(4)/1.2919/,
      1A(5)/1.7111/,A(6)/1.2351/,A(7)/2.5185/,A(8)/2.9477/,A(
9) /3.6205/,
      1A(10)/9.3603/,A(11)/8.5941/,A(12)/10.9587/,
A(13)/12.3674/,

1A(14)/12.3561/,A(15)/8.6536/,A(16)/7.3179/,A(17)/3.9234/,
      1A(18)/3.5106/,A(19)/8.295/,A(20)/0/,A(21)/0/,
      1A(22)/0/,A(23)/0/,A(24)/0/, A(25)/0/
      MVD=60
      GO TO 970
610  IF (ITYPE .NE. 4) GO TO 620
      DATA A(1)/5.31E-
4/,A(2)/0.4171/,A(3)/1.7248/,A(4)/2.3058/,
      1A(5)/3.2241/,A(6)/6.5143/,A(7)/10.2346/,A(8)/13.9311/,

1A(9)/12.4575/,A(10)/14.5606/,A(11)/12.0142/,A(12)/10.0444/,

1A(13)/1.8427/,A(14)/4.6426/,A(15)/1.4382/,A(16)/0/,A(17)/2.
1191/,
      1A(18)/2.5282/,A(19)/0/,A(20)/0/,A(21)/0/,
      1A(22)/0/,A(23)/0/,A(24)/0/, A(25)/0/
      MVD=42
      GO TO 970
620  IF (ITYPE .NE. 5) GO TO 630
      DATA A(1)/0/,A(2)/0.0904/,A(3)/1.6388/,A(4)/2.9182/,
      1A(5)/4.9143/,A(6)/5.0741/,A(7)/9.0905/,A(8)/8.9437/,A(
9) /8.4512/,
      1A(10)/12.4364/,A(11)/8.1805/,A(12)/13.0101/,
A(13)/3.6321/,
      1A(14)/5.4905/,A(15)/5.6694/,A(16)/2.77/,A(17)/3.3415/,
      1A(18)/1.9933/,A(19)/2.3549/,A(20)/0/,A(21)/0/,

```

```

1A(22)/0/,A(23)/0/,A(24)/0/, A(25)/0/
MVD=46
GO TO 970

630  IF (ITYPE .NE. 6) GO TO 400
      DATA A(1)/8.831E-
5/,A(2)/0.1597/,A(3)/1.4678/,A(4)/1.9986/,
      1A(5)/2.9284/,A(6)/5.3466/,A(7)/9.2133/,A(8)/11.9186/,

1A(9)/12.145/,A(10)/13.0194/,A(11)/9.4026/,A(12)/7.5192/,

1A(13)/6.2076/,A(14)/6.0821/,A(15)/2.1532/,A(16)/2.6301/,A(1
7)/0/,
      1A(18)/3.7853/,A(19)/0/,A(20)/0/,A(21)/0/,
      1A(22)/0/,A(23)/4.0225/,A(24)/0/, A(25)/0/
MVD=44
970  CONTINUE
      WRITE(*,*) 'DROPLET SPECTRUM PARAMETERS -PERCENT VOLUME
AT GIVEN
      1DIAMETER'

      WRITE(*,*) 'CENTRE 5MU 10MU 15MU 20MU 25MU 30MU 35MU
40MU125MU'
      WRITE(15,*) 'A(1)=' ,A(1) , 'A(2)=' ,A(2) , 'A(3)=' ,A(3) , 'A(4)
=' ,A(4) ,
      1'A(5)=' ,A(5) , 'A(6)=' ,A(6) , 'A(7)=' ,A(7) , 'A(8)=' ,A(8) , 'A
(9)=' ,A(9) ,
      1'A(10)=' ,A(10) , 'A(11)=' ,A(11) , 'A(12)=' ,A(12) , 'A(13)=' ,
A(13) ,

1'A(14)=' ,A(14) , 'A(15)=' ,A(15) , 'A(16)=' ,A(16) , 'A(17)=' ,A(17)
,

1'A(18)=' ,A(18) , 'A(19)=' ,A(19) , 'A(20)=' ,A(20) , 'A(21)=' ,A(21)
,

1'A(22)=' ,A(22) , 'A(23)=' ,A(23) , 'A(24)=' ,A(24) , 'A(25)=' ,A(25)
C
*****
*****
C      *          STATIC PRESSURE IN PASCALS
*
C
*****
*****

P=1E+5

```

```
DO 3420 V=V1,V2,V3
WRITE(15,*) 'FREE STREM VELOCITY=',V,'M/S'
```

```
WRITE(15,*) '*****'
*****'
```

```
C
*****
*****
```

```
C      *          DEFINE CONSTANTS
```

```
*
C
*****
*****
```

```
      P1=0.711
      S=0.595
      L2=2.5E+06
      C1=1.005E+03
      E1=0.622
      C2=4.27E+03
      C3=2.07E+03
      R3=287.04
      R4=918
      R9=1E+03
      PI=3.14
```

```
C
*****
*****
```

```
C      *          CALCULATE FUNCTIONS OF AIR TEMPERATURE
```

```
*
C
*****
*****
```

```
      R0=P/(R3*(T2+273.16))
      M=1.718E-05+5.1E-08*T2
      K=2.43E-02+7.3E-05*T2
```

```
C
*****
*****
```

```
C      *          CALCULATE FUNCTIONS OF VELOCITY
```

```
*
```

```

C
*****
*****

      R2=V*D*R0/M
      Z8=V*R0/M
      Z9=R9*V/(9*M*D)

C
*****
*****

C      *          CALCULATE LOCAL COLLECTION EFFICIENCY,
TOTAL      *
C      *          COLLECTION EFFICIENCY, MAXIMUM
INPINGEMENT ANGLE      *
C
*****
*****

      DO 1440 J=1,25
      D2=J*5E-06
      R8=Z8*D2
      K1=Z9*D2**2

      S1=1/(1+0.0967*R8**0.6367)
      K0=(K1-0.125)*S1+0.125
      IF (K0 .LT. 0.125) GO TO 1410
      B(J)=1.4*(K0-0.125)**0.84
      B(J)=B(J)/(1+B(J))
      E(J)=0.489*(LOG(8*K0))**1.978
      T(J)=ATAN(1.7*(K0-0.125)**0.76)
      IF (K0 .LT. 0.9) GO TO 1440
      E(J)=K0/(K0+PI/2)
      IF (K0 .LT. 7.5) GO TO 1440
      B(J)=K0/(K0+1)
      IF (K0.LT.10) GO TO 1440
      T(J)=ATAN(K0)
      GO TO 1440
1410  E(J)=0
      B(J)=0
      T(J)=1E-10
1440  CONTINUE
      pich=pi/36

C
*****
*****

```

```

C      *          CALCULATE FUNCTIONS OG ANGLE AROUND CYLINDER
*
C
*****
***
      piz=pi/2
      WRITE(15,*) ' TH          N1          TS          RW          BETA
F
1      W0          Q1          Q2          Q3          Y3          Q4
Q5
1 U1  U3          N  H          R1          FUN1  FUN2          FUND
1 P  T10'
      WRITE(16,*) 'I, J,A(J),B(J),E(J), G9, T(J)  T4'
      I=0

      DO 3390  T4=0,PIZ,PICH
      I=I+1
      IF (R7.EQ.1) GO TO 1540
      N=SQRT(R2*(1-(2*T4/PI)**3))
      GO TO 1550
1540  N=SQRT(R2*(2.4+1.2*SIN(3.6*(T4-25*PI/180))))
1550  H=N*K/D
      R1=0.75+0.25*COS(2*T4)
      S3=0
      DO 1630 J=1,25
      IF(T(J) .LT. T4) GO TO 1630
      G9=B(J)*COS(PI*T4/(2*T(J)))
      G9=G9+(PI**3/(T(J)**3*(PI**2-4)))*(E(J)-
2*T(J)*B(J)/PI)*
      1T4**2*SIN(PI*T4/T(J))
      S3=S3+G9*A(J)/100

c1632      WRITE(16,1637)I,J,A(J),B(J),E(J),G9,T(J),T4, S3
c1637
FORMAT(I5,2X,I5,2X,E10.3,2X,E10.3,2X,E10.3,2X,E10.3,2X,E10.3
,
c      12X,E10.3,2X,E10.3)
1630  CONTINUE

c1640  *****

C
*****
***
C      *          LOCAL COLLECTION EFFICIENCY
*

```

```
C
*****
***
```

```
      B1=S3
      B2=COS (T4)
```

```
C
*****
***
```

```
C      *           IMPINGING WATER AND ICE FLUXES
```

```
*
```

```
C
*****
***
```

```
      R=B1*L*V
      R6=B2*L9*V
```

```
C
*****
***
```

```
C      *CALCULATE LOCAL STATIC PRESSURE FOR EVAPORATIVE
COOLING TERM *
```

```
C
*****
***
```

```
      P=P+(1.3*COS(2*T4)-0.3)*R0*V**2/2
      IF (T4 .EQ. 0)GO TO 1920
      U1=U3
      U2=U4
      T7=T0
      GO TO 2040
1920  U1=0
      U2=0
      T7=0
```

```
C
*****
***
```

```
C      *   ITERATIVE SOLUTION OF THE HEAT BALANCE EQUATION
```

```
*
```

```
C
*****
***
```

```

C
*****
***
C      *   CALCULATE FUNCTIONS OF SURFACE TEMPERATURE
*
C
*****
***

2040  T1=0
2050  T10=T2-T1
      L1=3.34E+05+(C2-C3)*T1

C
*****
***
C      *   CALCULATE HEAT TRANSFER TERMS
*
C
*****
***
      FUN1=FNE(T2)
      FUN2=FNE(T1)
      FUND=FUN1-FA*FUN2
      Q1=H*T10
      Q2=(FUND)*H*L2*E1*(P1/S)**0.63/(C1*P)
      Q3=R*C2*T10
      Q5=H*R1*V**2/(2*C1)
      Q6=R*V**2/2
      Q7=R6*V**2/2
      Y1=U1*C2*(T7-T1)
      Y2=U2*C3*(T7-T1)

C
*****
***
C      *           TEST FOR NO SPRAY
*
C
*****
***

      IF(R .EQ. 0) GO TO 2270
      GO TO 2330
2270  IF(U1 .EQ. 0) GO TO 2290
      GO TO 2330
2290  K2=0
      M1=0

```

```

F1=0
GO TO 2770
2330 IF (T1 .LT. 0) GO TO 2740
2340 IF (T1 .GT. 0) GO TO 3150
K2=1
M1=0
Q8=K2*R6*C3*T10
Q9=-K2*M1*R6*L1
Y4=-M1*U2*L1
F1=- (Q1+Q2+Q3+Q5+Q6+Q7+Q8+Q9+Y1+Y2+Y4) / (L1*(R+U1))
IF(F1 .GT. 1) GO TO 2510
IF(F1 .LT. 0) GO TO 2900

```

```

C
*****
***
C      *      THERMODYNAMIC ZONE 3
*
C
*****
***

```

```

Q4=F1*R*L1
Y3=F1*U1*L1
GO TO 3190
2510 IF(R6 .EQ. 0) GO TO 2740
F1=1
Q4=F1*R*L1
Y3=F1*U1*L1
K2=- (Q1+Q2+Q3+Q4+Q5+Q6+Q7+Y1+Y2+Y3+Y4) / (R6*C3*T10-
M1*R6*L1)
IF (K2 .LT. 0) GO TO 2740
IF (K2 .GT. 1) GO TO 2590
GO TO 2660
2590 WRITE (*,*) 'ERROR: K EXCEEDS 1, PROGRAM STOPPED'
GO TO 3430

```

```

C
*****
***
C      *      THERMODYNAMIC ZONE 2
*
C
*****
***

```

```

2660 Q8=K2*R6*C3*T10

```

Q9=-K2\*M1\*R6\*L1  
GO TO 3190

C  
\*\*\*\*\*  
\*\*\*  
C \* THERMODYNAMIC ZONE 1  
\*  
C  
\*\*\*\*\*  
\*\*\*

2740 F1=1  
K2=0  
M1=0  
2770 Q4=F1\*R\*L1  
Q8=K2\*R6\*C3\*T10  
Q9=-K2\*M1\*R6\*L1  
Y3=F1\*U1\*L1  
Y4=-M1\*U2\*L1  
P9=Q1+Q2+Q3+Q4+Q5+Q6+Q7+Q8+Q9+Y1+Y2+Y3+Y4  
P8=-H-H\*L2\*E1\*(P1/S)\*\*0.63\*FNP(T1)/(C1\*P)-R\*C2-K2\*R6\*C3  
P8=P8-K2\*M1\*R6\*(C2-C3)+F1\*R\*(C2-C3)-U1\*C2+F1\*U1\*(C2-C3)  
P8=P8-U2\*C3-M1\*U2\*(C2-C3)  
T9=-P9/P8  
IF(ABS(T9).LT. 0.01) GO TO 3190  
T1=T1+T9  
GO TO 2050  
2900 IF(R6 .EQ. 0) GO TO 2920  
2910 GO TO 2930  
2920 IF(U2 .EQ. 0) GO TO 3150  
2930 F1=0  
Q4=F1\*R\*L1  
Y3=F1\*U1\*L1  
M1=(Q1+Q2+Q3+Q4+Q5+Q6+Q7+Q8+Y1+Y2+Y3)/((K2\*R6+U2)\*L1)  
IF(M1 .GT. 1) GO TO 3150  
IF(M1 .LT. 0) GO TO 3000  
GO TO 3070  
3000 WRITE(\*,\*)'ERROR: M IS NEGATIVE, PROGRAM STOPPED'  
GO TO 3430

C  
\*\*\*\*\*  
\*\*\*  
C \* THERMODYNAMIC ZONE 4  
\*

```

C
*****
***

3070  Q9=-M1*K2*R6*L1
      Y4=-M1*U2*L1
      GO TO 3190

```

```

C
*****
***

```

```

C      *      THERMODYNAMIC ZONE 5
*

```

```

C
*****
***

```

```

3150  F1=0
      K2=1
      M1=1
      GO TO 2770
3190  U3=(1-F1)*(R+U1)+M1*(K2*R6+U2)
      U4=(1-F1)*(1-M1)*(K2*R6+U2)
      T0=T1
      R5=F1*(R+U1+(1-M1)*(K2*R6+U2))
      W0=K2*R6+R+U1+U2
      IF(W0 .EQ. 0) GO TO 3270
      N1=R5/W0
      GO TO 3330
3270  N1=0

```

```

C
*****
***

```

```

C      *      OUTPUT PARAMETERS AND RESULTS
*

```

```

C
*****
***

```

```

3330  T5=T4*180/PI

      KRO=Z9*(MVD*1E-6)**2
      IF (T1. EQ.0) GO TO 3335
      XMAC=ABS(MVD*V/(2*T1))
      IF (KRO .GT. 4) GO TO 3331
      ROIM=917*(1-EXP(-(0.096*XMAC)**0.85))

```

```

        ROII=917-800*EXP(-(0.27*XMAC)**1.23)
        GO TO 3336
3331  ROIM=917-813*EXP(-(0.138*XMAC)**0.78)
        ROII=917-854*EXP(-(0.104*XMAC)**0.78)
        GO TO 3336
3335  ROIM=917
        ROII=917
3336  CONTINUE

WRITE(15,3350)T5,N1,T1,ROIM,ROII,R5,B1,F1,W0,Q1,Q2,Q3,Y3,Q4,
Q5,U1,
        1U3,N,H,FUN1,FUN2,P,T10
C      WRITE(15,3352)N,H,FUN1,FUN2,P,T10
3350
FORMAT(F4.0,3X,F6.3,3X,F6.2,3X,E10.3,3X,E10.3,3X,F6.4,3X,F6.
4,3X,
        1F6.4,

13X,E10.4,3X,E10.4,3X,E10.4,3X,E10.4,5X,E10.4,3X,E10.4,3X,E1
0.4,3X,

1E10.4,5X,E10.4,3X,E10.4,3X,E10.4,3X,E10.4,3X,E10.4,3X,E10.3
,3X,
        1E10.3,3X,E10.3)

3352  FORMAT(4E10.4,5X,4E10.4)

C
WRITE(15,*)'*****'
*****'
        IF(R5 .EQ. 0) GO TO 3380
        GO TO 3390
3380  IF(U3 .EQ. 0) GO TO 3400
3390  CONTINUE
3400  WRITE(*,*)
        WRITE(*,*)'AM I HERE?'
3420  CONTINUE
        CLOSE(UNIT=15)
C      CLOSE(UNIT=16)
        STOP
3430  END

        FUNCTION FNE(X)
        FNE=(( (2.59E-04*X+2.7487E-
2)*X+1.4472)*X+4.426E+1)*X+609.92

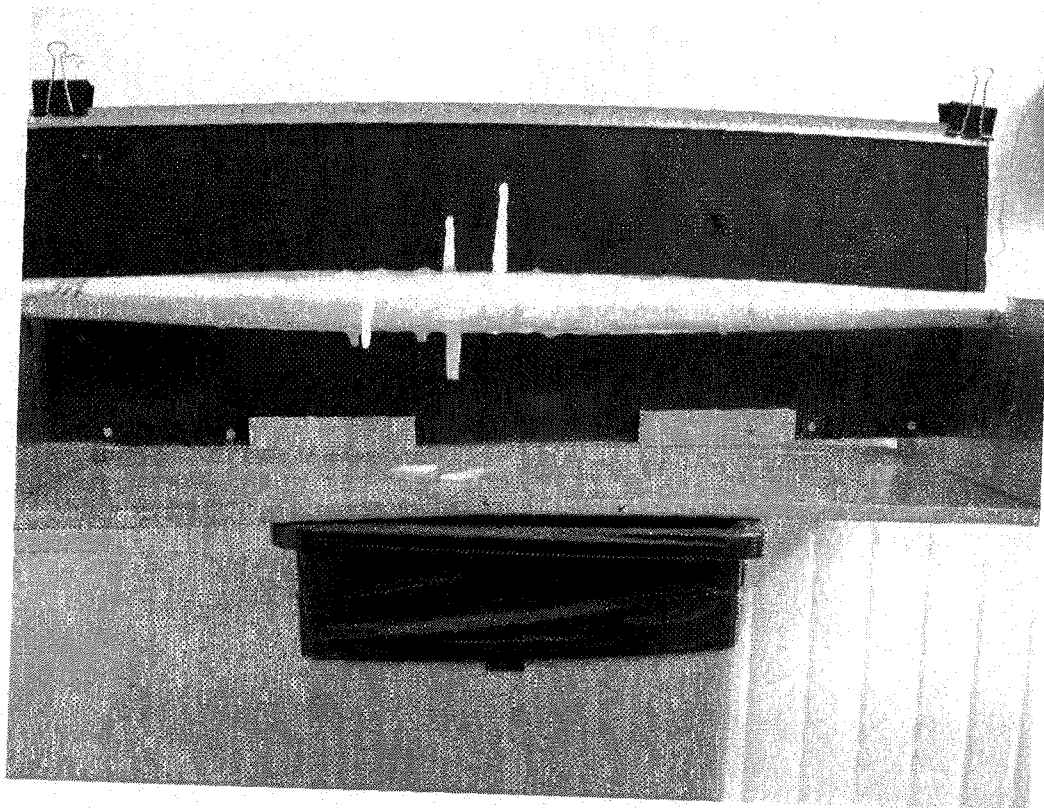
```

```
END FUNCTION
```

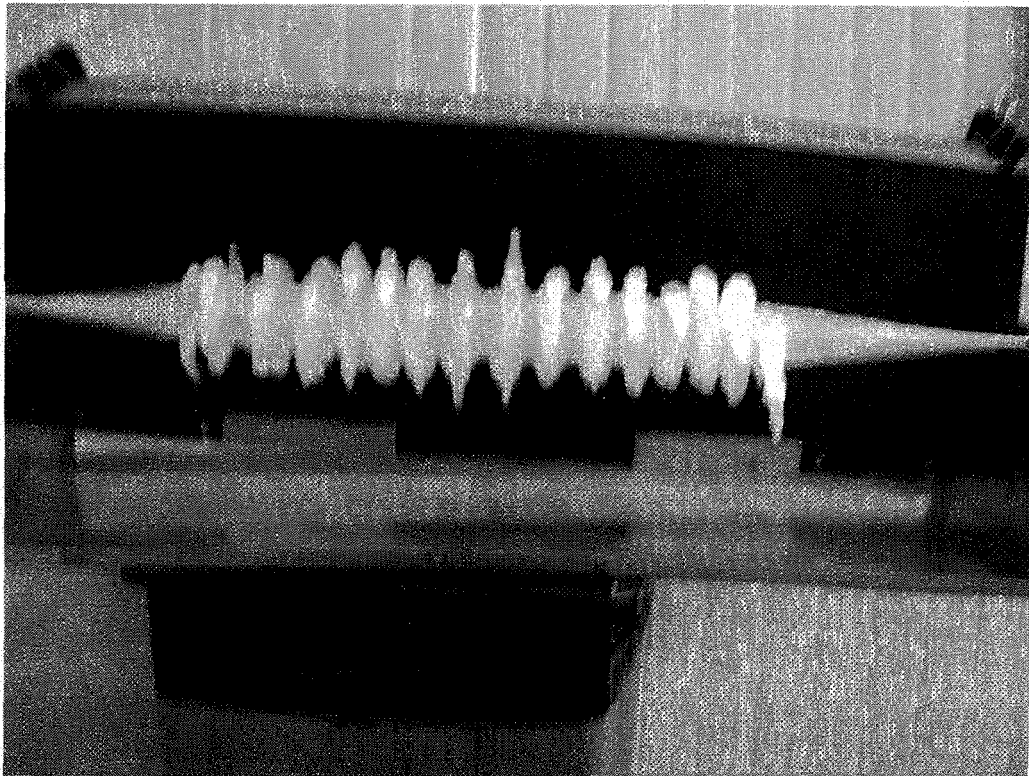
```
FUNCTION FNP(X)
```

```
FNP=( (1.036E-03*X+8.2461E-2) *X+2.8944) *X+44.26
```

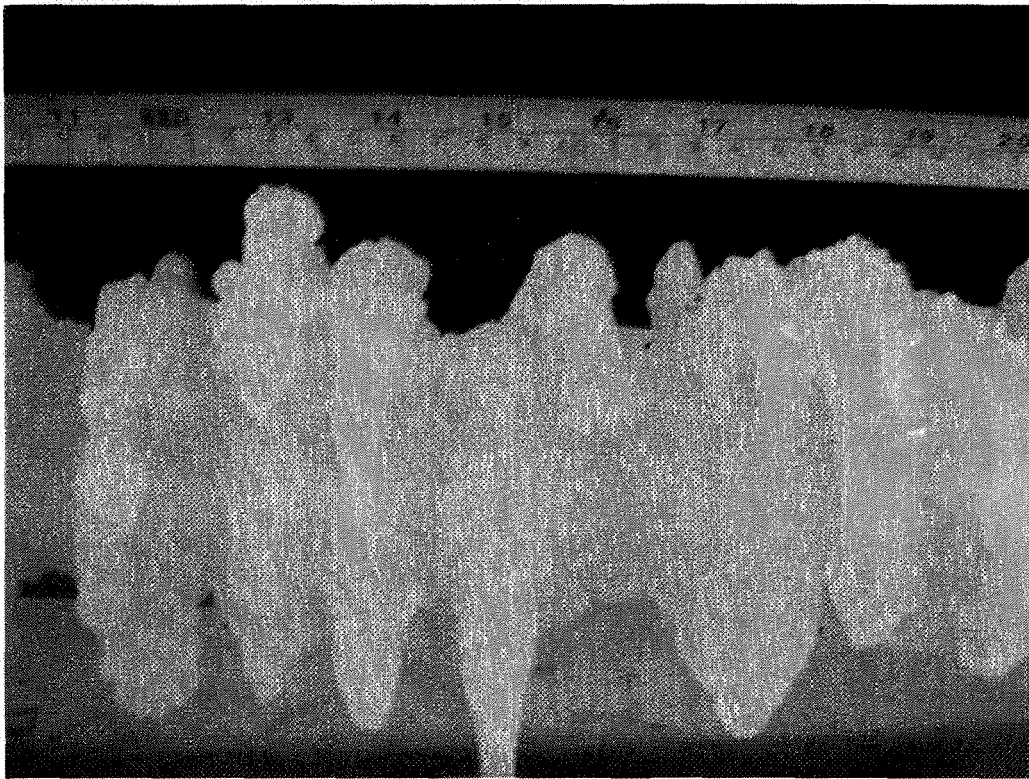
```
END FUNCTION
```



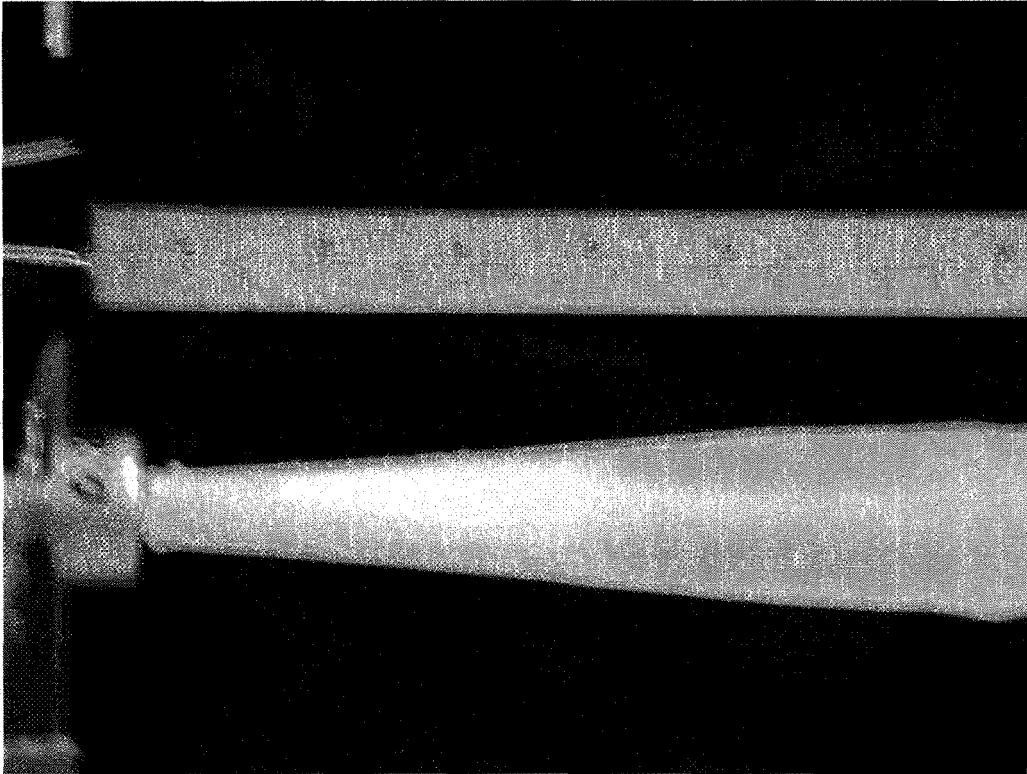
Test 71, rotating cylinder  $D=1.25$  (Inch),  $T=-10$  °C,  $V=5$  m/s



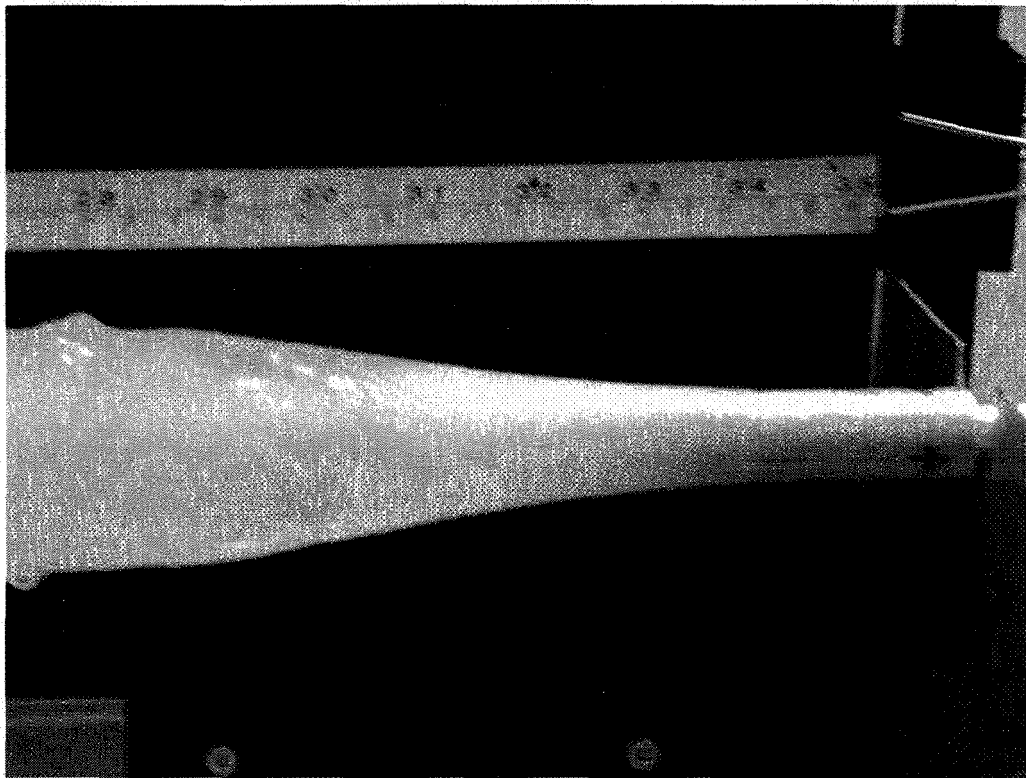
Test 70, rotating cylinder,  $D = 0.25$ ,  $T = 10\text{ }^{\circ}\text{C}$ ,  $V = 10\text{ m/s}$



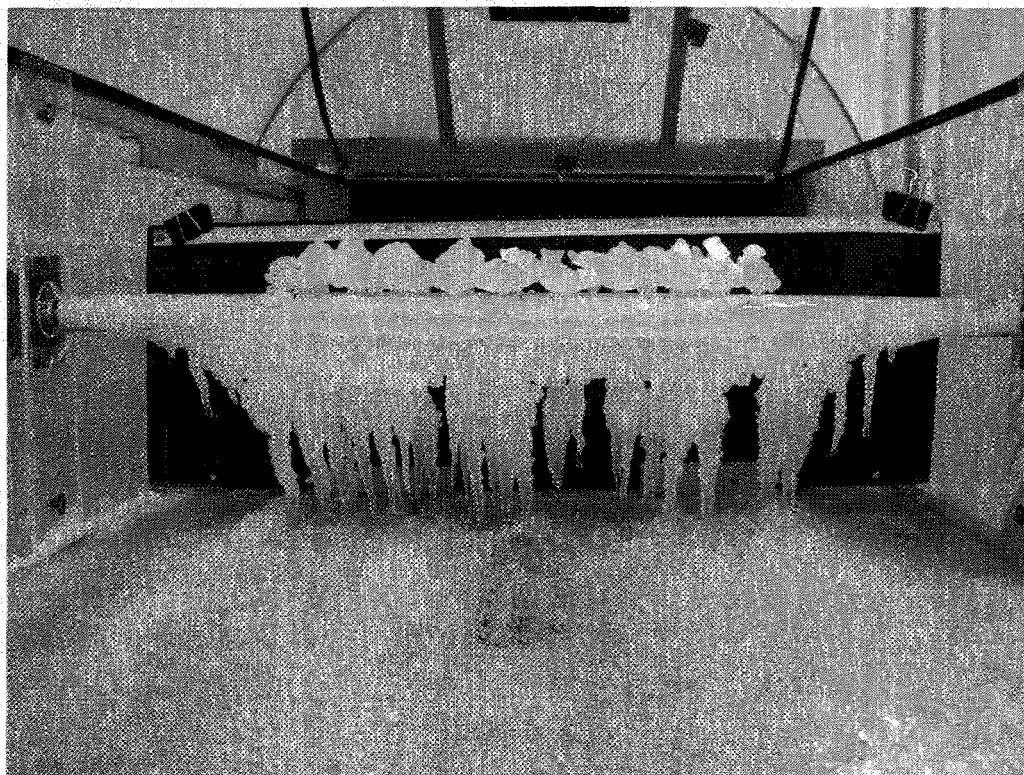
Test 45, centre of rotating cylinder,  $D=0.25$ ,  $T=-10\text{ }^{\circ}\text{C}$ ,  $V=10\text{ m/s}$



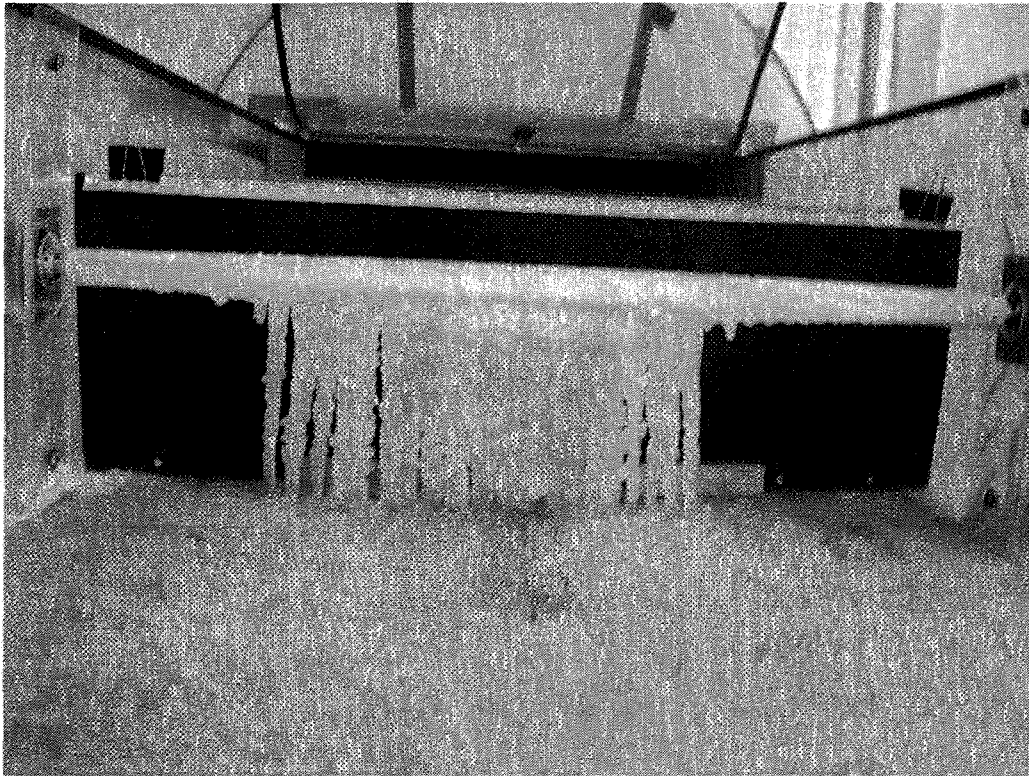
Test 44, left side of rotating cylinder,  $D=0.25$  (Inch),  $T=-10$  °C,  $V=5$ m/s



Test 43, right side of rotating cylinder,  $D=0.75$  (inch),  $T=-10$  °C,  $V=10$  m/s



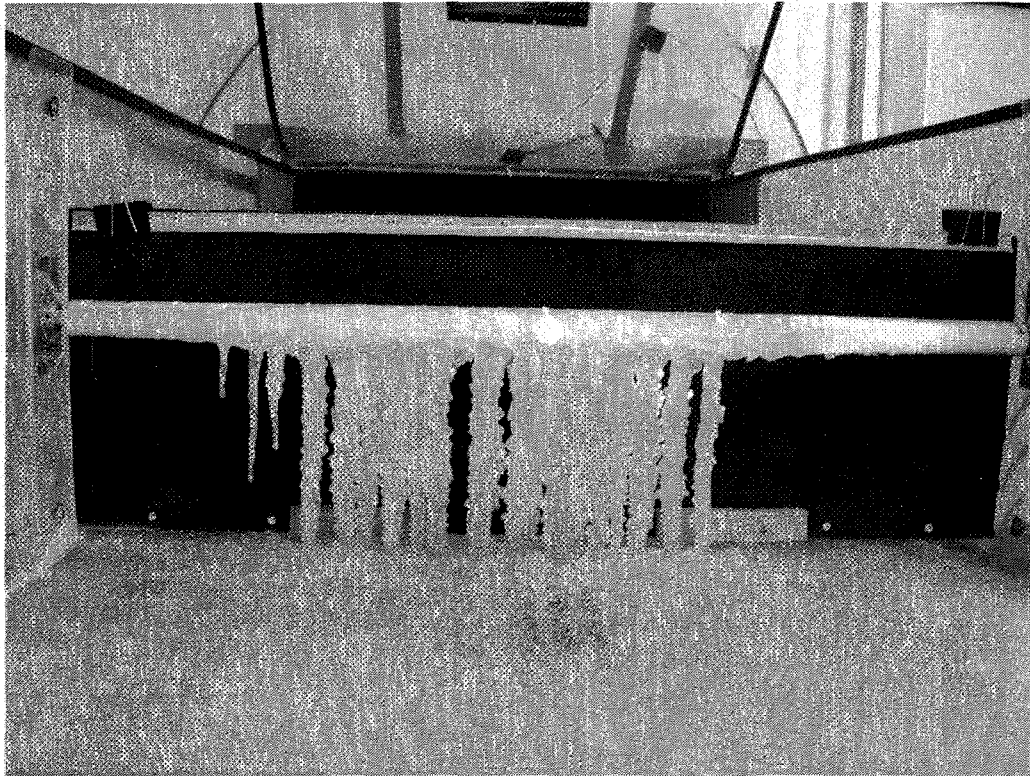
Test 69, fixed cylinder,  $T=-10\text{ }^{\circ}\text{C}$ ,  $V=10\text{ m/s}$



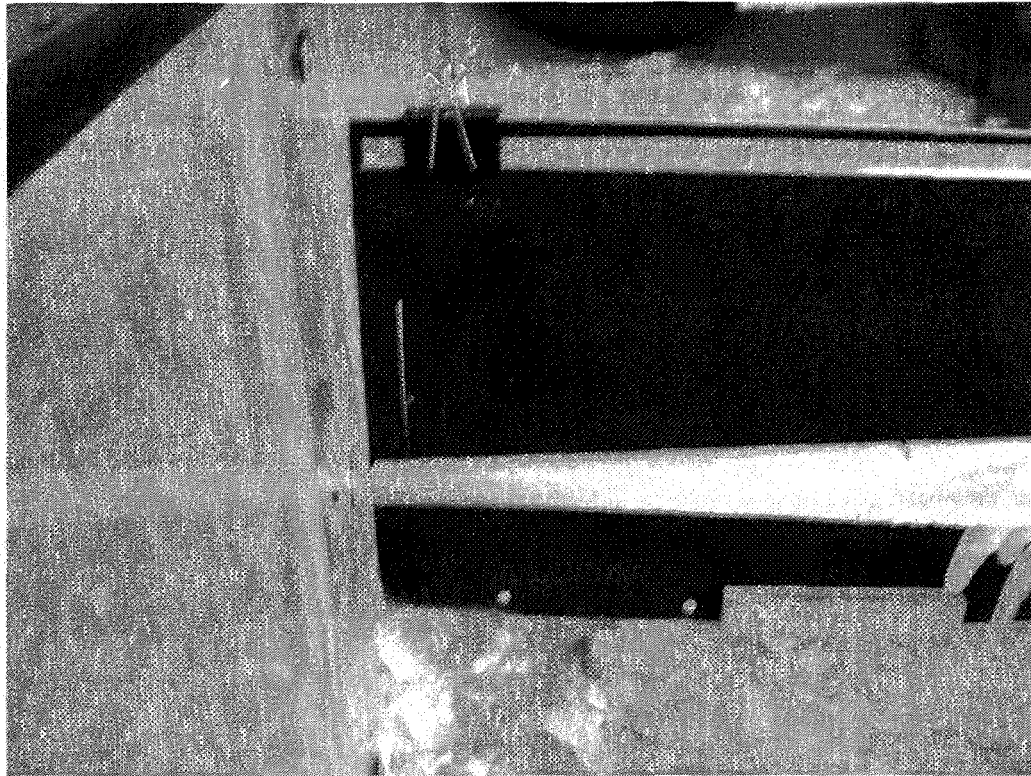
Test 68, fixed cylinder,  $D=1.375$  (inch),  $T= -10^{\circ}\text{C}$ ,  $V=5$



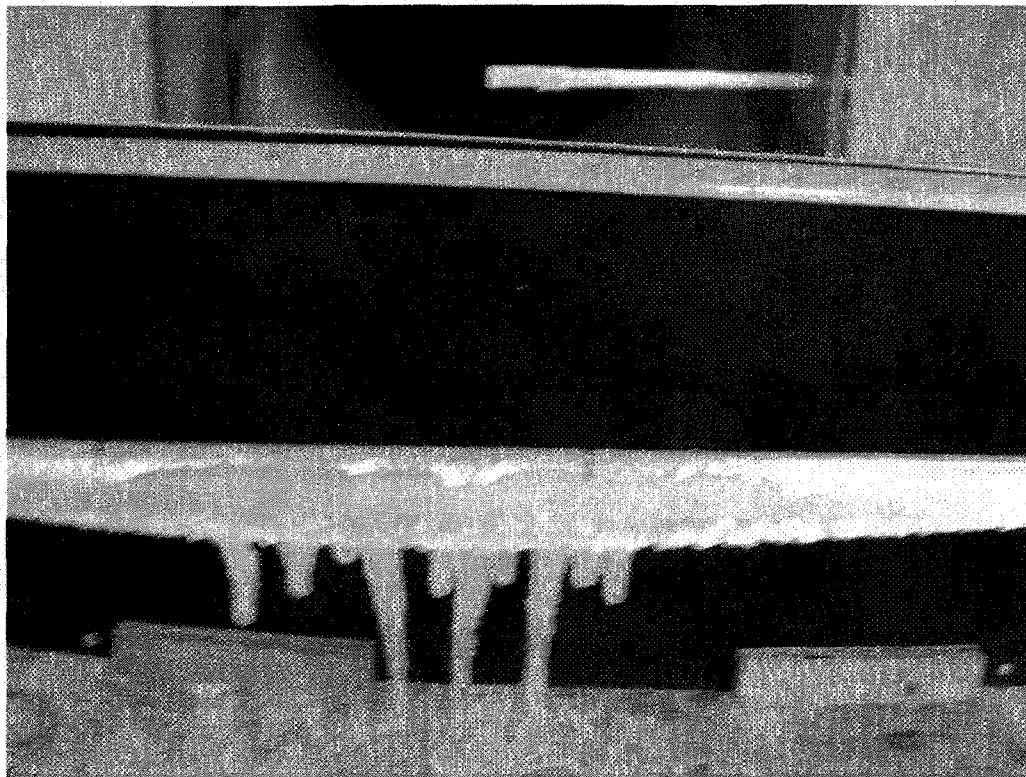
Test 67, fixed cylinder,  $D=1.25$ ,  $T=-10^{\circ}\text{C}$ ,  $V=10\text{ m/s}$



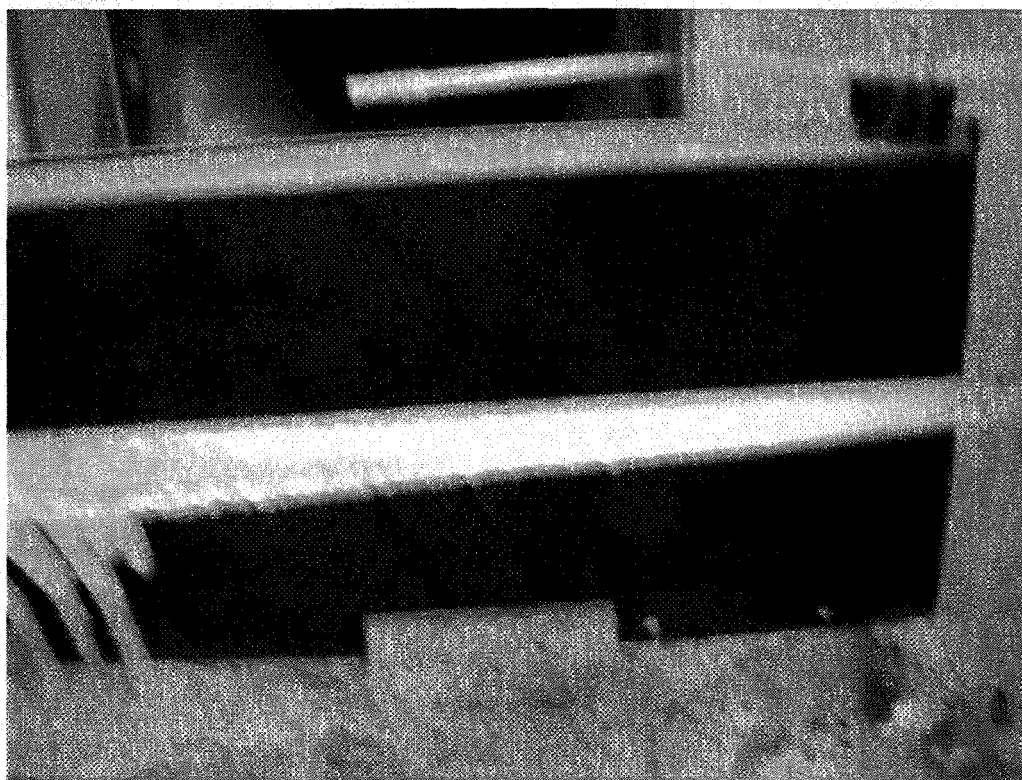
Test 66, fixed cylinder,  $D=1.25$  (inch),  $T=-10^{\circ}\text{C}$ ,  $V=5\text{m/s}$



Test 65, fixed cylinder, left side,  $D=0.75(\text{inch})$ ,  $T=-10\text{ }^{\circ}\text{C}$ ,  $V=5\text{ m/s}$



Test 65, fixed cylinder, centre part,  $D=0.75(\text{inch})$ ,  $T=-10\text{ }^{\circ}\text{C}$ ,  $V=5\text{ m/s}$



Test 65, fixed cylinder, right side,  $D=0.75(\text{inch})$ ,  $T=-10\text{ }^{\circ}\text{C}$ ,  $V=5\text{ m/s}$